ISSN 0914-9244
CODEN JSTEEW

COPY

Journal of Photopolymer Science and Technology

Volume 36 Number 2

2023

JOURNAL OF PHOTOPOLYMER SCIENCE AND TECHNOLOGY
Home Page https://www.spst-photopolymer.org
https://www.jstage.jst.go.jp/browse/photopolymer

Journal of Photopolymer Science and Technology publishes papers on the scientific progress and the technical development of photopolymers.

Editorial Board

Editor-in-Chief:
Hiroyuki MAYAMA, *Asahikawa Medical University*
Editors:
Masayuki ENDO, *Osaka University*
Teruaki HAYAKAWA, *Tokyo Institute of Technology*
Yoshihiko HIRAI, *Osaka Metropolitan University*
Takashi HIRANO, *SUMITOMO BAKELITE CO., LTD.*
Taku HIRAYAMA, *Hoya Co., Ltd.*
Hideo HORIBE, *Osaka Metropolitan University*
Takanori ICHIKI, *The University of Tokyo*
Takashi KARATSU, *Chiba University*
Yoshio KAWAI, *Shin-Etsu Chemical Co., Ltd.*
Shin-ichi KONDO, *Gifu Pharmaceutical University*
Hiroto KUDO, *Kansai University*
Kazuma KURIHARA, *AIST*
Takayuki MUROSAKI, *Asahikawa Medical University*
Tomoki NAGAI, *JSR Corporation*
Haruyuki OKAMURA, *Osaka Metropolitan University*
Hideo OHKITA, *Kyoto University*
Itaru OSAKA, *Hiroshima University*
Shu SEKI, *Kyoto University*
Atsushi SEKIGUCHI, *Litho Tech Japan Corporation*
Takehiro SESHITA, *Tokyo Ohka Kogyo Co., Ltd.*
Akinori SHIBUYA, *Fuji Film, Co., Ltd.*
Kuniharu TAKEI, *Hokkaido University*
Jun TANIGUCHI, *Tokyo University of Science* Takumi UENO, *Shinshu University*
Takeo WATANABE, *University of Hyogo*
Masashi YAMAMOTO, *Nat. Inst. Tech. Kagawa College*

International Advisory Board

Robert D. ALLEN, *IBM Almaden Research Center*
Paul F. NEALEY, *University of Chicago*
C. Grant WILLSON, *The University of Texas*
Ralph R. DAMMEL, *EMD Performance Materials*
Christopher K. OBER, *Cornell University*

COPY

The Editorial Office
Assoc. Prof. Hiroyuki MAYAMA
Department of Chemistry, Asahikawa Medical University, 2-1-1-1 Midorigaoka-Higashi, Asahikawa, Hokkaido 078-8510, Japan.
FAX: +81-166-68-2782, e-mail: mayama@asahikawa-med.ac.jp

Information for Contributors

Submit Manuscripts to the SPST Homepage (Journal --> Submission of Papers --> Editorial Manager). Submission is a representation that the manuscript has not been published previously elsewhere. The manuscript should be accompanied by a statement transferring copyright from the authors (or their employers-whoever holds the copyright) to the Society of Photopolymer Science and Technology. A suitable form for copyright transfer is available from the SPST Homepage. This written transfer of copyright, which previously was assumed to be implicit in the act of submitting a manuscript, is necessary under the Japan copyright law. Further information may be obtained from the "Manual for Manuscript Writing" at the SPST Homepage.

Proofs and All Correspondence: Concerning papers in the process of publication should be addressed to the Editorial Office.

Manuscript Preparation: All the papers submitted are reproduced electronically as they were. For this reason, the manuscripts should be prepared according to the Manual for Manuscript Writings shown at the SPST Homepage.

Subscription Price (Airmail Postage included):
¥12,000 (in Japan), US$ 150.00 (for Foreign)

Subscriptions, renewals, and address changes should be addressed to the Editorial Office. For the address changes, please send both old and new addresses and, if possible, include a mailing label from the wrapper of recent issue. Requests from subscribers for missing journal issues will be honored without charge only if received within six months of the issue's actual date of publication; otherwise, the issue may be purchased at the single-copy price.

Publication Charge (Reprint Order): To support a part of the cost of publication of journal pages, the author's institution is requested to pay a page charge of ¥3,000 per page (with a one-page minimum) and an article charge of ¥12,000 per article. The page charge (if honored) entitles the author to 50 free reprints. For Errata the minimum page charge is ¥3,000, with no articles charge and no free reprints.

The cover designed by M. Tsuda and M. Morishita

JOURNAL OF PHOTOPOLYMER SCIENCE AND TECHNOLOGY

COPY

Volume 36 Number 2

2023

Published by

THE SOCIETY OF PHOTOPOLYMER SCIENCE AND TECHNOLOGY

THE SOCIETY OF PHOTOPOLYMER SCIENCE AND TECHNOLOGY (SPST)

https://www.spst-photopolymer.org

Honorary President:
Minoru TSUDA
SPST & Chiba University

President:
Takeo WATANABE
SPST & University of Hyogo

Director of Publication:
Hiroyuki MAYAMA
Asahikawa Medical University

Director of Scientific Program:
Itaru OSAKA
Hiroshima University

Director of International Affairs:
Teruaki HAYAKAWA
Tokyo Institute of Technology

Director of Administration:
Hiroto KUDO
Kansai University

Office of the Administration:
c/o Prof. Hiroto KUDO
Department of Chemistry and Materials Engineering, Faculty of Chemistry, Materials and Bioengineering, Kansai University
3-3-35, Tamate-cho, Suita-shi, Osaka 564-8680, Japan
e-mail: hkudo@kansai-u.ac.jp

THE SPST REPRESENTATIVES 2023

Robert ALLEN, *IBM*
Hitoshi ARAKI, *Toray Co., Ltd.*
Masataka ENDO, *Osaka University*
Teruaki HAYAKAWA, *Tokyo Institute of Technology*
Taku HIRAYAMA, *HOYA Co., Ltd.*
Yoshihiko HIRAI, *Osaka Metropolitan University*
Takashi HIRANO, *Sumitomo Bakelite Co., Ltd.*
Hideo HORIBE, *Osaka Metropolitan University*
Takanori ICHIKI, *The University 0f Tokyo*
Takashi KARATSU, *Chiba University*
Yoshio KAWAI, *Shin-Etsu Chemical Co., Ltd.*
Shin-ichi KONDO, *Gifu Pharmaceutical University*
Hiroto KUDO, *Kansai University*
Kazuma KURIHARA, AIST
Masayuki KUZUYA, *Chubu Gakuin University*
Hiroyuki MAYAMA, *Asahikawa Medical University*
Takayuki MUROSAKI, *Asahikawa Medical University*
Seiji NAGAHARA, *Tokyo Electron Ltd.*
Tomoki NAGAI, *JSR Corporation*
Hideo Ohkita, *Kyoto University*
Haruyuki OKAMURA, *Osaka Metropolitan University*
Itaru OSAKA, *Hiroshima University*
Takehiro SEHITA, *Tokyo Ohka Kogyo Co., Ltd.*
Shu SEKI, *Kyoto University*
Atsushi SEKIGUCHI, *Litho Tech Japan Corporation*
Kohei SOGA, *Tokyo University of Science*
Akinori SHIBUYA, *Fuji Film Co., Ltd.*
Kuniharu TAKEI, *Hokkaido University*
Jun TANIGUCHI, *Tokyo University of Science*
Minoru TSUDA, *SPST & Chiba University*
Takumi UENO, *Shinshu University*
Takeo WATANABE, *SPST & University of Hyogo*
Shinji YAMAKAWA, *University of Hyogo*
Masahi YAMAMOTO, *Nat. Inst. Tech. Kagawa College*
Takashi YAMASHITA, *Tokyo University of Technology*
Wang YUEH, *Intel*

COPY

Notice about photocopying

Prior to photocopying any work in this publication, the permission is required from the following organization which has been delegated for copyright clearance by the copying owner of this publication.

- In the USA
  Copying Clearance Center Inc.
  222 Rosewood Drive, Danvers MA 01923, USA
  Tel: 1-978-750-8400, Fax: 1-978-750-4744, e-mail: info@copyright.com
  http://www.copyright.com
- Except in the USA
  Japan Academic Association for Copyright Clearance (JAACC)
  9-6-41 Akasaka, Minato-ku, Tokyo 107-0052, Japan
  Tel: 81-3-3475-5618, Fax: 81-3-3475-5619, e-mail: info@jaacc.jp
  http://www.jaacc.org

Journal of Photopolymer Science and Technology
Volume 36, Number 2 (2023) 67 − 71 ©2023SPST

Fabrication of Moth-eye-structured Films with Two Types of Resin Separated by Micro-order Regions

Kazuki Fujiwara[1], Hiroyuki Sugawara[2], Jun Taniguchi[1*],

[1] *Department of Applied Electronics, Tokyo University of Science*
Niijyuku Katsushika-ku, Tokyo, 125-8585, Japan
[2] *Geomatec Co., Ltd., R&D*
Yokohama Landmark Tower, 9th Floor, 2-2-1 Minato Mirai, Nishi-ku Yokohama, Japan
**junt@te.noda.tus.ac.jp*

Some organisms can control wettability for survival. Thus, these organisms are potential research targets for engineering applications. For example, a beetle is a desert dweller that captures water from fog and dew to drink. This characteristic shows potential for addressing the global water shortage. Beetle exoskeletons are composed of micropatterns with varying wettability (hydrophilic or hydrophobic). In this study, we propose a hybrid process that combines photolithography with UV nanoimprint lithography (UV-NIL). Photolithography is used to fabricate a resist micropattern on a nanopatterned substrate. In UV-NIL, the resist and UV-curable resin are released to fabricate micropatterns with different transferabilities and wettabilities. To realize this process, a resin compatible with photolithography and UV-NIL was developed.
Keywords: Ultraviolet nanoimprint lithography (UV-NIL), Moth-eye structure, Hybrid structure, Fluorinated epoxy photoresist, Water harvesting

COPY

1. Introduction

In recent years, biomimetic technology, which applies the excellent characteristics of organisms to engineering, has been attracting attention. The lotus leaf has a superhydrophobic self-cleaning effect (the lotus effect) [1], rose petals have a superhydrophobic function and are highly adhesive to water droplets (the rose petal effect) [2], and the Namib beetle captures water drops for drinking from fog and dew on the Atlantic coast of southwestern Africa (the water harvesting) [3]. These organisms possess sophisticated wetting control based on their surface structures. Such surfaces are attractive for solving the global water shortage problem by harvesting water [4–6] and fabricating a lab-on-a-chip to observe biochemical reactions at the microscopic scale [7–9]. This study proposes a hybrid process (Fig. 1) for bioinspired structures that combines photolithography with UV nanoimprint lithography (UV-NIL) technology [10].

In our previous study, we developed the high-throughput fabrication of moth-eye structures (nanoneedle arrays) using UV-NIL [11–15]. A moth-eye structure mold was fabricated by

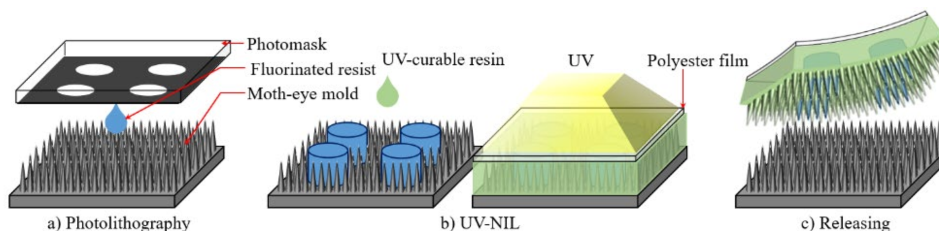

Fig. 1. Schematic of moth-eye structure film with two types of resin separated by micro-order regions. a) Photolithography-fabricated micropillars on the moth-eye substrate using the resist. b) In the UV-NIL process, UV-curable resin was dropped on the mold and cured. c) The resist and the resin were released to fabricate the moth-eye structure.

Received March 28, 2023
Accepted May 16, 2023

irradiating an oxygen ion beam onto a glassy carbon (GC) substrate [16–18]. Next, the structure of the mold was transferred using a UV-curable resin. However, the mold and the resin exhibit strong adhesion. Trifluoromethyl (CF_3-) groups have the lowest surface tension discovered to date. Treating materials with CF_3- groups can weaken their adhesive force. Thus, a chromium layer was deposited on the mold and fluorine–silane coupling was applied [19, 20]. By mixing fluorine monomers with the resin used in UV-NIL, we fabricated a superhydrophobic surface with contact angles (CA) of 150° or higher (Cassie–Baxter state) [21].

The following is the experimental setup of this study (Fig. 1). First, microstructures were fabricated on the nanostructures using photolithography on a moth-eye mold. To realize this process, a resist compatible with photolithography and UV-NIL was fabricated. SU-8 (3025) was used as the photoresist. In the next UV-NIL, a UV-curing resin, which has a different wettability from the resist, was dropped onto the mold. However, the resist did not peel off from the mold together with the UV-curable resin [22]. This is because the resist and mold have a high adhesive force. Thus, the resist was peeled off with the UV-curable resin by weakening its adhesion to the resist through mixing with a fluorine monomer. The fabricated surface had two types of resin separated by microscale regions with a moth-eye structure.

The moth-eye-structured resist was adhesive and hydrophobic (CA:128.2°), whereas the moth-eye-structured UV-curable resin was superhydrophobic (CA:161.5°). With this new process, wettability can be controlled by the pattern design of the photomask. We fabricated a biomimetic structure of the back of a Namib beetle and evaluated its water-harvesting properties.

2. Materials and methods

2.1. Fabrication of the moth-eye structured mold

The moth-eye mold was fabricated by etching. A 20 mm × 20 mm GC mirror-polishing substrate (Tokai Carbon Co., Ltd.) equipped with an oxygen ion beam was used. The GC is a carbon material with high hardness and chemical resistance. O_2 plasma was generated using inductively coupled plasma (ICP) equipment (EIS-700, ELIONIX Inc.). O_2 plasma was generated under the following conditions: vacuum degree: 5.0 × 10^{-2} Pa or less; antenna RF power: 600 W, substrate RF power: 50 W; O_2 mass flow rate: 50 sccm; and irradiation time: 600 s to fabricate the moth-eye mold [18].

2.2. Release treatment of the moth-eye mold

Figure 2 shows a schematic of the release treatment process.

Cr (~30 nm) is deposited on the mold using vacuum deposition equipment (VFC-2600F, ULVAC Kiko Co., Ltd.). Subsequently, the mold surface is oxidized to Cr_2O_3 to adsorb the silane coupling treatment (Optool UD-509, Daikin Industries, Ltd.). Optool UD-509 is diluted with Optool HD-TH (Daikin Industries, Ltd.) to 1 wt.%, and the mold is dipped in the solution. The Optool is then evaporated by heating to 60 °C, and the mold and Optool are sealed for 30 min. The mold is heated to 120 °C for 15 min and rinsed with a fluorine-based solvent (NOVEC7300, 3M Company) and water to remove contaminants.

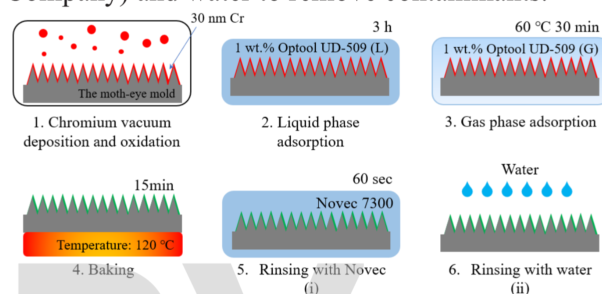

Fig. 2. Process of the release treatment applied to the moth-eye mold.

COPY

2.3. Fabrication of the moth-eye structure film with two types of resin separated by a micron-order region

First (Fig. 3), a negative resist (SU-8(3025), Kayaku Advanced Materials, Inc.) is mixed with a 1 wt.% fluorine monomer (2,2,3,3,4,4,4,5,5,5-Nonafluoropentyloxirane, Tokyo Chemical Industry Co., Ltd.) by heating at 50 °C. The mass concentration of the fluorine monomer is given by:

$$Monomer\ [wt.\%] = \frac{Monomer\ [g]}{Resist\ [g] + Monomer\ [g]} \times 100$$

This monomer is composed of a fluorinated chain on an epoxy group. The base of SU-8 is epoxy and thus does not separate from the monomer. This low-surface-free-energy treatment improves the release properties of the resist. Next, the moth-eye mold is heated at 50 °C, the fluorinated resist is dropped, and a polyester film (Cosmoshine A 4300, Toyobo Co., Ltd.) is placed on it. Then, the resist is filled into the moth-eye structure at a load of 100 N and a speed of 1 m/min by a roll press device at 50 °C. The polyester film is removed before baking because it interferes with the volatilization of SU-8. The bake is performed at 80 °C to prevent the resist

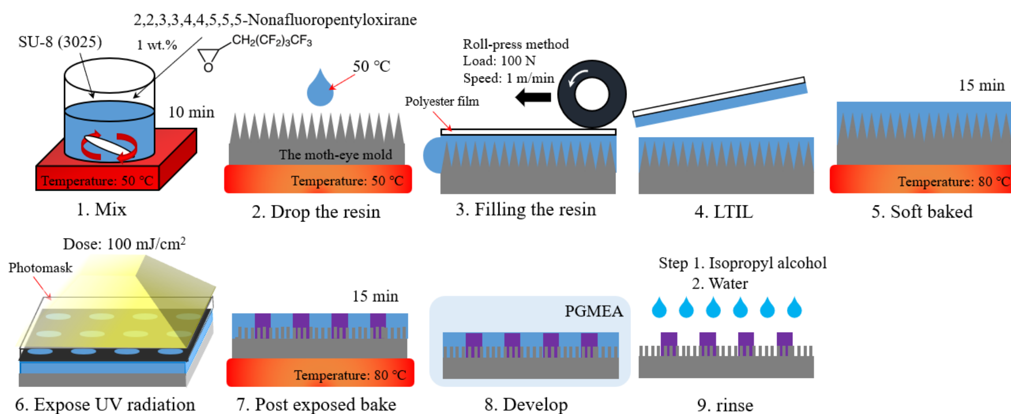

Fig. 3. Fabrication process of moth-eye structure film with two types of resin separated by micro-order regions. 1) Mix the fluorine monomer into the resist SU-8 for the resist to lower the surface free energy. 2) Drop the resist on the moth-eye mold and cover it with the polyester film. 3) Pressing to fill the resist into the pattern of the moth-eye with the roll-press equipment. 4) Release the polyester film. 5~9) The process of photolithography

on the mold from becoming spherical owing to the fluorine monomer. The photomask has a microscale dot pattern, and the resist is exposed to a UV dose of 100 mJ/cm^2. Next, the resist is baked at 80 °C. Once it is cooled to room temperature, it is developed using PGMEA (Kishida Chemical Co., Ltd.). The moth-eye mold with the micropatterns is rinsed with isopropyl alcohol (Kishida Chemical Co., Ltd.) and pure water.

In the next UV-NIL process (Fig. 4), the fluorine compound mixture acrylic UV-curable resin (Geomatec Co., Ltd.) is placed on the micropatterned moth-eye surface, and the polyester film is covered and pressed with a glass slide. Then, UV light (wavelength: 365 nm) is irradiated at 375 mJ/cm^2, and the resist on the mold was removed. After release, the film is baked at 80 °C for 30 min to form fluorine chains on the surface to improve water repellency. Hence, this film is referred to as the hybrid resin film.

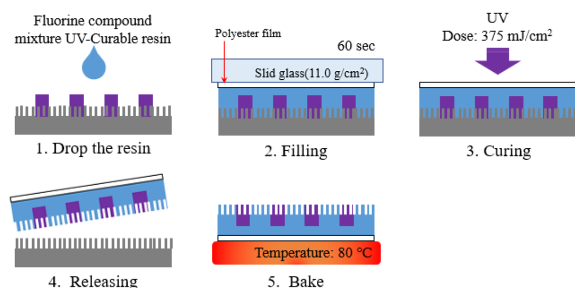

Fig. 4. Fabrication process of moth-eye structure film with two types of resin separated by micro-order regions. 1) The UV-curable resin was dropped onto the micropatterned moth-eye mold and covered with the polyester film. 2) The resin was filled into the needle of moth-eye by applying pressure. 3) The resin was exposed to UV radiation. 4) The UV-cured resin and resist were bonded and released. 5) The water repellency was improved by bake treatment.

COPY

3. Results and discussion

3.1. Evaluation of moth-eye structure transferability of various types of resins

The fluorine compound mixture acrylic UV-curable resin (Geomatec Co., Ltd) and the fluorinated resist SU-8 (3025) were transferred from the moth-eye mold through UV-NIL. Fig. 5 shows the SEM images of the top and cross-sectional (75°) views of the films. The hybrid resin film (Fig. 5 (iii)) exhibits moth-eye patterns with dots (the average diameter of dots: 211.5 µm, the average pitches: 400 µm), respectively, displaying the different moth-eye patterns of the two resins (Fig. 5 (i) and (ii)).

Table 1 depicts the images of 5 µL water droplets on the films, contact angle (CA), and sliding angle (SA) using a contact angle meter (DM-701, Kyowa Interface Science Co., Ltd.). The CAs of the hydrophobic samples were calculated using the Young–Laplace method.

Table 1. Wettability of moth-eye structure transferability of various types of resins.

Resin	C.A. [°] (Water 5 µL)	S.A. [°] (Water 5 µL)
Fluorine compound mixture UV-Curable resin (Geomatec Co., Ltd.)	161.5 ± 1.3	20
SU-8, Fluorinated Monomer 1 wt.%	128.2 ± 2.7	Adhered
1. Fluorine compound mixture UV-Curable resin 2. SU-8, Fluorinated Monomer 1 wt.%	152.4 ± 0.4	Adhered

The moth-eye film (a fluorine compound-containing resin) exhibits low adherence and superhydrophobicity: CA = 161.5° and SA = 20°.

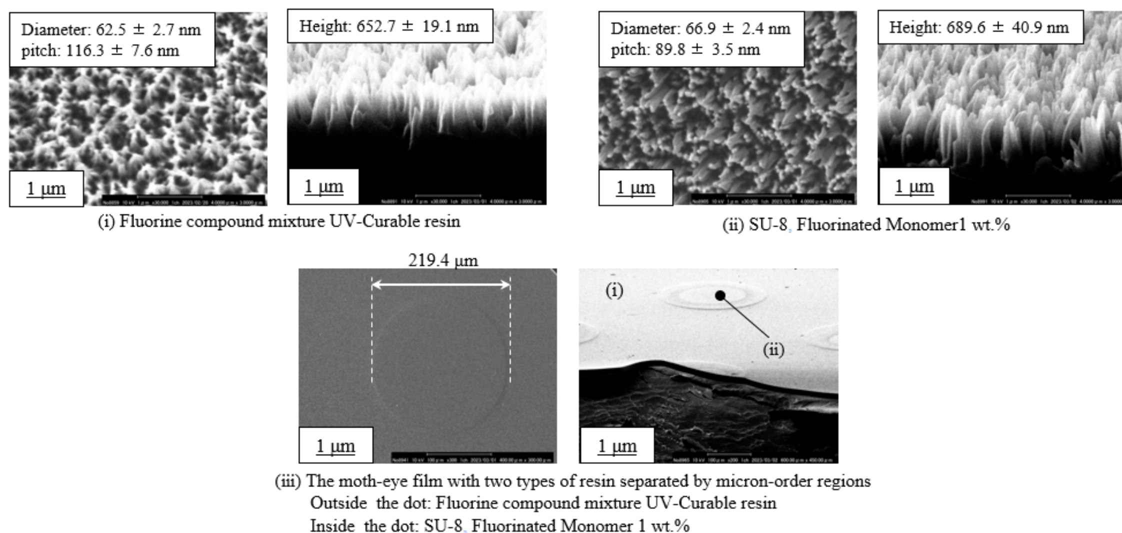

Fig. 5. SEM images; (i, ii) The moth-eye of various types of resins, (iii) Perspective view of the hybrid resin film.

The moth-eye film (fluorinated resist SU-8) was hydrophobic with high adhesion (CA = 128.2°), and no water droplets flowed when the film was inverted by 180°. Only the hybrid resin film exhibited both superhydrophobicity (CA = 152.4°) and high adhesion (SA = 180°).

3.2. Fog collection

Fig. 6 shows the setup of the fog-collection experiment. The masses of water in the moth-eye and hybrid resin films collected from the fog were measured every minute using an electronic balance (A&D Manufacturing Co., Ltd.). Fog was generated using an ultrasonic humidifier (UHM-280S-W, IRIS OHYAMA Inc.)

Fig. 7 illustrates the results of the amount of water collected using each patterned film (20 mm × 20 mm), and Table 2 summarizes the amount of water collected after 60 min, the time when the first water droplet slid off, and the gradient and coefficient of determination from the regression line of the plots. The unit of the gradient is μg/min·mm^2, which is used to evaluate the efficiency of fog collection rate. For comparison, a powdered water-absorbing resin (produced by KENIS LIMITED) was attached to a 20 mm × 20 mm square tape, soaked with a small quantity of pure water, and then subjected to five fog collection rate measurements. The average fog collection was 31.3 μg/min·mm^2. The water droplets on the moth-eye films slid down the flat surface faster (fluorine compound mixture UV-curable resin). Upon comparing the fog collection rate of the moth-eye film (fluorine compound mixture UV curable resin) with that of the hybrid resin film, the hybrid resin film exhibited the highest water collection efficiency, i.e., 19.0 μg/min·mm^2 compared to 7.3 μg/min·mm^2. The fog adheres to the water-adhesive resist, and as the water droplets enlarge, the area in contact with the low-adhesion fluorine UV-cured resin expands, causing the water droplets to slide off.

COPY

4. Conclusion

A moth-eye structure film with two types of resins separated by microscale regions was fabricated by combining moth-eye transfer technology (UV-NIL) and photolithography. First, resist SU-8 mixed with a fluorine monomer was dropped onto the moth-eye mold, and the microstructure was fabricated via photolithography. In the next UV-NIL step, the UV-cured resin and fluorinated resist were released together to fabricate a moth-eye structure that exhibited different transferabilities and wettabilities. This moth eye is composed of two types of resins on the same surface as the structure of the back of the Namib beetle. The contact angle of the hybrid resin film was 152.4°, indicating superhydrophobicity and high adhesion (rose petal effect).

Fog collection experiments were conducted on superhydrophilic, superhydrophobic, and hydrophobic surfaces with high adhesion/superhydrophobic hybrid surfaces. The experiments showed that the beetle-inspired surface was the most efficient.

References

1. M. Yamamoto, N. Nishikawa, H. Mayama, Y. Nonomura, S. Yokojima, S. Nakamura, and K. Uchida, *Langmuir*, **31**(26) (2015) 7355–7363. https://doi.org/10.1021/acs.langmuir.5b00670.

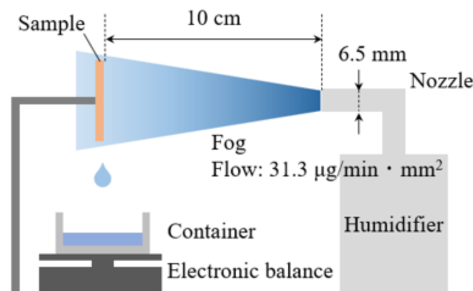

Fig. 6 Setup of the fog collection experiment

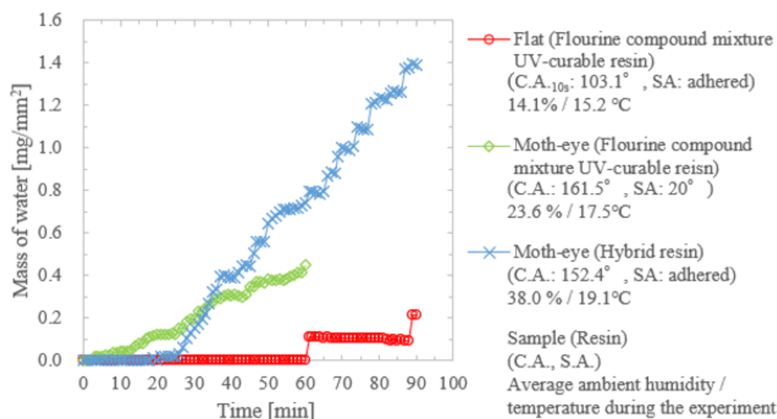

Fig. 7 Plot of water collection collected by each sample per minute.

Table. 2 Result of fog collection experiment

Sample	Mass of water (after 60 min) [mg / mm²]	Time when water droplet first slid down [min]	Regression line	
			Gradient [μg / min・mm²]	Coefficient of determination R^2
Flat (Fluorine compound mixture UV-curable resin)	0.000	61	0.3	0.074
Moth-eye (Fluorine compound mixture UV-curable resin)	0.449	3	7.3	0.982
Moth-eye (Hybrid resin)	0.741	19	19.0	0.992

2. X. Hong, X. Gao, and L. Jiang, *J. Am. Chem. Soc.,* **129** (2007) 1478–1479. https://doi.org/10.1021/ja065537c.
3. A. R. Parker and C. R. Lawrence, *Nature*, **414** (2001) 33–34.
4. A. Lee, M. W. Moon, H. Lim, W. D. Kim, and H. Y. Kim, *Langmuir* , **28**(27) (2012) 10183–91. https://doi.org/10.1021/la3013987.
5. M. Qadir, G. C. Jiménez, R. L. Farnum, and P. Trautwein, *Front. Water*, **3** (2021). https://doi.org/10.3389/frwa.2021.675269.
6. D. Nioras, K. Ellinas, and E. Gogolides, *ACS Appl. Nano Mater.*, **5**(8) (2022) 11334–11341. https://doi.org/10.1021/acsanm.2c02439.
7. E. Ueda and P. A. Levkin, *Adv. Mater.* , **25** (2013) 1234–1247. https://doi.org/10.1002/adma.201204120.
8. Y. Wang, H. Yang, H. Liu, L. Zhang, R. Duan, X. Liu, and J. Chen, *RSC Adv.*, **7** (2017) 53525–53531. https://doi.org/10.1039/C7RA09283K.
9. M. Cao and L. Jiang, *Surface Innovations*, **4**(4) (2016) 180–194. http://dx.doi.org/10.1680/jsuin.16.00004.
10. S. Y. Chou, P. R. Krauss, and P. J. Renstrom, *J. Vac. Sci. Technol.*, **14** (1996) 4129. https://doi.org/10.1116/1.588605.
11. K. Yajima, K. Adachi, Y. Tsukahara, and J. Taniguchi, *Microelectron. Eng.*, **110** (2013) 188–191. https://doi.org/10.1016/j.mee.2013.03.104.
12. C. H. Chuang, D. M. Lu, P. H. Wang, W. Y. Lee, and M. O. Shaikh, *Microsyst. Technol.*, **24** (2018) 389–395.
13. J. Kawauchi, S. Hiwasa, and J. Taniguchi, *Photopolym. Sci. Technol.*, **32** (2019) 143–148. https://doi.org/10.2494/photopolymer.32.143.
14. M. Vogler, S. Wiedenberg, M. Mu¨hlberger, I. Bergmair, T. Glinsner, H. Schmidt, E. B. Kley, and G. Gru¨tzner, *Microelectron. Eng.*, **84** (2007) 984–988. https://doi.org/10.1016/j.mee.2007.01.184.
15. T. Okabe, H. Maebashi, and J. Taniguchi, *Microelectron. Eng.*, **213** (2019) 6–12. https://doi.org/10.1016/j.mee.2019.04.007.
16. J. Taniguchi, E. Yamauchi, and Y. Nemoto, *J. Phys. Conf. Ser.*, **106** (2008) 012011. https://doi.org/10.1088/1742-596/106/1/012011.
17. T. Okumoto, J. Taniguchi, and Y. Kamiya, *Microelectron. Eng.*, **88** (2011) 1832–1835. https://doi.org/10.1016/j.mee.2011.02.062.
18. T. Yano, H. Sugawara, and J. Taniguchi, *Micro and Nano Engineering*, **9** (2020) 100077. https://doi.org/10.1016/j.mne.2020.100077.
19. M. Zelsmann and N. Chaix, *J. Vac. Sci. Technol. B*, **25**(6) (2007) 2430–2434. https://doi.org/10.1116/1.2806969.
20 H. Schmitt, M. Zeidler, M. Rommel, A. J. Bauer, and H. Ryssel, *Microelectronic Engineering*, **85** (2008) 897–901.
21. Y. Otsuka, S. Hiwasa, and J. Taniguchi, *Microelectronic Engineering*, **123** (2014) 192–196. https://doi.org/10.1016/j.mee.2014.09.001.
22. K. Arai, T. Wakasa, K. Fujiwara, J. Taniguchi, The 21st International Conference on Nanoimprint and Nanoprint Technologies, Toyama, Japan, (2022)

COPY

COPY

Journal of Photopolymer Science and Technology
Volume 36, Number 2 (2023) 73 − 76 ©2023SPST

Filling Behavior Observation of UV-curable Resin Using Bridge-Structure Mold

Yusuke Murakami[1], Yusuke Nagai[1], and Jun Taniguchi[1*]

[1] *Department of Applied Electronics, Tokyo University of Science, 6-3-1 Niijuku, Katsushika-ku, Tokyo 125-8585, Japan*
**junt@te.noda.tus.ac.jp*

In recent years, owing to the increasing demand for semiconductors, decreasing the power consumption of semiconductor-exposure equipment has become an important issue. Therefore, ultraviolet nanoimprint lithography (UV-NIL), which can efficiently produce nanopatterns with reduced power consumption, is desirable. However, the problem with UV-NIL is that when the mold is subjected to a mold-release treatment, the water repellency increases, and the resin does not fill the interior of the fine pattern. Therefore, investigating the filling behavior is essential. Our previous study used hydrogen silsesquioxane (HSQ) as the bridge structure, which is a negative-type electron-beam (EB) resist with a film thickness of 300 nm. Using HSQ, the height of the bridge structure was less than 300 nm, and a small amount of UV-curable resin was obtained. Therefore, thicker negative-type EB resists are required to address this issue. In this study, a negative-type photoresist was used as the bridge structure via EB lithography. Consequently, the height and thickness of the bridge were approximately 6 and 2 µm, respectively, and hence, we could comprehensively pursue the filling behavior.
Keywords: Ultraviolet nanoimprint lithography, Bridge structure, Capillary force

COPY

1. Introduction

Ultraviolet nanoimprint lithography (UV-NIL) is a next-generation lithography technique used in various fields [1-5]. This is because the price and power consumption of UV exposure equipment in semiconductor manufacturing have become enormous. However, when UV-NIL is performed using a normal mold in the air, bubble defect [6-8] interrupts the observation of the essential filling behavior. Therefore, we fabricated a mid-air structure mold to observe the filling behavior of the UV-curable resin at atmospheric pressure [9]. Moreover, a problem with NIL is that when the mold is subjected to mold-release treatment, the water repellency increases, and the resin does not fill the interior of the fine pattern [10-12]. This phenomenon was observed in our previous study using a bridge structure mold [13], which revealed that the filling height of the UV-curable resin depended on the NIL pressure. Our previous study used hydrogen silsesquioxane (HSQ) as the bridge structure, which is a negative-type electron-beam (EB) resist [14]. The filling behavior of the mold pattern in air was observed using scanning electron microscopy (SEM). The filling behavior is expressed as follows:

$$Pc = 4\gamma\cos\theta/a \quad (1)$$

This is called "capillary force" [15-18], where a is the length of the square aperture size, γ is the surface tension of the liquid, and θ is contact angle in the channel. HSQ is a negative-type EB resist with a film thickness of 300 nm. Using HSQ, the height of the bridge structure was less than 300 nm, and a small amount of UV-curable resin was obtained. Therefore, thicker negative-type EB resists are required to address this issue.

A negative-type photoresist (SU-8 3025, Nippon Kayaku Co., Ltd.) was used for the bridge structure via EB lithography (EBL). SU-8 is a negative resist with a large film thickness and viscosity and is used in various microscopic processing [19,20]. We investigated the filling behavior of the UV-curable resin comprehensively by increasing the height and thickness of the bridging structure.

Received March 28, 2023
Accepted May 16, 2023

2. Materials and methods

2.1. Fabrication of the bridge structure

Figure 1 shows the fabrication process of the bridge structure. First, the SU-8 resist was applied to a 1-cm square Si substrate using spin coating. The resist was baked at 95 °C for 10 min on a hot plate. After baking, EBL was performed to obtain a bridge structure. Figure 2 shows the design of the bridge structure directly above and the experimental conditions. The lower row (which will be bridge beam after development) was delineated with an acceleration voltage of 50 kV, a beam current of 100 pA, and a dose of 400 μC/cm^2. The upper row (which will be bridge after development) was delineated with an acceleration voltage of 10 kV, a beam current of 100 pA, and a dose of 300 μC/cm^2. After drawing, the film was developed for 5 min using a SU8 developer and washed with pure water. Finally, the films were hard-baked at 180 °C for 30 min.

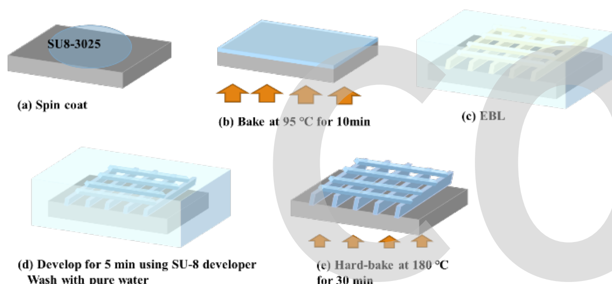

Fig. 1. Fabrication process of bridge structure.

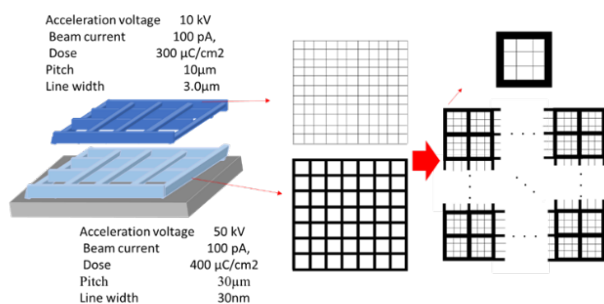

Fig. 2. Design of the bridge structure directly above and the experimental conditions.

2.2. Mold release processing

Figure 3 shows the mold-release process. Fabricated bridge-structure molds were soaked in 1% release-coating agent (Optool DSX, Daikin Co., Ltd.) for 12 h, heated at 120 °C for 5 min, and then soaked in hydrofluoroether (Novec 7300, 3M Japan Co., Ltd.) for 30 s. In this experiment, a coated bridge structure mold was prepared without release for comparison.

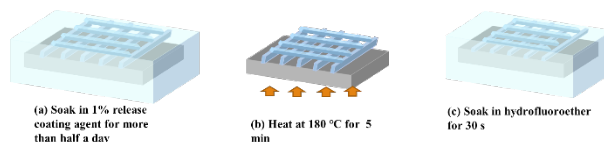

Fig. 3. Mold-release process.

2.3. UV-NIL transfer process

Figure 4 illustrates the UV-NIL process. A UV-curable resin (PAK-01-CL, Toyo Gosei Co., Ltd.) was dropped onto the mold, covered with a polyester film (Cosmoshine A4300, Toyobo Co., Ltd.), and pressed at various pressures. Under constant pressure, UV light was irradiated for 30 s. Finally, the film was peeled from the bridge structure mold, and a transfer pattern was obtained.

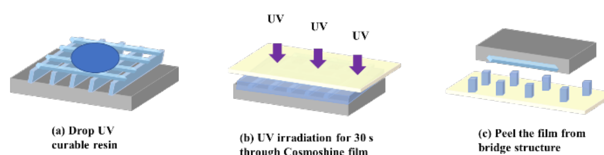

Fig. 4. UV-NIL process using a bridged structure mold

COPY

3. Result and discussion

3.1. Bridge structure

Figure 5 shows the fabricated bridge structures. Figure 6 shows a portion of the bridge girder. The line width and height of the bridge girder were approximately 5 and 7 μm, respectively; the pitch was 30 μm. However, the lower part of the bridge girder was thicker than the top part. Hence, the space was smaller than 30 μm. The line width was larger than the design value of 30 nm, and the space is considerably smaller than 30 μm. This may be due to the thickening of the line width caused by the scattering effect. Although the pitch was 30 μm, the spacing considering the line width was 20 μm. The line width of the bridge was 5 μm, the aperture size was approximately 5 μm^2, and the height was 2 μm. The upper stage was also smaller than the designed aperture size of 10 μm^2. This was also attributed to the scattering effect; the aperture size was 5 μm^2 when the line width was considered. In addition, a part of the upper bridge was slightly slack. This was probably owing to the influence of the meniscus force generated during the development. When the mold was immersed in the developer, a capillary force was generated between the bridge and the substrate. When the developer dried out, the capillary force was attracted between the bridge and the substrate, and

the bridge was bent toward the substrate.

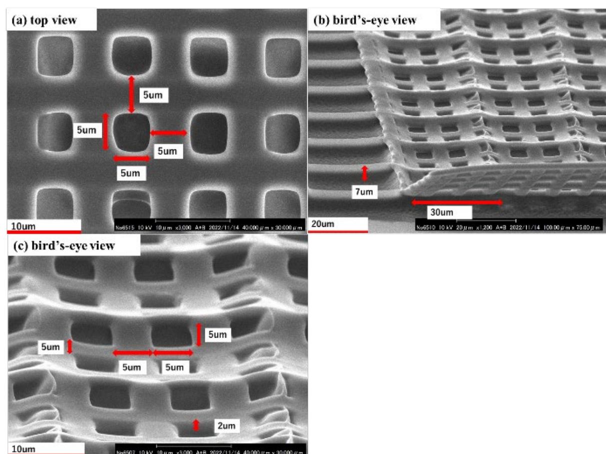

Fig. 5. Bridge structure.

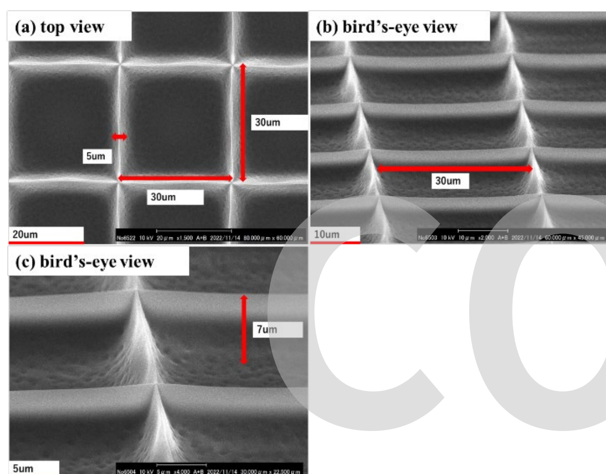

Fig. 6. Bridge girder.

3.2. Mold-release processing

Figure 7 shows the UV-NIL transfer bridge structure mold with and without the release coating. With the release coating, although some resin remained, no significant changes were observed in the mold. Therefore, the transfer process performed well. In contrast, without the release coating, the UV-curable resin adhered. Therefore, the transfer did not perform well. Hence, a release coating is important.

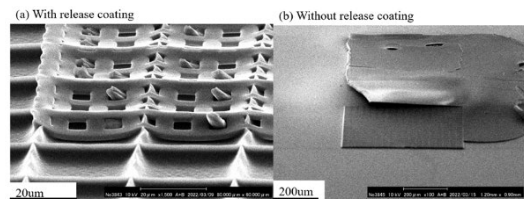

Fig. 7. (a)Mold after transfer with mold-release processing. (b) Mold after transfer without mold-release processing.

3.3. UV-NIL transfer process

Figure 8 shows the UV-curable resin shapes transferred using the release-coated bridge-structure molds at various NIL pressures. Figure 9 shows the relationship between the replication patterns and pressure. The transfer pressure was changed from 7.4 kPa to 5.6 × 10 kPa. In Fig. 8(a)–(c), the heights of the transferred UV-curable resins did not change significantly at 2.4, 2.3, and 1.6 μm, respectively. This indicates that the UV-curable resin was repelled by the capillary force of the bridging structure that was mold-release coated and did not enter the interior. This means that low pressure causes a shortage in filling. In contrast, in Figs. 8(d) and (e), the height of transferred UV curable resin increased to 3.1 and 4.5 μm. This indicates that the transfer pressure was greater than the capillary force, and the UV-curable resin entered the interior; thus, the height increased. The transfer pressure and height of the cured UV-curable resin patterns through the apertural area increased. However, this was not the case. In Figs. 8(f)–(h), the height of transferred UV-curable resin was 3.8, 4.0, and 3.8 μm and hump-shaped. This implies that sufficient pressure was applied to fully penetrate the resin.

COPY

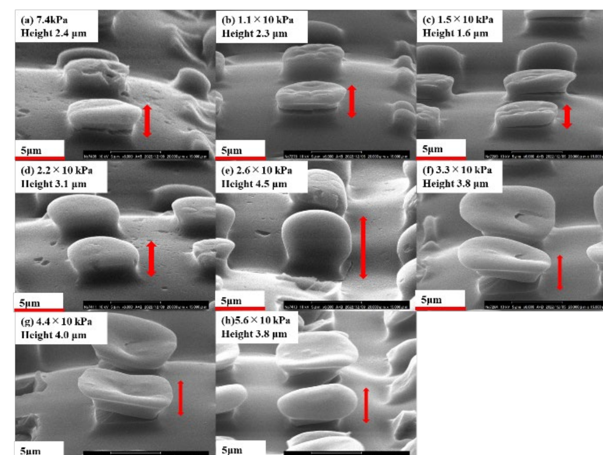

Fig. 8. Transferred patterns at various pressure.

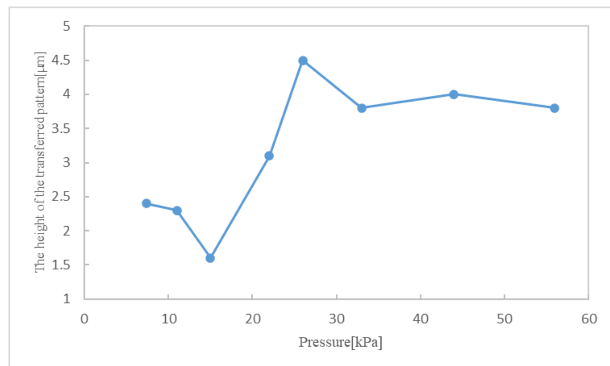

Fig. 9. Relation between transfer pattern and pressure.

Figure 9 shows the relationship between the replication patterns and pressure. The height of the transferred pattern increased as the pressure increased to approximately 30 kPa. At pressures greater than 30 kPa, the height did not increase and remained constant. This indicates that the mold was completely filled with UV-curable resin. Figs. 8 and 9 confirm that 33 kPa is required to completely fill a release-treated tube of 5 × 5 µm square and 2 µm long with UV-curable resin.

4. Conclusion

Using SU-8, a photoresist, as an electron beam resist, we fabricated a bridging structure with a high bridge height. The higher the transfer pressure, the greater the height of the transferred pattern. The transfer pattern became bumpy when the pressure was over 3.3 × 10 kPa. As a future prospect, we plan to change the transfer pressure finely and fabricate a bridging structure that reduces the aperture size a so that the relationship between the transfer pressure and θ can be investigated.

COPY

References

1. Y. Ishii and J. Taniguchi, *Microelectron. Eng.,* **84** (2007) 912.
2. N. Unno, J. Taniguchi, and Y. Ishii, *J. Vac. Sci. Technol. B*, **25** (2007) 2361.
3. L. J. Guo, *J. Phys. D: Appl. Phys.,* **37** (2004) 11.
4. S. Zankovych, T. Hoffmann, J. Seekamp, J.-U. Bruch, and C. M. S. Torres, *Nanotechnology,* **12** (2001) 2.
5. C. M. S. Torres, S. Zankovych, J. Seekamp, A. P. Kam, C. C. Cedeño, T. Hoffmann, J. Ahopelto, F. Reuther, K. Pfeiffer, G. Bleidiessel, G. Gruetzner, M. V. Maximove, and B. Heidari, *Mater. Sci. Eng. C,* **23** (2003) 23.
6. H. Hiroshima and M. Komuro, *Jpn. J. Appl. Phys.,* **46** (2007) 6391.
7. M. Fukuhara, J. Mizuno, M. Saito, T. Homma, and S. Shoji, *IEE. J. Trans.,* **2** (2007) 307.
8. D. Morihara. *Microelectoronics and Nanometer Structures Processing, Measurement, and Phenomena,* **27** (2009) 2866.
9. J. Taniguchi, K. Machinaga, N. Unno, and N. Sakai, *Microelectron. Eng.,* **86** (2009) 676.
10. M. Okada, D. Yamashita, N. Unnno, and J. Taniguti, *Microelectron. Eng.*, **123** (2014) 117.
11. F. A. Houle, C. T. Rettner, D. C. Miller, and R. Sooriyakumaran, *Appl. Phys. Lett.,* **90** (2007) 213103.
12. F. A. Houle and E. Guyer, *Microelectoronics and Nanometer Structures Processing, Measurement, and Phenomena,* **25** (2007) 1179.
13. K. Osari, N. Unno, J. Taniguchi, K. Machinaga, T. Ohsaki, and N. Sakai, *Microelectron. Eng.,* **87** (2010) 918.
14. Y. Matsubara, J. Taniguchi, and I. Miyamoto, *Jpn. J. Appl. Phys.,* **45** (2006) 5538.
15. E. Delamarche, A. Bernard, H. Schmid, A. Bietsch, B. Michel, and H. Biebuyck, *J. Am. Chem. Soc.,* **120** (1998) 500.
16. J. H. Jeong, Y. S. Choi, Y. J. Shin, J. J. Lee, K. T. Park, E. S. Lee, and S. R. Lee, *Fibers Polym.,* **3** (2002) 113.
17. C. Thanner and M. Eibelhuber, *Nanomaterials,* **11** (2021) 822.
18. N. Chaix, C. Gourgon, S. Landis, C. Perret, M. Fink, F. Reuther, and D. Mecerreyes, *Nanotechnology*, **17** (2006) 4082.
19. J. B. Lee, K. Choi, and K. Yoo, *Micromachines,* **6** (2015) 1.
20. C. H. Lin, G. B. Lee, B. W. Chang, and G. L. Chang, *J. Micromech. Microeng.,* **12** (2002) 590.

Journal of Photopolymer Science and Technology
Volume 36, Number 2 (2023) 77 − 81 ©2023SPST

Transfer Durability of Re-release Coated Replica Mold on Ultraviolet Nanoimprint Lithography

Tomohito Wakasa[1] and Jun Taniguchi[1*]

[1] *Department of Applied Electronics, Tokyo University of Science, 6-3-1Niijuku, Katsushika-ku, Tokyo 125-8585, Japan*
**junt@te.noda.tus.ac.jp*

In recent years, the scaling of semiconductors, optical devices, and other devices has led to a demand for technologies to efficiently produce microstructures. Consequently, nanoimprint lithography, commonly known as NIL, has gained particular attention. However, NIL has several limitations, and one main drawback is that the repeated use of the mold causes the release layer to deteriorate, and resin adhesion renders the mold unusable. A solution to this problem is to predict at which usage cycle resin adhesion occurs to the mold and to perform the mold release treatment again before the resin adhesion occurs. Using the line and space (L&S) pattern mold, the lifetime of the replica mold was determined after the first and second re-release treatments. Re-release treatment resulted in a higher contact angle of the replica molds and extended their lifetime.

Keywords: Nanoimprint lithography (NIL), Transfer durability, Re-release treatment, Adhesion, Mold, Surface contact angle

COPY

1. Introduction

Ultraviolet nanoimprint lithography (UV-NIL) is a powerful tool in nanoscale fabrication owing to its capability to produce nanoscale patterns in few steps [1-4]. UV-NIL is a nanoscale pattern-transfer process that uses a release-coated mold with nanoscale patterns and a UV-curable resin [5]. UV-NIL has recently been used not only to pattern resins but also to transfer silver ink and fabricate devices [6-13]. In UV-NIL, the patterned mold is directly contacted with the UV-curing resin, which causes resin adhesion, leading to the formation of defects in the mold [14-15]. A mold is usually made of an expensive material, such as Si, which is time- and labor-intensive to process [16]. The surface of the mold can be coated with a release agent to prevent defect formation. As molds are used repeatedly, the durability of the release coating is of high significance [17-19]. In our previous study, a line and space (L&S) patterned mold was used to ensure the durability and lifetime of the release agent [20]. A brief explanation of this method is as follows. As the release coating on the mold is damaged after repeated UV-NIL transfers [21], the water contact angle (CA) of the mold surface decreases with repeated transfers. In the case of the L&S patterned mold, water flows along line grooves under the capillary force, and the CA of water along the line pattern is reduced compared with that across the line pattern. Using this differential CA trend, the lifetime and durability of the release coating layer on the mold can be determined. Generally, the release agent is used at a low concentration of ~0.1 wt%; however, the characteristic of the release agent at further lowered release agent concentrations is unknown. In this study, the properties of low-concentration release were investigated using replica molds with a 100 nm L&S pattern. We also investigated the possibility of increasing the number of transcripts by applying the release treatment again, before the replica mold became unusable.

2. Materials and methods

Figure 1 shows the fabrication process of the replica mold. UV-curable resin, PAK-01-CL (Toyo Gosei, Tokyo, Japan) was dropped onto a Si master mold (Toppan, Tokyo, Japan) with an L&S pattern having a line width of 100 nm (Fig. 1a). PAK-01-CL was then spread on the Si master mold by pressing with a polyester film (Cosmoshine A4300; Toyobo, Osaka, Japan). It was then cured by UV irradiation at a dose of 180 mJ/cm^2 (Fig. 1b). The

Received March 30, 2023
Accepted May 16, 2023

mold was then released, and the replica mold was collected (Fig. 1c).

After the fabrication of the replica mold, a mold release treatment was performed on its surface to improve release. Specifically, a Cr layer was deposited on the mold surface, and the mold was immersed in the mold release agent, Optool DSX (Daikin, Osaka, Japan), which is hereafter referred to as Optool, for 30 min. In this treatment, an Optool concentration of 0.01 wt% was used (Fig. 1d). Subsequently, the mold was heated to 85 °C for 15 min (Fig. 1e). Finally, the mold was rinsed with Novec 7300 (3M) for 5 min (Fig. 1f).

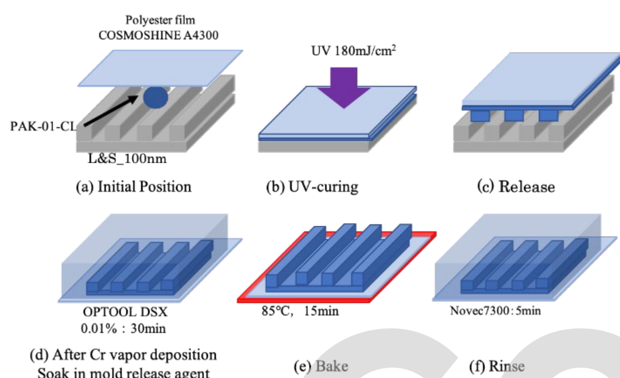

Fig. 1. Fabrication process of the replica mold

The durability of the replica mold was evaluated by repeating the transfer process using a machine (Mitsui Electric Co., Ltd., Chiba, Japan), as illustrated in Fig. 2. For this, PAK-01-CL was dropped onto the replica mold (Fig. 2a) and pressurized at 0.3 MPa for 7 s to fill the mold with the resin (Fig. 2b). Then, the pressure was maintained and the mold with resin was irradiated with UV light at a dose of 560 mJ/cm^2 (Fig. 2c). Subsequently, the mold was released (Fig. 2d). These processes (shown in Fig. 2a–d) were repeated several times.

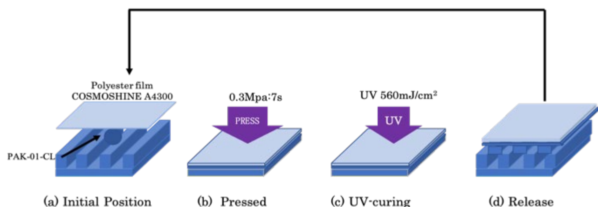

Fig. 2. Process of repeated transcription

To evaluate the release performance of the replica mold, the water CA on its surface was measured using a CA measurement system (Drop Master 701, Kyowa Interface Science, Niiza City, Japan) with various imprint numbers.

The CA was measured using 2 µL water droplets. In this experiment, the CAs along the x-direction (CA along the line pattern) and y-direction (CA across the line pattern) were measured by rotating the replica mold by 90° as shown in Fig. 3.

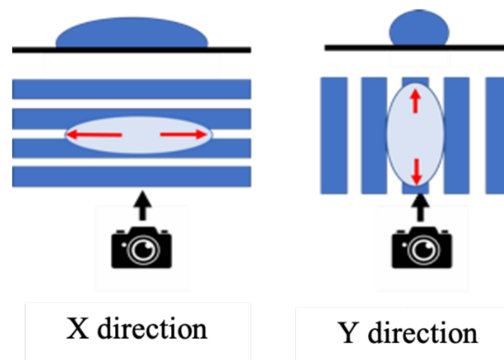

Fig. 3. Measurement of the contact angle along x- and y-directions

3. Results

3.1 Measurement of the life-time of the release-coated replica mold

First, the lifetime of the untreated replica mold (without the release agent) was investigated.

The results of the transfer durability tests conducted on replica molds treated with 0.01 wt% Optool are shown in Figure 4, where the horizontal axis represents the number of repeated transfers and the vertical axis represents the CAs in the x- and y-directions. The CA along the x-direction decreased after a relatively low number of transfers, and the CA value saturated at ~36° after approximately 200 transfers. On the other hand, the CA along the y-direction decreased gradually and proportionally with a slope of −0.085 from the 200th to 450th transfers. The CAs along the x- and y-directions intersected at the 450th transfer when resin adhesion to the replica mold surface could be visually confirmed.

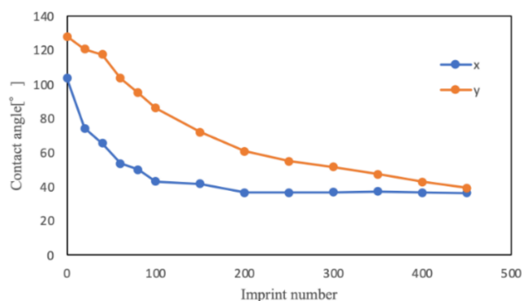

Fig. 4. Results of the transfer durability tests of the replica mold treated with 0.01 wt% of Optool DSX

COPY

Figure 5 displays a scanning electron microscopy (SEM) image of the L&S pattern transferred from the replica mold treated with 0.01 wt% Optool. The image reveals that the L&S pattern was retained until the 400th transfer (Fig. 5c), and a defective pattern was obtained at the 450th transfer (Fig. 5d), when resin adhesion occurred. This result indicates that the life of the replica mold can be predicted by determining the intersecting point of the CA along the x- and y-directions, even when the density is low. This analysis reveals that the transfer lifetime of a replica mold without the re-release treatment corresponds to 450 transfers.

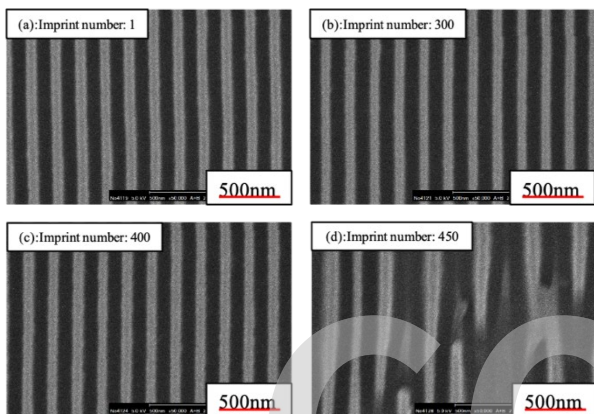

Fig. 5. Patterns transferred from a replica mold treated with 0.01 wt% of Optool. (a) After first transfer, (b) 300 transfers, (c) 400 transfers, (d) 450 transfers

COPY

3.2 Replica mold with one re-release coating

Figure 6 shows the results of the transfer durability tests of a replica mold subjected to a re-release treatment with Optool. For treatment, an Optool concentration of 0.01 wt%, which is same as that used in the first treatment, was used without Cr deposition. Before the re-release process, the CA along the x-direction decreased faster than that along the y-direction and saturated at approximately 40° after the 100th transfer. On the other hand, the CA along the y-direction decreased gradually. The re-release treatment was carried out after 300 transfer cycles, before the CAs along the x- and y-directions intersected. After the re-release treatment, the CAs along the x- and y-directions increased. The CAs along the x- and y-directions were 105.4° and 125.5°, respectively, higher than the initial CAs along the two directions. The CA along the x-direction decreased sharply from the 300th transfer onward up to the 450th transfer and exhibited a non-monotonic trend between the 450th and 1000th transfers. It however remained unchanged on average. The CA along the y-direction decreased linearly from ~90° to a value close to that along the x-direction, which was saturated. At this point, slight resin adhesion was observed on the replica mold.

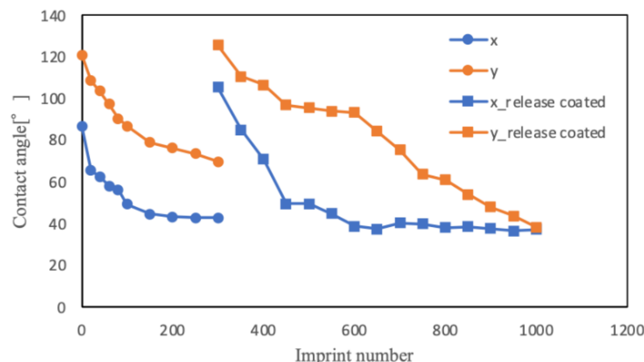

Fig. 6. Results of the transfer durability tests of the replica mold subjected to a re-release process using an Optool concentration of 0.01 wt%

Figure 7 presents a SEM image of the L&S pattern transferred from the replica mold. The morphology of the pattern reveals that the 1000th transferred pattern (Fig. 7d), which approximately corresponds to the intersection of the CAs along the x- and y-directions, was distorted. This result indicates that the re-release treatment extends the lifetime of the mold.

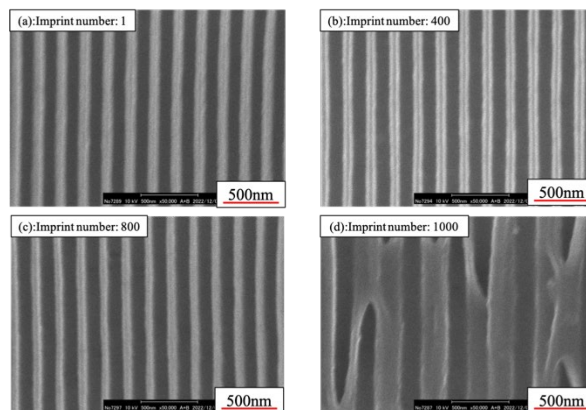

Fig. 7. SEM images of the patterns transferred from a replica mold subjected to re-release treatment using 0.01 wt% Optool. (a) After first transfer, (b) 400 transfers, (c) 800 transfers, (d) 1000 transfers

3.3 Replica mold with two re-release coatings

Figure 8 shows the results of the transfer durability test of a replica mold subjected to two re-release treatments using an Optool concentration of 0.01 wt%. The re-release treatments were conducted

after 300 and 700 transfers. After the first re-release treatment, the CA along the x-direction saturated between the 650th and 700th transfers. A second re-release treatment was then performed, before the intersection of the CAs along the x- and y-directions. After the second re-release treatment, the CAs along the x- and y-directions increased to 78.3° and 94.6°, respectively. Compared with the CAs measured after the first treatment, the second re-release process did not increase the CAs. The CA along the x-axis saturated between the 750th and 1250th transfers, although it changed only slightly. As described in Sections 3.1 and 3.2, the CA along the y-direction decreased linearly from the 800th to 1250th transfers. A defect was observed in the replica mold, almost corresponding to the intersection of the CAs along the x- and y-directions.

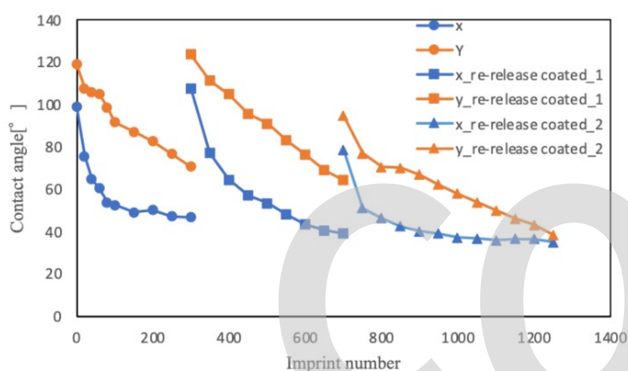

Fig. 8. Transfer durability result of the twice re-released mold with Optool concentration of 0.01 wt%

Figure 9 shows the SEM images of the L&S patterns transferred from the replica mold subjected to the second re-release treatment. The line pattern was broken at the 1250th transfer (Fig. 9d), when the CAs along the x- and y-directions intersected. The results reveal that the second re-release treatment significantly extended the lifetime of the mold compared with that after the first re-release treatment. The experiments revealed that the CAs along the x- and y-directions were restored after the first re-release treatment, but they were not restored sufficiently after the second re-release treatment. This could be attributed to the reduced ability of the replica mold to retain the release agent owing to repeated transfers. This is possibly because of the reduction in the number of -OH groups on the surface, as they are necessary for silane coupling reaction. The loss of -OH groups can occur due to the transfer or breakage of the molecular chains of the silane coupling agent and masking of the -OH groups. The origin of this can be determined by surface analysis, such as X-ray photoelectron spectroscopy, which will be the subject of a future study.

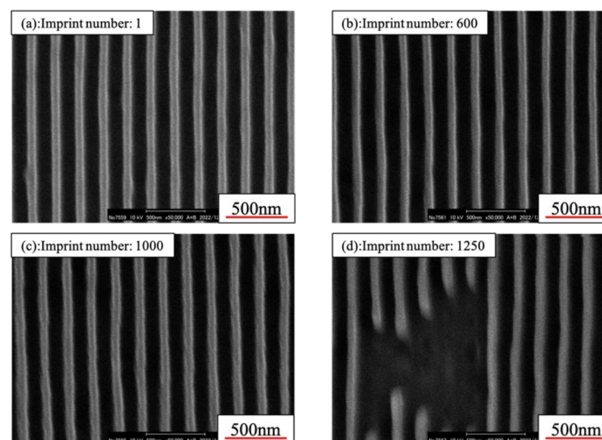

Fig. 9. SEM images of the patterns transferred from a replica mold subjected to two times of Optool treatment at 0.01 wt%. (a) After first transfer, (b) 600 transfers, (c) 1000 transfers, (d) 1250 transfers

Table 1 presents the lifetimes of the mold after different number of re-release treatments. The data reveal that the re-release treatment increases the lifetime of the replica mold. The lifetime doubled with a single release treatment, but did not triple with the second re-release treatment. This is because the CA of the mold surface was not restored sufficiently after the second re-release treatment. Thus, it can be concluded that one re-release treatment is effective for extending the lifetime of the mold.

Table 1. Number of transfers per re-release process.

Number of re-released processes	Number of transfers to lifetime
0	450
1	1000
2	1250

4. Conclusion

By analyzing the contact angles along the x- and y-directions, it was possible to predict the lifetime of the mold with the L&S pattern and then extend it by conducting a re-release treatment after an appropriate number of transfer processes. The effects of the first and second re-release treatments were investigated, and the results indicated that the second re-release treatment does not sufficiently restore the surface contact angle and hence does not significantly increase the lifetime of the mold. Therefore, one re-release treatment was determined to be effective.

COPY

Reference

1. S. Y. Chou, P. R. Krauss, and P. J. Renstrom, *J. Vac. Sci. Technol.* B, **14** (1996) 4129.
2. M. Bender A. Fuchs, U. Plachetka, and H. Kurz., *Microelectron. Eng.*, **83** (2006) 827.
3. T. Bailey, B.J. Choi, M. Colburn, M. Meiss l, S. Shaya, J.G. Ekerdt, S.V. Sreenivasan, and C. G. Willson, *J. Vac. Sci. Technol. B*, **18** (2000) 3572.
4. N. Unno, J. Taniguchi, and Y. Ishii, *J. Vac. Sci. Technol. B*, **25** (2007) 2361.
5. J. Taniguchi, T. Kawasaki, Y. Tokano, Y. Kogo, I. Miyamoto, M. Komuro, H. Hiroshima, N. Sakai, and K. Tada, *Jpn. J. Appl. Phys.*, **41** (2002) 4194.
6. K. Enomoto and J. Taniguchi, *Jpn. J. Appl. Phys.,* **62** (2023) SG1011.
7. H. Wadayama, T. Okabe, and J. Taniguchi, *Microelectron. Eng.,* **193** (2018) 47.
8. N. Sato and J. Taniguchi, *Microelectron. Eng.,* **193** (2018) 79.
9. S. Senzaki, T. Okabe, and J. Taniguchi, *Microelectron. Eng.,* **258** (2022) 111776.
10. N. Unno and J. Taniguchi, Microelectron. Eng., **88** (2011) 2149.
11. H. Yoshikawa, J. Taniguchi, G. Tazaki, and T. Zento, *Microelectron. Eng.*, **112** (2013) 273.
12. S. Barcelo and Z. Li, *Nano Converg.,* **3** (2016) 21.
13. J. Chen, Y. Zhou, D. Wang, F. He, V. M. Rotello, K. R. Carter, J. J. Watkins, and S. R. Nugen, *Lab Chip*, **15** (2015) 3086.
14. M. S. Kim, B. K. Kang, M. Ramachandran, J. K. Kim, B. K. Lee, and J. G. Park, *Microelectron. Eng.,* **114** (2014), 126.
15. J. Perumal, T. H. Yoon, H. S. Jang, J. J. Lee, and D. P. Kim, *Nanotechnology,* **20** (2009) 055704.
16. P. Voisin, M. Zelsmann, C. Gourgon, and J. Boussey, *Microelectron. Eng.*, **84** (2007) 916.
17. F.A. Houlse, E. Guyer, D. C. Miller, and R. Dauskardt, *J. Vac. Sci. B,* **25** (2007) 1179
18. D. N. Markatos, K. I. Tserpes, E. Rau, S. Markus, B. Ehrhart, and Sp. Pantelakis, *Composites: Part B,* **45** (2013) 559.
19. E. J. Jang, Y. B. Park, H. J. Lee, D. G. Choi, J. H. Jeong, E. S. Lee, and S. Hyun, *Int. J. Adhes.*, **29** (2009) 662.
20. T. Marumo, S. Hiwasa, and J. Taniguchi, *Nanomaterials,* **10** (2020) 1956.
21. J. Tsuchiya, S. HIwasa, J. Taniguchi, *Microelectron. Eng.,* **193** (2018) 98.

COPY

COPY

Journal of Photopolymer Science and Technology
Volume 36, Number 2 (2023) 83 – 90 ©2023SPST

Ultraviolet-curable Material with High Fluorine Content for Biomimetic Functional Structures Achieved by Nanoimprint Lithography with Gas-permeable Template for Life Science and Electronic Applications

Rio Yamagishi[1], Sayaka Miura[1], Mano Ando[1], Yuna Hachikubo[1], Tsugumi Murashita[1], Naoto Sugino[2], Takao Kameda[2], Yoshiyuki Yokoyama[3], Yuki Kawano[3], Kaori Yasuda[1], and Satoshi Takei[1] *

[1] Department of Pharmaceutical Engineering, Toyama Prefectural University, Imizu, Toyama 939-0398, Japan
[2] Futuristic Technology Department, Sanko Gosei, Nanto, Toyama 939-1852, Japan
[3] Toyama Industrial Technology Research and Development Center, Takaoka, Toyama 933-0981, Japan
**takeis@pu-toyama.ac.jp; Tel.: +81-766567500; Fax: +81-766566131*

COPY

Fluorine materials exhibit excellent properties, such as high water repellency, low adhesion, and chemical resistance, owing to their low surface energy. They also exhibit high thermal and oxidation stability owing to the strength of the C–F bonds. Recently, in the field of life science, further improvement of the low adherence and antifouling properties of biological substances and microorganisms by imparting surface properties to fluorine materials through pattern fabrication technology has attracted considerable attention. However, fluorine materials exhibit high thermal expansion and contraction, making it difficult to apply fabrication methods, such as injection molding and hot embossing. Conventional focused ion beam and laser processing are difficult for further pattern fabrication. Here, an ultraviolet (UV)-curable material with a high fluorine content (44wt%) was created, and the pattern fabrication of 80-nm line structures was performed on the material by UV nanoimprint lithography using the gas-permeable template that can permeate the gas entrained during pressurization. The water contact angle was 127.3°, with 129.7° being the most favorable, achieved by a combination of the water-repellency characteristics of the UV-curable material with high fluorine content and fine line patterning in the nanometer range. We discovered the possibility of creating surface functions on short-chain perfluoroalkyl sulfonate (PFAS) substitutes with a relatively low impact on the environment and human body by establishing a pattern fabrication method for long-chain PFAS, which is more difficult to pattern fabricate, as a preliminary experiment.
Keywords: Fluorine material, UV nanoimprint lithography, Gas-permeable template, Highly sensitive instant UV-curing, Water repellency, Antifouling properties

1. Introduction

The creation of advanced functional structures, in which the surface of the material processed by patterning fabrication technology exhibits valuable properties, has attracted attention for life science and electronic applications. For example, the increased surface area due to pattern fabrication on the surface can be used to improve the light collection rate of solar cells and promote chemical reactions [1][2][3]. In addition, the subwavelength structure, which is shorter than the wavelength of sunlight, improves power generation and conversion efficiency [4][5]. Furthermore, the expression of functionalities on the surface of

Received April 7, 2023
Accepted May 16, 2023

materials through biomimetic structures that mimic the water-repellent structure of lotus leaves [6][7], the structural color of morpho butterflies [8][9], and the low-friction structure of shark skin [10][11] has attracted attention for biomimetic functional properties. The multiple pattern fabrication of advanced surface structures in the micrometer to nanometer range that expresses chemical and physical functions is expected to be a technology that improves the properties and added value of materials.

Fluorine materials exhibit numerous and excellent properties, such as high water and oil repellency [12][13], low friction [14], chemical resistance [15], and corrosion resistance [16], owing to their extremely low surface free energy and high chemical stability resulting from the high bond energy of the C–F bonds that form their framework [17][18]. These characteristics are used in a wide range of fields, including electronics [19][20], automotive parts [21][22], and medical and pharmaceutical fields [23][24].

Recently, in the fields of life science and biotechnology, the improvement of the low adherence and antifouling properties of biological substances and microorganisms has attracted attention [25], and the creation of fluorine materials with an unprecedented molecular structure is required. Furthermore, fluorine materials are versatile for the pattern fabrication of microfluidic devices. The microminiaturization and integration of microfluidic devices through fabrication technology are required for medical diagnosis using minute amounts of biological samples, by analysis and drug discovery [26].

In previous studies, polymeric materials with high fluorine content in the range of 50wt%–70wt%, such as polytetrafluoroethylene (PTFE) and polyvinylidene fluoride (PVDF), have been extensively studied for life science applications, such as blood contact applications [27] and catheters [28], owing to their excellent low adhesion properties.

The surface properties of acrylate-cured materials with fluorine atom content below 20wt% have been reported [29]. A previous study reported the surface properties of fluorine materials with fluorine contents below 20wt%.

Therefore, the objective of this study was to create an UV-curable material with high (44wt%) fluorine content. In addition, we added functionality to this material through ultrafine fabrication to create valuable properties, such as improved water repellency and low adhesion.

However, fluorine materials exhibit high thermal expansion and contraction, making it difficult to apply advanced pattern fabrication technologies, such as injection molding and hot embossing [30]. In addition, focused ion beam, synchrotron radiation, and laser fabrication, which are conventionally employed for the pattern fabrication of fluorine materials, require expensive equipment and facilities, as well as time-consuming processes [31]. Furthermore, laser fabrication has the disadvantages of the nonuniformity of the fabricated surface due to the nonuniformity and interference of the laser beam and difficulty in fabricating large areas because the laser beam is focused on a single point [32][33].

We employed pattern fabrication and created surface functions on high-fluorine materials by UV nanoimprint lithography, a type of pattern fabrication process. Nanoimprint lithography is a simple, high-precision, high-resolution, and large-area pattern fabrication technique [34][35] with a wide range of applications in the field of electronics [36], such as semiconductors [37][38] and solar cells [39][40], and the field of life science [41], such as microneedles [42][43] and cell culture scaffolds [44][45].

Here, we improved the nanoimprinting defects using a gas-permeable template that can remove the gas entrained between the template and material to be transferred from the porous structure of the gas-permeable template. Furthermore, we evaluated surface functions by the pattern fabrication of the UV-curable material with high fluorine content, to facilitate a smooth transition to short-chain fluorinated surfactants and alternatives [46][47], which have relatively low environmental and human impact.

2. Experimental

2.1. Synthesis of ultraviolet-curable material with high fluorine content

Fig. 1 shows the composition of the synthesized and prepared UV-curable material with high fluorine content. The UV-curable material was developed with two components: (A) tetrahydroperfluorotriethyleneglycol diacrylate (56.5wt%; Toyama Prefectural University) and (B) 4,4,5,5,6,6,7,7,8,8,9,9,10,10,11,11,11-heptadecafluoro-2-hydroxyundecyl acrylate (39wt%; Merck). In addition, (C) 2-hydroxy-2-methyl-1-phenylpropanone (4.5wt%; IGM Resins B.V.) was used as a photoinitiator. The three

COPY

components were mixed and stirred for 3 h using a MIX-ROTAR MR-5 (AS ONE). Thereafter, the UV-curable material with high fluorine content was fabricated by performing a defoaming treatment for 2 h at room temperature using a vacuum dryer (AVO-250NS, AS ONE). As shown in Fig. 1, the fluorine-containing groups in (A) and the perfluoroalkyl groups in (B) migrated to the surface to express functions, such as water and oil repellency.

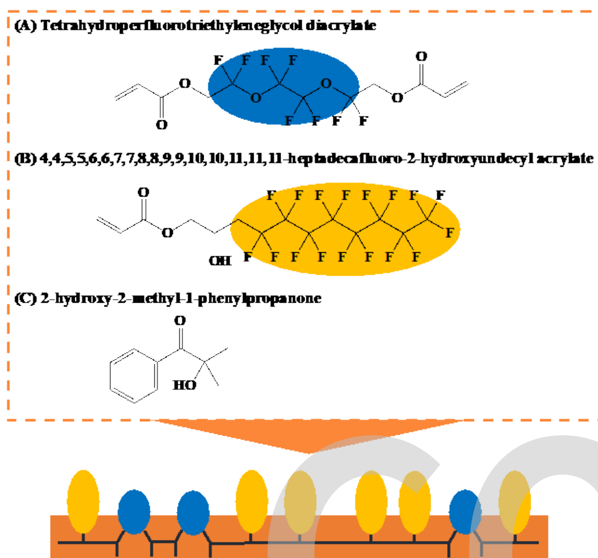

Fig. 1. Composition of UV-curable material with high fluorine content and diagram of fluorine migration on surfaces

COPY

2.2. Evaluation of crosslinking time by dynamic viscoelasticity measurements

Dynamic viscoelasticity measurements were performed using viscoelastic measurement equipment (MCR102, Anton Paar) that allows UV irradiation during measurements. The crosslinking time of the UV-curable material with high fluorine content was measured in the oscillatory rotation mode (parallel plate diameter, 12 mm; gap, 0.100 mm; frequency, 10 Hz; strain, 0.2%; temperature, 26.3℃). UV irradiation was performed using a UV spotlight source (Lightning Cure™ LC8, Hamamatsu Photonics). The intensity of the UV light was measured with a UV illuminance meter (ACCU-CAL™ 50, Dymax) to be 11 mW/cm^2. After an interval of 0–60 s without UV irradiation, UV irradiation was initiated, and measurements were performed for 400 s.

2.3. Ultraviolet nanoimprint lithography

Fig. 2 shows the nanoimprinting process of UV nanoimprint lithography.

The UV nanoimprint processes were performed in two steps: imprinting the gas-permeable template using a quartz master template and imprinting the UV-curable material using our developing gas-permeable template [48][49][50][51].

First, to perform a template release treatment, a silane coupling agent (DS-831TH, DURASURF) was applied to the surface of the quartz master template (10 mm × 10 mm), and the process was repeated twice by drying for 2 h. The quartz master template had nanostructures of lines. The gas-permeable material was dispensed on the surface of the lower layer metal, and the quartz master template was placed on the material and pressurized. The lower layer metal was made of maraging steel and exhibited a gas-permeable porous structure.

UV irradiation was performed for 1 min using a UV spotlight source (Lightning Cure™ LC8, Hamamatsu Photonics), followed by UV irradiation for 4 min using a Handy Type UV curing power supply (SunEnergy). The UV light intensities measured using a UV irradiance meter (ACCU-CAL™ 50, Dymax) were 25 and 59 mW/cm^2, respectively. The gas-permeable template with line patterns was produced after removing the quartz master template.

Next, the UV-curable material with high fluorine content was dispensed on the surface of the gas-permeable template, and a glass slide (S3233, Matsunami Glass Industry) was placed on the material and pressurized.

UV irradiation was performed for 1 min using the UV spotlight source (Lightning Cure™ LC8, Hamamatsu Photonics), followed by UV irradiation for 1 min using a Handy Type UV curing power supply (SunEnergy). The nanostructures of the UV-curable material with high fluorine content were produced after removing the gas-permeable template. Furthermore, the process of patterning on the UV-curable material was repeated 30 times using the same gas-permeable template.

For comparison, the patterning of the UV-curable material with high fluorine content was directly performed from the quartz master template. The UV curing time was the same as that for the second nanoimprinting process. The nanoimprinting results were observed by scanning probe microscope (SPM) to evaluate the surface of the line patterning nanostructures of the UV-curable material.

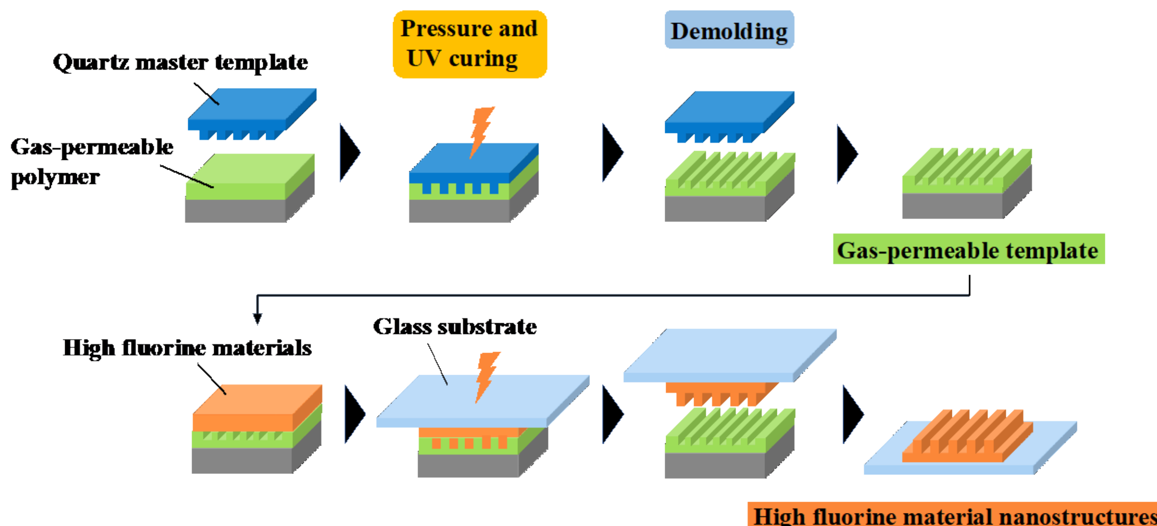

Fig. 2. Two-step nanoimprinting process by UV nanoimprint lithography

2.4. Water contact angle measurements

The water contact angles on the films of the UV-curable material with high fluorine content without surface nanostructures and those of the UV-curable material with high fluorine content with surface nanostructures were measured to evaluate the water repellency. A fully automatic contact angle meter (Drop Master DM500, Kyowa Interfacial Science) was used to measure the water contact angle using the θ/2 analysis method. The drop volume was 1.0 μL, and the measurement began immediately after the drop. The measurements were performed in an environment with a temperature of 25°C. The 1st and 10th measurements were omitted, and the average value of the water contact angle was calculated. Five measurements of 9 s each were obtained, and the average value of the water contact angles was calculated. The water contact angle measurements were conducted from a direction horizontal to the line structure.

3. Results

3.1. Crosslinking time measured using a dynamic viscoelasticity measurement device

Fig. 3 shows the results of the dynamic viscoelasticity measurements of the prepared UV-curable material with high fluorine content. The horizontal axis represents the UV-curing time (s), and the vertical axis represents the storage modulus (MPa).

After the UV irradiation of the UV-curable material, the storage modulus rapidly increased from the uncured state, reaching 80% of the maximum storage modulus at 100 mJ. The UV-curable material with high fluorine content is expected to be applied to life science and electronics as one of the highly sensitive instant UV-curing products. The concentration of C=C bonds in the high-fluorine material was calculated to be 8%.

A previous study reported that the elastic modulus reached 80% of the maximum storage modulus at 90 mJ in a radical light-cured resin with a 10% concentration of C=C bonds [52].

Compared with this previous study, there was no significant difference in the UV curing speed even with high fluorine content, although the UV curing of the UV-curable material was slightly slower because of the effect of fluorine and the type of initiator.

After approximately 300 s, the storage modulus reached a plateau for all the measurements.

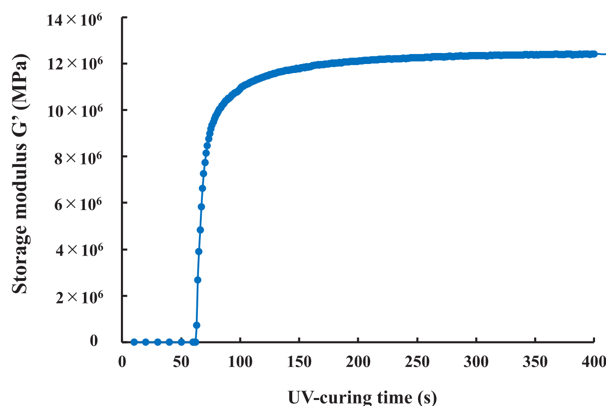

Fig. 3. Storage modulus of UV-curable material with high fluorine content

COPY

3.2. Nanoimprinting results of the UV-curable material with high fluorine content and repeated fabrication

Fig. 4. shows the SPM images of the template surfaces and the line patterning nanostructures of the UV-curable material with high fluorine content. The following are shown. (a) Quartz master template with line patterns, (b) gas-permeable template imprinted using (a), (c) patterning error of the UV-curable material with high fluorine content imprinted using (a), (d) results of the 1st transfer to the UV-curable material using (b), (e) results of the 15th transfer, and (f) results of the 30th transfer. The results of the patterning sizes were (a) width, 80 nm ± 2 nm; height, 160 nm ± 4 nm; (b) width, 86 nm ± 9 nm; height, 151 nm ± 13 nm; (c) width, 69 nm ± 21 nm; height, 148 nm ± 13 nm; (d) width, 83 nm ± 9 nm; height, 157 nm ± 11 nm; (e) width, 79 nm ± 8 nm ± 10 nm; and (f) width, 82 nm ± 9 nm; height, 155 nm ± 11 nm.

The results of imprinting the UV-curable material with high fluorine content using (a) showed that the groove width was narrower than the quartz master template, and uniform line patterning was not achieved. Such nanoimprinting defects are caused by gases, such as nitrogen and oxygen, which prevent the cross-linked liquid material from filling the template during UV-curing.

Conversely, the gas-permeable template (b) formed superior nanoscale patterns compared with those of the non-gas-permeable quartz master template. We successfully demonstrated an excellent approximately 80 nm dense-line patterning of the UV-curable material during the UV nanoimprint lithography using the gas-permeable template. The porous molecular structure of the gas-permeable template was speculated to be the cause of the reduction in the severity of the pattern failure density factors, such as the nonuniform line pattern size.

In addition, no significant difference was observed in the line patterning nanostructures of the UV-curable material in the results of the (d) 1st, (e) 15th, and (f) 30th fine pattern formation in the basic laboratory-level manual nanoimprint lithography processes, such as dispensing, imprinting, and demolding. The results indicated the excellent release of the gas-permeable template and the UV-curable material with high fluorine content. Further improvement in the number of transfers and low costs are expected owing to the use of automated nanoimprinting equipment.

Although the accumulation of perfluoroalkyl sulfonate (PFAS) in the environment and human body is an issue, we discovered the possibility of creating surface functions on short-chain PFAS substitutes with a relatively low impact on the environment and human body by establishing a pattern fabrication method for long-chain PFAS, which is more difficult to pattern fabricate, as a preliminary experiment.

3.3. Water contact angle measurement results

Fig. 5 shows the results of the water contact angle measurements. The average water contact angle of the UV-curable material with high fluorine content without surface nanostructures was 104.1°. However, the water contact angle of the UV-curable material with surface nanostructures was 127.3°, with 129.7° being the most favorable. The preparation of line patterns on the surface of the UV-curable material can increase the water contact angle by approximately 20° compared with that of the smooth UV-curable material.

COPY

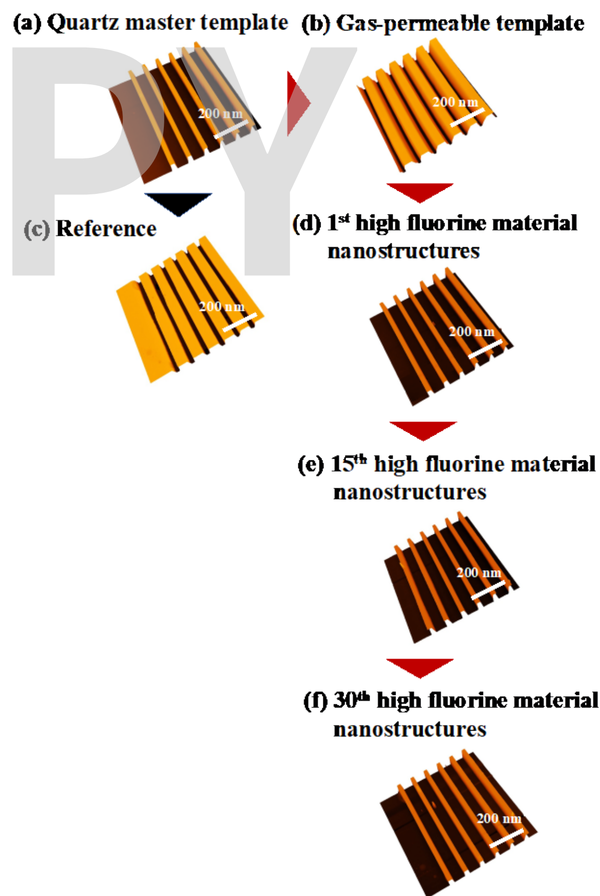

Fig. 4. SPM images of template surfaces and line patterning nanostructures of UV-curable material with high fluorine content

In a previous study, it was reported that the water contact angle improved from approximately 10° to approximately 90° by imparting micrometer line patterns on polyglycolic acid [53]. Here a further improvement in the water contact angle was achieved by combining the water-repellency characteristics of the UV-curable material with fine patterning in the nanometer range.

It has also been reported that nanostructures, such as pillars and protrusions, significantly improve the contact angle compared with line patterns [54].

We performed the microfabrication and evaluation of the line patterns to evaluate the resolution. Further improvement of the surface properties was expected from the addition of microstructures, such as pillars and protrusions.

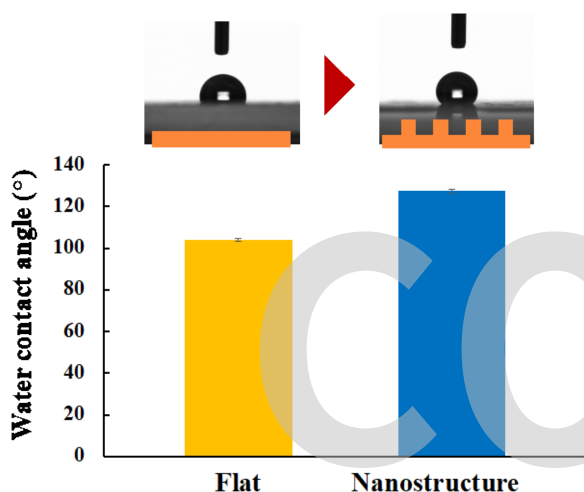

Fig. 5. Comparison of contact angles of UV-curable material with high fluorine content

4. Conclusion

We succeeded in the ultrafine fabrication of a UV-curable material with high fluorine content (44wt%) with photoreactive groups by nanoimprint lithography with a gas-permeable template. Furthermore, the combination of fluorine materials with low surface energy properties and nanoimprinting processes in the nanometer range increased the water contact angle, demonstrating improved water repellency and low adhesion. This result was achieved by the chemistry of the fluorine material and the expression of surface functionalities through the imposition of nanostructures. The patterning of the UV-curable material is expected to be useful for a wide range of applications in the field of electronics, such as semiconductors and displays, and the field of life science. In addition, it has the potential to improve the added value of materials.

Acknowledgements

The author, Rio Yamagishi, is deeply grateful to the member of Hayashi Rheology Memorial Foundation 2022-2024, and the family of TAU scholarship 2023. This industry-academia-government collaboration was financially supported by the Japan Science and Technology Agency Adaptable and Seamless Technology Transfer Program No. JPMJTR192C, the Japan Society for the Promotion of Science Bilateral Joint Research Projects No.120229937 with Belgium and No. 120199971 with the U.S.A., a Toyama Prefecture Grant 2021–2023, Iketani Science and Technology Foundation, the Takeuchi Foundation, the Amada Foundation, the Ame Hisaharu Foundation, the Die and Mould Technology Promotion Foundation, Ogasawara Foundation, Lotte Foundation, KOSE Cosmetology Research Foundation, TOBE MAKI Scholarship Foundation 2022-2023.

References

1. C. Wu, K. Wang, M. Batmunkh, A. S. Bati, D. Yang, Y. Jiang, Y. Hou, J. G. Shapter, and S. Priya, *Nano Energy*, **70** (2020) 104480.
2. H. Liu, Y. Du, X. Yin, M. Bai, amd W. Liu, *J. Nanomater.*, **2022** (2022)
3. Z. Gao, G. Lin, Y. Chen, Y. Zheng, N. Sang, Y. Li, L. Chen, and M. Li, *Sol. Energy*, **205** (2020) 275.
4. H. J. Choi, D. Huh, J. Jun, and H. Lee, *Appl. Spectrosc. Rev.*, **54** (2019) 719.
5. Z. Teng, Y. Sun, F. Kong, Y. Jin, Y. Liu, Y. Wang, Y. Zhang, H. Cao, Z. Xu, H. He, and J. Shao, *Opt. Laser Technol.*, **145** (2022) 107487.
6. N. A. Patankar, *Langmuir*, **20** (2004) 8209.
7. W. Barthlott, and C.Neinhuis, *Planta*, **202** (1997) 1.
8. S. Kinoshita, S. Yoshioka, and K. Kawagoe, *Proc. Royal Soc. B*, **269** (2002) 1417.
9. S. Niu, B. Li, Z. Mu, M. Yang, J. Zhang, Z. Han, and L. Ren, *J. Bionic Eng.*, **12** (2015) 170.
10. L. Wen, J. C. Weaver, and G. V. Lauder, *J. Exp. Biol.*, **217** (2014) 1656.
11. G. D. Bixler, and B. Bhushan, *Adv. Funct. Mater.*, **23** (2013) 4507.
12. T. Chen, J. Hong, C. Peng, G. Chen, C. Yuan, Y. Xu, B. Zeng, and L. Dai, *Carbohydr. Polym.*, **208** (2019) 14.
13. X. Zheng, Y. Tang, and Y. Bai, Eur. *Polym. J.*, **175** (2022) 111324.
14. A. A. Riskulov, G. B. Yuldasheva, and O. T. Toirov, *WoS: Int. Sci. Res. J.*, **3** (2022) 1670.
15. Y. Guo, S. Li, B. Su, and B. Mandal, *Chem. Eng.*

COPY

J., **369** (2019) 498.
16. X. Jiang, W. Wan, B. Wang, L. Zhang, L. Yin, H. Van Bui, and J. Xie, L. Zhang H. Lu, L. Deng, *Appl. Surf. Sci.*, **572** (2022) 151320.
17. S. Dehnen, L. L. Schafer, T. Lectka, and A. Togni, *Inorg. Chem.*, **60** (2021) 17419.
18. R. Berger, G. Resnati, P. Metrangolo, E. Weber, and J. Hulliger, *Chem. Soc. Rev.*, **40** (2011) 3496.
19. Y. Yang, Y. Hong, and X. Wang, *ACS Appl. Mater. Interfaces*, **13** (2021) 8682.
20. G. Zhang, C. Wang, L. Jiang, Y. Wang, B. Wang, X. Wang, H. Liu, L. Zong, J. Wang, and X. Jian, *Polymers*, **15** (2023) 1531.
21. T. Yin, Q. Fu, L. Zhou, Y. Fu, and L. Qi, *Tribol. Int.*, **142** (2020) 106001.
22. Y. Miki, T. Fukunaga, S. Yamagishi, and I. Kuwayama, *SEI Tech. Rev.*, **88** (2019) 99.
23. R. Koguchi, K. Jankova, and M. Tanaka, *Acta. Biomater.*, **138** (2022) 34.
24. K. Yonezawa, M. Kawaguchi, A. Kaneuji, T. Ichiseki, Y. Iinuma, K. Kawamura, K. Shintani, S. Oda, M.Taki and N. Kawahara, *Antibiotics*, **9** (2020) 495.
25. G. Cai, F. Liu, and T. Wu, *Colloids Surf. B*, **202** (2021) 111667.
26. D. Liu, Y. Wang, X. Li, M. Li, Q. Wu, Y. Song, Z. Zhu, and C. Yang, *Aggregate*, **3** (2022) e184.
27. V. M. Vijayan, B. S. Tucker, P. T. Hwang, P. S. Bobba, H. W. Jun, *S. A. Catledge*, Y. K.Vohra, and V. Thomas, *J. Mater. Chem.* B, **8** (2020) 2814.
28. L. Wang, S. Zhang, R. Keatch, G. Corner, G. Nabi, S. Murdoch, F. Davidson, and Q. Zhao, *J. Hosp. Infect.*, **103** (2019) 55.
29. K. Li, P. Wu, and Z. Han, *Polymer*, **43**(2002). 4079.
30. Y. Zhang, M. J. Yin, X. Ouyang, A. P. Zhang, and H. Y. Tam, *Appl. Mater. Today*, **19** (2020) 100580.
31. W. Li, K. Liu, Y. Zhang, S. Guo, Z. Li, and S. C. Tan, *Chem. Eng. J.*, **446** (2022) 137195.
32. A. Cherala, P. N. Pandya, K. M. Liechti, and S. V. Sreenivasan, *Microsyst. Nanoeng.*, **7** (2021) 13.
33. M. Modaresialam, Z. Chehadi, T. Bottein, M. Abbarchi, and D. Grosso, *Chem. Mater.*, **33** (2021) 5464.
34. S. Y. Chou, P. R. Krauss, and P. J. Renstrom, *JVST B*, **14** (1996) 4129.
35. N. Atthi, M. Dielen, W. Sripumkhai, P. Pattamang, R. Meananeatra, P. Saengdee, O. Thongsook, N. Ranron, K. Pankong, W.Uahchinkul, J. Supadech, N. Klunngien, W. Jeamsaksiri, P.Veldhuizen, and J. M. Ter Meulen, *Nanomaterials*, **11** (2021) 339.
36. K. Kurematsu, S. Takei, S. Nakajima, K. Mizui, S. Takamatsu, D. Hirata, and M. Hanabata, *Microelectron. Eng*, **216** (2019) 111085.
37. K. Kobayashi, H. Torii, M. Hiura, Y. Takabayashi, A. Kimura, Y. Suzaki, T. Ito, K. Yamamoto, J. Choi, and T. Estrada, *In Photomask Jpn. 2022: XXVIII Symp. on Photomask and Next-Gener. Lithogr. Mask Technol.*, **12325** (2022) 32.
38. H. Xu, L. Han, J. J. Su, Z. Q. Tian, and D. Zhan, *Sci. China Chem.*, **65** (2022) 810.
39. Y. Gu, J. Xu, J. Lin, H. Ma, H. Zhao, Y. Zhang, and B. Sun, *Sol. Energy*, **241** (2022) 172.
40. M. A. Yakoob, J. Lamminaho, K. Petersons, A. Prajapati, E. Destouesse, B. R. Patil, H. Rubahn, G. Shalev, J. Stensborg, and M. Madsen, *ChemSusChem*, **15** (2022) e202102618.
41. S. Takei, and M. Hanabata, *AIP Adv.*, **7** (2017). 035110.
42. S. Terashima, C. Tatsukawa, M. Suzuki, T. Takahashi, and S. Aoyagi, *Precis. Eng.*, **59** (2019) 110.
43. S. Miura, R. Yamagishi, R. Miyazaki, K. Yasuda, Y. Kawano, Y. Yokoyama, N. Sugino, T. Kameda, and S. Takei, *Gels*, **8** (2022) 785.
44. B. Nowduri, S. Schulte, D. Decker, K. H. Schäfer, and M. Saumer, *Adv. Funct. Mater.*, **30** (2020) 2004227.
45. N. Lu, X. Wang, X. Li, W. Shi, X. Wang, Y. Zou, G. Yang, X. Tang, Z. Zhang, W. Xiang, and Y. Weng, *Adv. Mater. Interfaces,* **10** (2023) 2201929.
46. L. Croce, F. Coperchini, M. Tonacchera, M. Imbriani, M. Rotondi, and L. Chiovato, *J. Endocrinol. Invest.*, **42** (2019) 1329.
47. X. Qiu, J. Li, J. Wang, X. Yang, Y. Li, and D. Qi, *Surf. Coat. Technol.*, **447** (2022) 128810.
48. R. Yamagishi, S. Miura, K. Yasuda, N. Sugino, T. Kameda, Y. Kawano, Y. Yokoyama, and S. Takei, *Appl. Phys. Express,* **15** (2022) 046502.
49. S. Takei and M. Hanabata, *Appl. Phys. Lett.*, **107** (2015) 141904.
50. S. Takei, S. Nakajima, K. Sugahara, M. Hanabata, Y. Matsumoto, and A. Sekiguchi, *Macromol. Mater. Eng.*, **301** (2016) 902.
51. S. Nakajima, S. Takei, Z. Zhou, H. Maki, K. Sugahara, M. Hanabata, Y. Matsumoto, and A. Sekiguchi, *J. Photopolym. Sci. Technol.*, **29** (2016) 189.
52. J. Sung, D. G. Lee, S. Lee, J. Park, and H. W. Jung, *Materials*, **13** (2020) 3277.

COPY

53. H. Gao, J. Xiao, Y. Wei, H. Wang, H. Wan, and. S. Liu, *ACS omega*, **6** (2021) 20931.
54. N. Kaga, H. Fujimoto, S. Morita, Y. Yamaguchi, and T. Matsuura, *Dent. J.*, **9** (2021) 124.

COPY

Journal of Photopolymer Science and Technology
Volume 36, Number 2 (2023) 91 − 96 ©2023SPST

Development of High Accurate Multi-Step Deep X-ray Exposure System Using Two-axial PZT Actuators

Taki Watanabe,[1*] Sho Amano,[1] Kaito Fujitani,[1] Akinobu Yamaguchi,[1] and Yuichi Utsumi[1]

[1]Laboratory of Advanced Science and Technology for Industry, University of Hyogo,
3-1-2 Kouto, Kamigori, Ako-gun, Hyogo 678-1205, Japan
wtaki@lasti.u-hyogo.ac.jp

Abstract

Deep X-ray Lithography (DXRL) has conventionally processed shapes that depend on the two-dimensional pattern of the X-ray mask used. In this study, we attempted to fabricate microstructures of micron-order 3D arbitrary shapes on a PMMA surface by using a high-precision multi-step exposure system with a 2-axis PZT actuators. The sample on the PZT actuator stages controlled was exposed, and a micro conical shape with a bottom diameter of 63 μm, a top diameter of 2 μm, and a height of about 70 μm was successfully fabricated. This was in accordance with the designed model and we could control micron-order processing.

Keywords: Synchrotron radiation, X-ray, LIGA, Microfabrication

COPY

1. Introduction

DXRL is a high-precision, high-aspect-ratio microfabrication method using X-rays from synchrotron radiation [1, 2]. X-rays pass through a mask with an arbitrary X-ray absorber pattern and are irradiated to a photoresist with the pattern for processing, but this can only fabricate a 2.5-dimensional shape with the pattern of the X-ray mask. Therefore, various approaches have been proposed to generate exposure distributions [3-5].

In this study, we aimed to microfabricate three-dimensional shapes by using PZT actuators making multi-step exposures on the resist surface. This is achieved by generating the exposure distribution for the desired shape by a step operation of the x-ray mask to the resist. In this paper, we report on the developed exposure system and the results of microfabrication using the system. For an example, we report on the results of microfabrication of a conical shape when a circular X-ray mask was used. The obtained machined shapes were consistent with a simple designed model, and the machining control on the order of a few microns was successfully achieved.

2. Experiments

We carried out DXRL exposure experiments at the beamline (BL11) in the New SUBARU Synchrotron

Received March 10, 2023
Accepted May 16, 2023

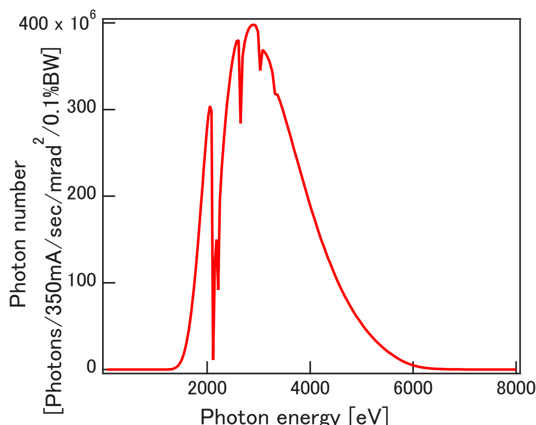

Fig. 1 Photon Flux at BL11

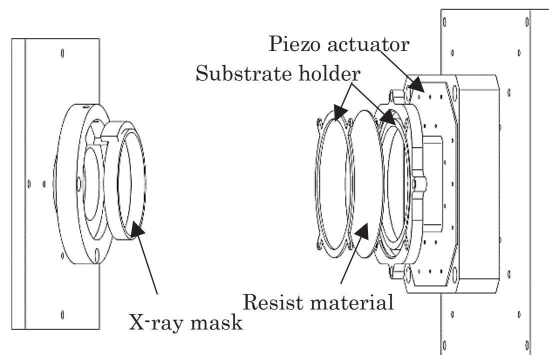

Fig.2 Overview of multi-step exposure system

Radiation Facility in the University of Hyogo. BL-11 was constructed as a dedicated eamline for the LIGA process. A bending magnet is used as a light source, and the beam is reflected by a toroidal mirror and transmitted to two Be filters[6]. X-ray energy and flux used in this experiment shows Fig.1.

A 4-axis exposure stage, which can rotate, tilt, translate in the x- and y-directions, had installed in the exposure chamber of BL-11. Additionally, we attached originally developed multi-step exposure system. This multi-step exposure system generates energy absorption distribution on the sample by moving the sample to the X-ray mask relatively. The exposure sample is fixed on two PZT actuators stages, and desired energy absorption distribution can be generated by precise movement of the PZT actuators. The developed multi-step exposure system is shown in Fig.2, and its performance is summarized in Table 1.

Table 1 Performances of multi-step exposure system

Travel range in X [μm]	200
Travel range in Y [μm]	200
System resolution [nm]	2
Bidirectional repeatability [nm]	±10
Processing area [mm]	35×35
Sample thickness [μm]	0~1000

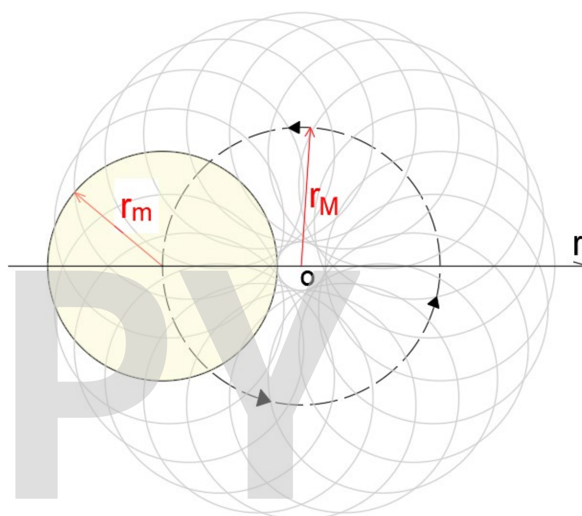

COPY

Fig.3 Trajectory of step motion of piezo actuator and calculation parameters

To test this system, we tried to fabricate a micro conical array using an X-ray mask having an array pattern of circular X-ray absorbers (Au) with a diameter of 32.4 μm and interval of 70 μm. At rest frame of the sample, the mask was moved circularly to the sample by multi-steps to fabricate the micro conical shape.

To determine the operating parameters, we calculated the energy absorption distribution on the sample surface. Trajectory of the step motion in the calculations are shown in Fig.3.

This shows a top view of the micro conical shapes. The center position of the shape is 'o', and the radius

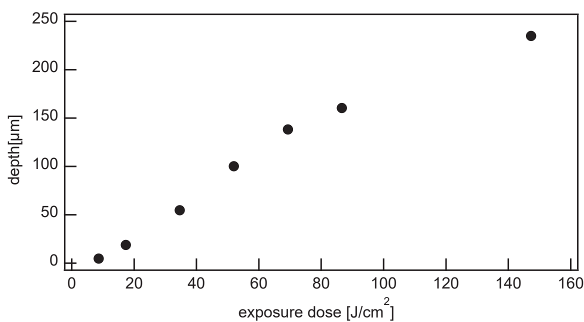

Fig.4 Exposure-dose dependence of processing depth of PMMA sheet

of the Au shield is 'r_m'. The Au shield is stepped in a circular motion by PZT actuators. The radius of this circular motion is 'r_M'. When the intensity of the irradiation beam is kept constant, the energy absorption distribution on the sample surface is determined by the exposure time. An energy absorption at a point during all exposed time is defined to be 1. While the sample is covered by the Au shielding, it is not exposed, so an energy absorption is less than 1. The absorbed energy can be calculated from time covered by the Au absorber at each 'r' point. Normalized absorbed energy at point 'r' is defined as dose rate, and expressed as shown in (1).

$$dose\ rate = 1 - \frac{1}{\pi} arccos\left(\frac{r^2 + {r_M}^2 - {r_m}^2}{2r_M \times r}\right) \quad (1)$$

Fig.4 shows the dependency of processing sample depth after development on amount of absorbed energy. At this time, the sample was PMMA. The developing time was 24 hours with GG developer at 37.8°C. Based on the calculations of energy absorption distribution on the sample surface and the measured the processing depth, a simple model of the processed shape can be predicted. In the X-ray lithography experiments, rm was fixed and r_M was set to be 10 μm, 15 μm, and 20 μm.

Table 2 Experimental conditions

Resist Material	PMMA
Thickness [μm]	200
Exposure Dose [J/cm²]	32.7
Developing Time [min]	360
Developing Temperature [°C]	37.8
Developer	GG Developer

3. Results and discussion

y operating the multi-step exposure system, we were able to fabricate a three-dimensional shape. Fig. 5 shows the designed trajectory of the X-ray mask (a), the calculated energy absorption distribution on the sample surface(b), the calculated 3D model (c), and the actual processing geometry results. For each case of Fig.5(a)~(d), left side indicates r_M=10μm case when the overlapping area of the moving mask is large, center 15μm when the overlapping area of the moving mask is small, and right 20μm when the overlapping area of the moving mask is none. In Fig.5(a), the areas that are always covered by the X-ray mask are highlighted in yellow. Table 2 summarize the experiment conditions at this time.

Table 3 indicates obtained sizes of the fabricated PMMA shapes comparing with sizes of the models and they are in good agreement. However, there are some differences in the shape, and we next discuss them.

First, let us consider the r_M = 10 μm case. The difference between the 3D model (Fig.5c, left) and the processing results (Fig.5d, left) is observed in the shape in the range of r<-20 and 20<r. In the 3D

Table 3 Comparison of 3D model and processed shape results

	r_M = 10		r_M = 15		r_M = 20	
	3D model	Processed shape	3D model	Processed shape	3D model	Processed shape
Upper circle diameter [μm]	12.3	10.0	2.4	2.0	23.5	22.0
Lower circle diameter [μm]	52.0	55.0	62.4	60.0	72.4	67.0
Height [μm]	56.0	45.2	56.0	29.7	16.8	15.6

COPY

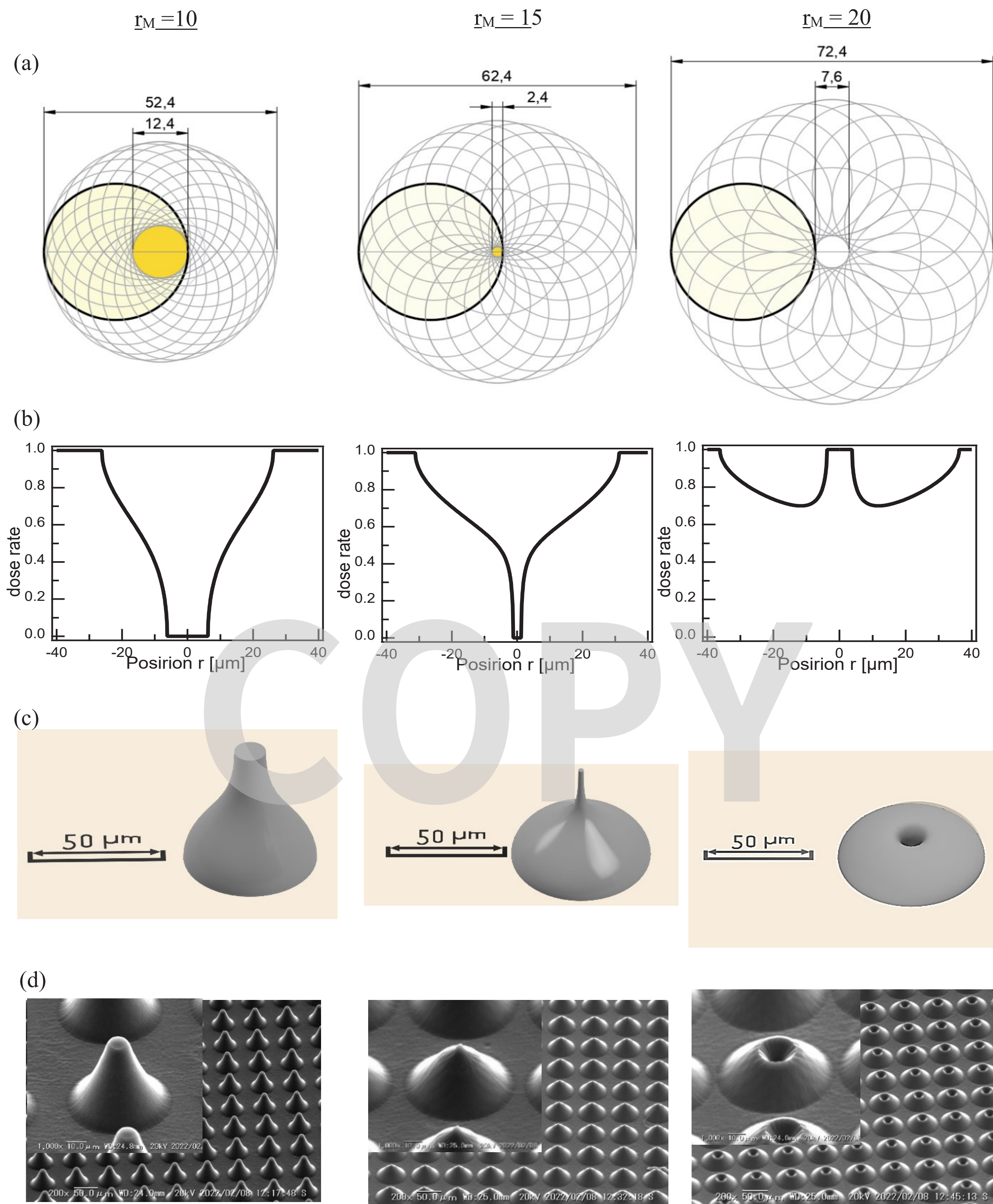

COPY

Fig.5 Geometry designs and machining results with rM=10mm (left), 15mm (center) and 20mm (right), (a)Drive trajectory of piezo actuator, (b) Absorbed energy distribution on sample surface, (c)3D model of machining geometry, (d) DXRL processing results.

model, the slope gradually increases, whereas in the processing results, the slope is more gradual. This difference can be explained by the difference in processing speed due to the difference in the amount of energy absorbed by the sample surface. The results in Fig. 4 shows that the processing speed

becomes higher at higher energy absorption. Therefore, near the outer part of the shape, where the dose rate is close to 1, the development progresses rapidly. In contrast, the development progresses slowly near the inner part of the shape. This means that the development progresses not only from the upper part of the shape but also from the lateral direction in the area. The sizes of the processed PMMA were 55 µm in diameter at the bottom, 10 µm at the top, and 45.2 µm in height.

Next, we consider the r_M = 15µm case. In this case, the rM and the rm are closest. In the 3D model (Fig.5c, center), a columnar structure can be seen in the range of the unexposed area (dose rate = 0) near the center of the pattern. However, no columnar structure can be seen in the processed shape (Fig.5d, center). Because the radius of the columnar structure is very small and has a large aspect ratio, we thought that it was damaged during the development process and lost it. The size of the processed PMMA were 60 µm in diameter at the bottom, 2 µm at the top, and 29.7 µm in height and we were successful in fabricating the microstructure as design with the multi-step exposure system we developed.

Finally, we consider the r_M = 20 µm case. In this case, the rm is larger than the rM. Therefore, the area around the pattern center of the conical shape is always exposed by X-rays. As a result, a hole shape is processed at the center of the shape. This is evident in the processing results. However, the entrance of the hole shape is different between the 3D model (Fig.5c, right) and the processing results (Fig.5d, right). This difference can be attributed to the difference in processing speed due to the difference in energy absorption on the sample surface as well as the difference at r_M = 10 µm. Near the center, the development proceeds quickly because the dose rate = 1. However, the dose rate rapidly decreases as the sample approaches the outer edge. Therefore, lateral development near the center more increased. The approximate dimensions of the PMMA pattern were 67.0 µm at the bottom end diameter, 22.0 µm at the inside hole diameter, and the height was 15.6 µm. The diameter of the hole here represents the value at the highest point.

4. Conclusion

In the conventional DXRL, resists pattern has been limitted by the pattern of the x-ray mask. Therefore, in this study, we tried to fabricate 3D microstructures by moving the resist while irradiating X-rays patterned by the X-ray mask. Using the developed multi-step exposure system at the NewSUBARU BL11 in the University of Hyogo, exposure experiments were conducted. PMMA was used as the resist material. As results, we could fabricate microstructures that have sizes very close to the calculated models. The minimum size of the processed shape was 2 µm, and we succeeded in processing a microstructure as designed. However, in some areas where there were differences in the exposure intensity distribution, the different shapes were observed. We consider this cause as follows: the development speed depends on the amount of energy absorption, and development proceeds not only from the surface of the exposed sample but also from the lateral direction. Then, we will improve the design model taking account into the development speed. And we will develop new devices using this multi-step exposure system.

5. References

[1] M. Takeuchi, A. Yamaguchi, and Y. Utsumi: J. *Synchrotron Rad*. **26**(2019)528.

[2] Chao-Min Cheng, and Ren-Haw Chen: *J.Micromech. Microeng*. **11**(2001)692.

[3] T. Chuang, T Fang, M Jiang, W Lei, B Shew,

COPY

and C Fu, *J.Micromech. Microeng.* **22** (2012) 085027.

[4] K. wang-Cheol Lee, and Seung S Lee, *Sensors and Actuators* A **108**(2003)121.

[5] O. tabata, H. You, N. Matsuzuka, T. Yamaji, S. Uemura, and I. Dama: *Microsystem technologies* **8** (2002) 93.

[6] A ANDO, T HATTORI, K HOSONO, K KANDA, H KINOSHITA, S MATSUI, H MEKARU, M NIIBE, Y UTSUMI and T WATANABE: *The Japanese Society for Synchrotron Radiation Research* **15** (2002) 8.

COPY

Journal of Photopolymer Science and Technology
Volume 36, Number 2 (2023) 97 − 100 ©2023SPST

Study of Dihedral-Corner-Reflector-Array Fabrication Process Using Soft X-ray Deep X-ray Lithography

Taki Watanabe[1*], Sho Amano[1], Shinya Izawa[1], Satoshi Maekawa[2], Keisuke Yoshiki[3], Akinobu Yamaguchi[1], and Yuichi Utsumi[1]

[1] Laboratory of Advanced Science and Technology for Industry, University of Hyogo, 3-1-2 Kouto, Kamigori, Hyogo 678-1205, Japan
[2] Parity Innovations Co. Ltd.
[3] Institute for Research Promotion and Collaboration
**wtaki@lasti.u-hyogo.ac.jp*

We fabricated sectoral-pillar structures for Dihedral Corner Reflector Array (DCRA) using Deep X-ray Lithography (DXRL) in New SUBARU Synchrotron Radiation Facility. We studied process conditions such as a start timing of development after exposure and development temperature. We succeeded in fabricating a structure without of micro-cracks on sidewalls of the pillar and in demonstration of floating image using the fabricated DCRA.
Keywords: Synchrotron radiation, X-ray, LIGA, Microfabrication, DCRA

COPY

1. Introduction

In recent years with the COVID-19, demand for non-contact terminal operation to avoid contact infection, has increased. To realize non-contact operation, a visible floating image and a sensor-based operation system are required. A Dihedral Corner Reflector Array (DCRA), which consists of two right-angle plane mirrors to generate floating image in the air, was proposed [1-4].

Fig. 1(a) shows the principle of DCRA. In a DCR the total reflections of a light-ray occur by two mirrors. Fig. 1(b) shows a path of light in XY plane of the DCR. When the angle of incidence is θ, the light from a source is reflected and returns to the source with an angle of 180° according to Equation (1) [3]. In three dimensions, the light from the source does not return to the source but reaches a symmetry point for the DCRA device face. This point is an observation point (Fig. 1(a)).

$$2\theta + 2\left(\frac{\pi}{2} - \theta\right) = \pi \tag{1}$$

By mounting many DCRs perpendicularly to a substrate, the real image can be formed at the observation point. The image sharpness is determined by surface clearness and right-angle accuracy of the DCR walls. However, it is not easy to produce such a microstructure with high

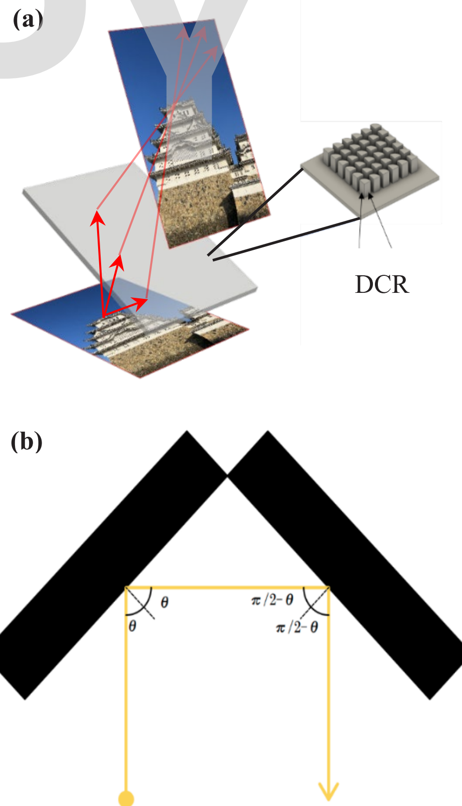

Fig. 1. (a) Principle of DCRA, (b) Trajectory of the ray.

Received March 14, 2023
Accepted May 16, 2023

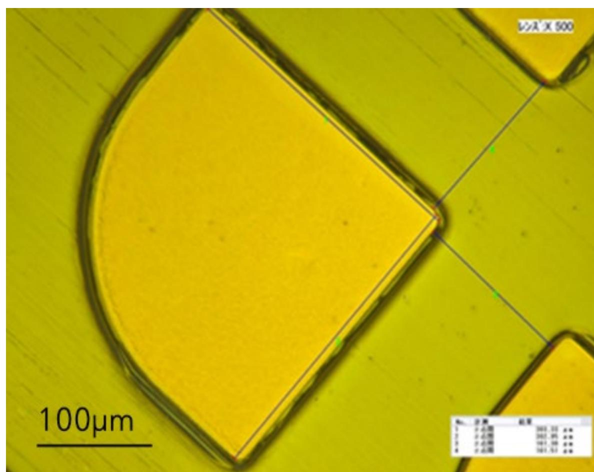

Fig. 2. Unique sectoral shaped x-ray mask.

precision by conventional machining. Therefore, we propose the use of DXRL technology for DCRA production. DXRL has several advantages: it is easy to fabricate microstructures with high aspect ratio, mirror surfaces can be machined with high precision, and it is a mass-production technology that can reduce costs [5-15]. Furthermore, by changing the pattern of the X-ray mask, desired cross-sectional shapes can be easily created. DCR shapes created previously were limited to square pillars or holes [1, 3]. In such shapes, the other two faces that do not contribute to required imaging may produce ghost. Therefore, in this study, we developed prototype pillar structures with a sectoral cross section as shown in Fig. 2 by DXRL, in which all surfaces except the two corner reflectors are curved. Shown in Fig. 2 is an X-ray mask used in DXRL.

2. Experimental

Exposure experiments were carried out in the NewSUBARU synchrotron radiation facility in the University of Hyogo. There are two modes of electron storage energy, 1.0 GeV and 1.5 GeV, but in this study, we used the 1.5 GeV mode, which has

Table 1. Target values and Measurements of each dimension of the DCR (parameters are defined in Fig. 6).

		target value	measurements
X wall	Upper distance [μm]	300	301.6
	Lower distance [μm]	300	303.5
	Upper side length [μm]	175	174.7
	Lower side length [μm]	175	171
	Verticality [mrad]	0	1.72
Y wall	Upper distance [μm]	300	291.9
	Lower distance [μm]	300	306.4
	Upper side length [μm]	175	186
	Lower side length [μm]	175	171.5
	Verticality [mrad]	0	13.1
	Average height [μm]	600	553

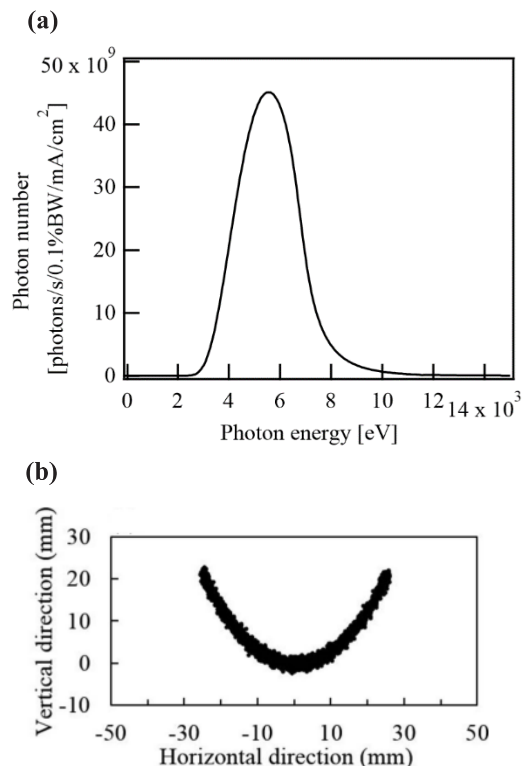

Fig. 3. (a) Photon intensity distribution as a function of photon energy at the beamline BL11, (b)beam shape (cite from [7]).

higher X-ray energy and allows deeper processing. In BL11, synchrotron radiation X-rays are passedthrough a toroidal mirror and two Be filters to cut off energy components below 2 KeV. The spectrum at the exposure plane is shown in Fig. 3(a). The X- ray energy range is 3KeV-8KeV, with a peak of approximately 6KeV. The beam pattern is shown in Fig. 3(b) and the beam is highly paralleled with a divergence of 278 μrad in the horizontal direction and 14 μrad in the vertical direction [7].

In this study, PMMA (CLAREX Precision Sheet, Nitto Jushi Kogyo Co., Ltd) pillar structures are tested. The critical angle of PMMA was calculated to be 42.2° from Snell's law, and the aspect ratio should be 2 to realize a two-times reflections in DCR. The smaller DCR size causes the higher space-resolution, but the image becomes darker because of diffraction, so there is an optimum size. There is an optimum DCR pitch for a focal distance. Based on the above, we determined the dimensions of the device to be fabricated in this study as shown in Table 1.

We used GG developer solution for the development and developed the PMMA samples for 24 hours. The ingredients of the developer are shown in Table 2. The development temperature and the elapsed time to start development were changed

COPY

Table 2. Ingredients of the GG developer.

Ingredient	Vol%
2-(2-n-butoxy-ethoxy)ethanol	60
Tetrahydro-1, 4-oxazine	20
2-amino-ethanol-1	5
D. I. Water	15

and their optimum conditions were researched.

3. Results and discussion

We succeeded in fabricating a DCRA without micro-cracks on the pillar wall surface in the optimized development condition. The unique sectoral shaped DCRA fabricated is shown in Fig. 4. The exposure dose was 150 J/cm2. The developing conditions at this time were a developing solution temperature of 37.8°C and an elapsed time to start development of 15 minutes.

Using this DCRA, we observed a floating image as shown in Fig. 5. The DCRA size was 2 cm square.

The scale parameters of each part of DCRA is defined as shown in Fig. 6. The target dimensions and measured values of the fabricated DCRA are summarized in Table 1. Although the floating image was successfully formed using the fabricated new DCRA, there is still a problem to be solved to obtain clearer image. It is the verticality of the DCR pillar is poor. In Table 1, the verticality is clearly worse on the Y wall than on the X wall. We consider this cause is due to thermal inhomogeneous by X-ray beam scanning. Since the X wall is perpendicular to the beam scan direction, similar thermal mass is given simultaneously, but since the Y wall is parallel, a continuous distribution of thermal mass is created.

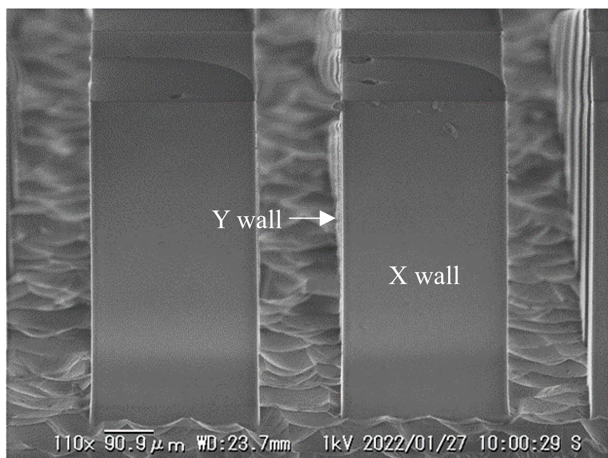

Fig. 4. The unique sectoral shaped DCRA fabricated.

4. Conclusion

In this study, we fabricated a new DCRA device that can generate a floating image in the air. In conventional square DCRA, two surfaces that do not contribute to image formation may cause the generation of ghost images. Therefore, we fabricated a unique sectoral-pillar DCRA that is expected to generate less ghost. For this micro-fabrication, we studied the PMMA fabrication process by DXRL at aBL11 in NewSUBARU. By trying various development conditions, we found the condition under which micro-cracks on the pillar wall were not observed. Using the DCRA fabricated, floating imaging was observed. However, the verticality of the pillar still needs improvement. We will improve the exposure and development process in order to establish a DCRA processing by DXRL.

Fig. 5. Floating image formed using the fabricated DCRA.

COPY

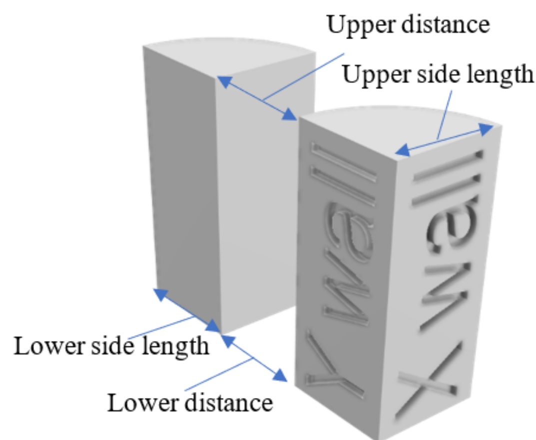

Fig. 6. Scale parameters of each part of DCRA.

References

1. A. Yamaguchi, S. Maekawa, T. Yamane, I. Okada, and Y. Utsumi, *Transactions of The Japan Institute of Electronics Packaging* **8** (2015) 23.
2. D. Miyazaki, N. Hirano, Y. Maeda, S. Yamamoto, T. Mukai, and S. Maekawa, *Applied Optics,* **52** (2013) A282.
3. J. G. Korvink, S. Haf, S. Maekawa, *NanotechJapan Bulletin* **7** (2014) No.4.
4. S. Maekawa, Y. Hirai, and O. Matoba, Proc. SPIE 6392, 63920E (2006).
5. Meyer, *LIGA and its Applications,* (2009).
6. Y. Utsumi, T. Kishimoto, T. Hattori, and H. Hara, *Jpn. J. Appl. Phys*. **44** (2005) 550.
7. M. Takeuchi, A. Yamaguchi, and Y. Utsumi, *J. Synchrotron Rad*., **26** (2019) 528.
8. W. Ehrfeld, V. Hessel, H. Lowe, Ch. Schulz, and L. Weber, *Microsystem technologies.,* **5** (1999) 105.
9. F. Perennes, B. Marmiroli, M. Matteucci, M. Tormen, L. Vaccari, and E. Di. Fabrizio, *J. Micromech. Microeng.,* **16** (2006) 473
10. F. Karlsruhe, *Sensors and materials*, **10** (1998) 363.
11. V. Saile, U. Wallrabe, O. tabata, J. G. Korvink, “LIGA and Its Applications”, Wiley-VCH Verlag GmbH & Co. KGaA, (2008) 51.
12. S. Lemke, P. Goettert, I. Rudolph, J. Goettert, and B. Lochel, *Proceedings MNE Conference,* (2013).
13. G. Feiertag, W. Ehrfeld, H. Freimuth, H. Kolle, H. Lehr, M. Schmidt, M. M. Sigalas, C. M. Soukouli, G. Kiriakidis, T. Pedersen, J. Kuhl, and W. Koenig, *Appl. Phys. Lett.*, **70** (1997) 1441.
14. B. Lai, D. C. Mancini, W. Yun, and E. Gluskin, *Microlithography and Metrology in Micromachining 2*, (1996).
15. H. Scheunemann, B. Loechela, L. Jiana, D. Schondelmaier, Y. M. Desta, and J. Goettert, *Smart Sensors, Actuators, and MEMS*, (2003).

COPY

Journal of Photopolymer Science and Technology
Volume 36, Number 2 (2023) 101－110 ©2023SPST

Development of Photo-curable Resin for 3D Printing Using Acrylic Monomers with Bisphenol Skeleton

Kotaro Kobayashi[1], Daisuke Aoki[1], Tatsuo Taniguchi[1,2], Takashi Karatsu[1,2 *], Nobuaki Takane[3], Hiroaki Okamoto[3], Koichi Fujii[4], and Yuki Yamauchi[4]

[1] Department of Applied Chemistry and Biotechnology, Graduate School of Engineering, Chiba University, 1-33 Yayoi-cho, Inage-ku, Chiba-shi, Chiba 263-8522, Japan
[2] Molecular Chirality Research Center, Chiba University, 1-33 Yayoi-cho, Inage-ku, Chiba-shi, Chiba 263-8522, Japan
[3] Okamoto Chemical Industry Co., Ltd., 2-6-4 Chuo, Warabi-shi, Saitama 335-0004, Japan
[4] Tokyo Metropolitan Industrial Technology Research Institute, 2-4-10, Aomi, koto-ku, Tokyo 135-0064, Japan
** karatsu@faculty.chiba-u.jp*

Vat photopolymerization 3D printing mainly uses acrylic or epoxy monomers, or a mixture of these monomers. Polymerization of hard and brittle acrylic monomers and flexible epoxy monomers forms an interpenetrating polymer network, resulting in a resin with fast curing speed and high toughness. However, phase separation occurs, and stress concentrated between the layers causes the cured resin to fracture. In this study, we synthesized acrylic monomers that have both rigid and flexible parts in a single molecule. By using this monomer in a photo-curable resin, we have developed resins that suppress phase separation and have excellent curing speed and toughness.

Keywords: 3D printing, Stereolithography, Acrylic monomer, Epoxy monomer, Interpenetrating polymer network, Bisphenol, Tensile strength

COPY

1. Introduction

3D printers (Additive Manufacturing, AM) create 3D objects based on 3D-CAD data, and in recent years they have been used in various fields such as medicine and architecture. Vat photopolymerization (SLA or DLP) is one modeling methods of 3D printing. This method uses photo-curable resin, which hardens when exposed to light, to create a three-dimensional object. Compared to other molding methods, the vat photopolymerization method has the advantage of quick and smooth molding, but it also has the disadvantage of low strength [1-6]. Because of this disadvantage, it is difficult to create final products using the vat photopolymerization method, and the method is mainly use to create prototypes and manufacture products that do not require high strength. It is expected that industrial products such as automobile parts and gears can be manufactured using the vat photopolymerization method, which can create complex shapes with high precision if the strength of the resin can be improved.

Photo-curable resins used in the vat photopolymerization are generally radical or cationic polymerization systems. Acrylic monomers are mainly used for radical polymerization, and while they generally react quickly, the resulting polymers are characterized by being hard and brittle [7,8]. Cationic polymerization mainly uses epoxy monomers, which generally have slower reaction rate and cure slowly, but the resulting polymers are flexible and toughness [9,10]. In the Vat photopolymerization, these two types of monomers are sometimes mixed to form a structure called an interpenetrating polymer network (IPN), which is a state in which polymer chains are intertwined. The IPN formation of hard and brittle acrylic monomers and flexible epoxy monomers has been shown to produce resin with high curing speed and excellent mechanical strength [11-15]. However, strength is not sufficient to form the final product using the Vat photopolymerization, and a material with high toughness that combines hardness and tenacity is

Received April 24, 2023
Accepted May 19, 2023

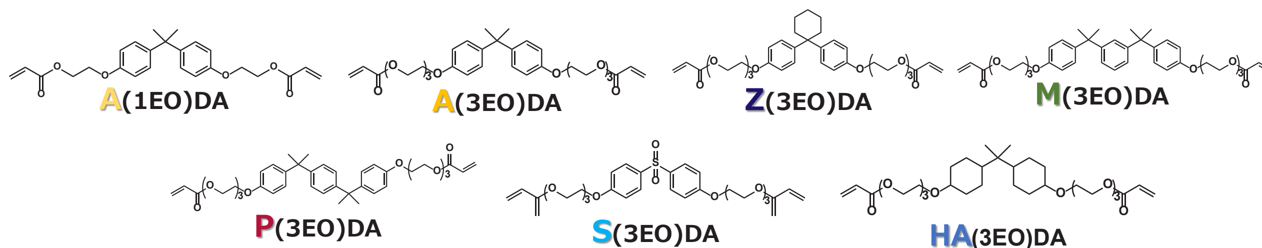

Fig. 1. Structures of synthesized monomers and their abbreviation names.

required.

In this study, we developed a photo-curable resin with high toughness with the aim of fabricating final products using the vat polymerization method. As an approach, we developed photo-curable resins using acrylic monomers that have both rigid and flexible parts in a monomer molecule. In conventional acrylic-epoxy blends, a hard, brittle component and a flexible component are mixed, and each is polymerized. In this case, since the monomers are polymerized from the same type of monomer, phase separation occurs, and stress concentration between the phases causes the resin to fracture [16]. By using the monomers in this research, the rigid and flexible parts are connected alternately, preventing the concentration of stress between the phases and improving strength. We synthesized bifunctional acrylic monomers, focusing on a bisphenol skeleton, which is widely used in industry and inexpensive, for the rigid part and an ethylene oxide chain for the flexible part (Fig. 1). The synthesized monomers were evaluated for mechanical strength and thermal properties as photo-curable resins.

2. Experimental

2.1. Apparatus

Following apparatuses were used in this research, ^{1}H NMR; Bruker AVANCE-III-400M (400 MHz). Light source; CCS, LDR2-60VL405-W-TP equipped with PD3-3024-3-EI(A) (405 nm) and ELEGOO, Mercury curing machine DLP SLA3D (405 nm). Hot plate; AS ONE, Ceramic hot plate CHP-170DN. FT-IR; JASCO, FT/IR-4100. DSC; SHIMADZU, DSC-60 plus equipped with FC-60A, and TGA; SHIMADZU, DTG-60A equipped with FC-60A.

2.2. Reagents

2,2-Bis(4-hydroxyphenyl)propane (Bisphenol A), 1,1-bis(4-hydroxyphenyl)cyclohexane (Bisphenol Z) , 1,3-bis[2-(4-hydroxyphenyl)-2-propyl]benzene (Bisphenol M), α,α'-bis(4-hydroxyphenyl)-1,4-diisopropylbenzene (Bisphenol P), bis(4-hydroxyphenyl)sulfone (Bisphenol S), 2-[2-(2-chloroethoxy)ethoxy]ethanol (CEEE), ethylene carbonate (EC), acryloyl chloride (AC), phenylbis(2,4,6-trimethylbenzoyl)phosphine oxide (BAPO) were purchased from Tokyo Chemical Industry Co., and used as it received. 2,2-Bis(4-hydroxycyclohexyl)propane (hydrogenated Bisphenol A), potassium carbonate, potassium iodide, and triethylamine were purchased from FUJIFILM Wako Pure Chemicals Co. and used as they received.

2.3. Syntheses

For the preparation of monomers, A(1EO)DA was prepared by stepwise reaction of EC and AC. The other monomers were prepared by stepwise reaction of the corresponding bisphenols with CEEE and AC (Table 1).

2.3.1. A(1EO)H [17]

9.80 g of Bisphenol A (43.8 mmol), 8.05 g of EC (91.4 mmol) and 11.16 g of potassium carbonate (80.8 mmol) were placed in a three-necked round flask. 100 mL of DMF was then added and the flask was purged with nitrogen, and then held at 150°C for 12 hs while stirring. The reaction mixture was extracted with Ethyl acetate and washed with brine

COPY

Table 1. Materials stoichiometry and yield of the monomer syntheses.

Reactant of the first step reaction [a)]		Product (Yield / %)	Reactant of the second step reaction [b)]	Final product (Yield / %)
				HA(3EO)DA 1.95 g (12.0%)

COPY

and water, followed by drying with anhydrous sodium sulfate to give a white solid (10.42 g, 75.0% yield).

+ 2

K_2CO_3

DMF

A(1EO)H: ^{1}H NMR ($CDCl_3$, 400 MHz), δ ppm: 1.62 (s, 6H), 3.95-3.92 (t, J = 5.27 Hz, 4H), 4.07-4.04 (t, J = 4.08 Hz, 4H), 4.12-4.10 (t, J = 4.71 Hz, 4H), 6.83-6.79 (d, J= 8.97 Hz, 4H), 7.15-7.12 (d, J= 9.03 Hz, 4H).

2.3.2. A(1EO)DA [18]

5.03 g of A(1EO)H (15.8 mmol), 3.24 g of triethylamine (32.0 mmol), and 90 mL of THF as a solvent were placed in three-necked round flask. The flask was purged with nitrogen and held at 0°C. 3.93 g of acryloyl chloride (43.4 mmol) was added to this solution over 30 mins and then stirred for 24 hs. After filtration of the reaction mixture, the product was isolated by silica gel column chromatography (AcOEt: hexane: chloroform = 2:1: 1) to give a white solid (1.54 g, 26.5% yield).

+ 2

Triethylamine

THF

A(1EO)DA: ^{1}H NMR ($CDCl_3$, 400 MHz): δ ppm: 1.63 (s, 6H), 4.20-4.17 (t, J = 4.77 Hz , 4H), 4.50-4.48 (t, J= 4.77 Hz , 4H), 5.86-5.83 (dd, J_1 = 10.48 Hz, J_2 = 1.44 Hz, 2H), 6.19-6.12 (dd, J_1 = 17.57 Hz, J_2 = 10.42 Hz, 2H), 6.44-6.41 (dd, J_1 = 17.38 Hz, J_2 = 1.44 Hz, 2H), 6.83-6.80 (d, J= 8.91 Hz, 4H), 7.14-7.12 (d, J= 8.97 Hz, 4H).

2.3.3. A(3EO)H [19]

In a typical run, 41.86 g of Bisphenol A (183.6

mmol), 49.26 g of potassium carbonate (356.9 mmol) and 8.71 g of potassium iodide (52.4 mmol) were placed in a three-necked round flask. 150 mL of DMF was then added and the flask was purged with nitrogen, and then held at 80°C for 30 mins while stirring. 79.38 g of CEEE (472.5 mmol) was added to the reaction mixture and stirred at 80°C for 24 hs. The reaction mixture was extracted with ethyl acetate and washed with brine and water, followed by drying with anhydrous sodium sulfate. The product was isolated by silica gel column chromatography (AcOEt: hexane: chloroform = 2:1:1) to give a yellowish liquid (40.67 g, 47.3% yield).

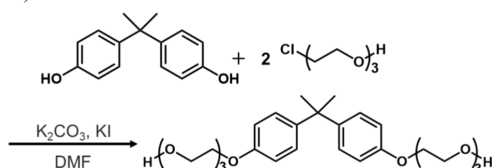

A(3EO)H: ^{1}H NMR ($CDCl_3$, 400 MHz), δ ppm: 1.62 (s, 6H), 3.74-3.68 (m, 12H), 3.86-3.83 (t, J = 4.83 Hz, 4H), 4.12-4.10 (t, J= 4.71 Hz, 4H), 6.80-6.76 (d, J= 8.91 Hz, 4H), 7.14-7.12 (d, J= 8.85 Hz, 4H).

2.3.4. A(3EO)DA [20]

In a typical run, 40.67 g of A(3EO)H (82.8 mmol) and 20.85 g of triethylamine (206.4 mmol) were placed in a three-necked round flask. 100 mL of chloroform was then added and the flask was purged with nitrogen, and then held at 0°C. 22.48 g of acryloyl chloride (248.0 mmol) was added to this solution over 30 mins and then stirred for 24 hs. The reaction mixture was extracted with chloroform and washed with brine and water, followed by drying with anhydrous sodium sulfate. The product was isolated by silica gel column chromatography (AcOEt: hexane: chloroform = 2: 1: 1) to give a yellowish liquid (28.99 g, 58.3% yield).

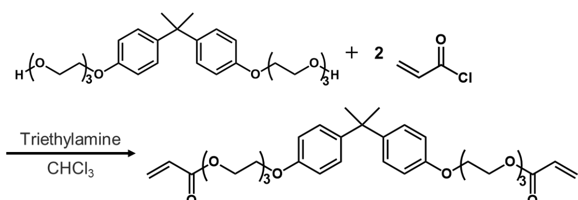

A(3EO)DA: ^{1}H NMR ($CDCl_3$, 400 MHz), δ ppm: 1.62 (s, 6H), 3.76-3.67 (m, 12H), 3.85-3.82 (t, J = 4.96 Hz , 4H), 4.11-4.08 (t, J= 5.02 Hz, 4H), 4.32-4.30 (t, J= 4.87 Hz, 4H), 5.83-5.80 (dd, J_1 = 10.48 Hz, J_2 = 1.44 Hz, 2H), 6.18-6.11 (dd, J_1 = 17.38 Hz, J_2 = 10.35 Hz, 2H), 6.44-6.40 (dd, J_1 = 17.32 Hz, J_2 = 1.44 Hz, 2H), 6.80-6.78 (d, J = 8.85 Hz, 4H), 7.15-7.12 (d, J = 8.91 Hz, 4H).

2.3.5. ^{1}H NMR data for other monomer precursors and monomers

Z(3EO)H**:** ^{1}H NMR ($CDCl_3$, 400 MHz), δ ppm: 1.58-1.44 (m, 6H), 2.22-2.18 (t, J = 5.65 Hz, 4H), 3.61-3.58 (t, J = 4.71 Hz, 4H), 3.72-3.64 (m, 12H), 3.84-3.81 (t, J = 4.83 Hz, 4H), 4.11-4.07 (t, J = 4.71 Hz, 4H), 6.82-6.79 (d, J= 8.91 Hz, 4H), 7.15-7.13 (d, J= 8.91 Hz, 4H).

Z(3EO)DA**:** ^{1}H NMR ($CDCl_3$, 400 MHz), δ ppm: 1.53-1.40 (m, 6H), 2.22-2.18 (t, J = 5.84 Hz, 4H), 3.75-3.66 (m, 12H), 3.84-3.81 (t, J = 5.02 HZ, 4H), 4.09-4.07 (t, J = 4.89 Hz, 4H), 4.32-4.29 (t, J = 4.77 Hz, 4H), 5.83-5.80 (dd, J_1 = 10.42 Hz, J_2 = 1.51 Hz, 2H), 6.18-6.11 (dd, J_1 = 17.94 Hz, J_2 = 10.48 Hz, 2H), 6.44-6.40 (dd, J_1 = 17.44 Hz, J_2 = 1.51 Hz, 2H), 6.81-6.78 (d, J = 8.97 Hz, 4H), 7.15-7.13 (d, J = 8.91 Hz, 4H).

M(3EO)H**:** ^{1}H NMR ($CDCl_3$, 400 MHz), δppm: 1.60 (s, 12H), 3.75-3.68 (m, 16H), 3.86-3.84 (t, J = 4.71 Hz, 4H), 4.12-4.10 (t, J = 4.77 Hz, 4H), 6.80-6.76 (d, J = 8.97 Hz, 4H), 7.01-7.00 (d, J = 9.10 Hz, 2H), 7.15-7.00 (m, 6H).

M(3EO)DA**:** ^{1}H NMR ($CDCl_3$, 400 MHz), δ ppm: 1.60 (s, 12H), 3.77-3.67 (m, 12H), 3.86-3.83 (t, J= 4.96 Hz , 4H), 4.11-4.10 (t, J = 4.96 Hz, 4H), 4.33-4.30 (t, J = 4.71 Hz, 4H), 5.83-5.80 (dd, J_1 = 10.42 Hz, J_2 = 1.44 Hz, 2H), 6.18-6.11 (dd, J_1 = 17.94 Hz, J_2 = 10.48 Hz, 2H), 6.44-6.40 (dd, J_1 = 17.38 Hz, J_2 = 1.44 Hz, 2H), 6.80-6.78 (d, J = 8.91 Hz, 4H), 6.99-6.97 (d, J = 9.10 Hz, 2H), 7.14-7.06 (m, 6H).

P(3EO)H**:** ^{1}H NMR ($CDCl_3$, 400 MHz), δppm: 1.62 (s, 12H), 3.65-3.60 (t, J= 4.71 Hz, 4H), 3.74-3.68 (m, 12H), 3.86-3.83 (t, J = 4.83 Hz, 4H), 4.12-4.10 (t, J = 4.71 Hz, 4H), 6.80-6.76 (d, J = 8.91 Hz, 4H), 7.08 (s, 4H), 7.14-7.12 (d, J= 8.85 Hz, 4H).

P(3EO)DA**:** ^{1}H NMR ($CDCl_3$, 400 MHz), δ ppm: 1.62 (s, 12H), 3.76-3.67 (m, 12H), 3.85-3.82 (t, J= 4.96 Hz , 4H), 4.11-4.08 (t, J = 5.02 Hz, 4H), 4.32-4.30 (t, J = 4.87 Hz, 4H), 5.83-5.80 (dd, J_1= 10.48 Hz, J_2= 1.44 Hz, 2H), 6.18-6.11 (dd, J_1 = 17.38 Hz, J_2 = 10.35 Hz, 2H), 6.44-6.40 (dd, J_1 = 17.32 Hz, J_2 =1.44 Hz, 2H), 6.80-6.78 (d, J = 8.85 Hz, 4H), 7.08 (s, 4H), 7.15-7.12 (d, J=8.91, 4H).

S(3EO)H**:** ^{1}H NMR ($CDCl_3$, 400 MHz), δppm: 3.72-3.58 (m, 16H), 3.87-3.84 (t, J = 4.77 Hz, 4H), 4.17-4.14

COPY

(t, J = 4.64 Hz, 4H), 4.12-4.10 (t, J = 4.71 Hz, 4H), 6.98-6.95 (d, J = 9.03 Hz, 4H), 7.84-7.81 (d, J = 8.97 Hz, 4H).

S(3EO)DA**:** ^{1}H NMR ($CDCl_3$, 400 MHz), δ ppm: 3.75-3.66 (m, 12H), 3.86-3.84 (t, J = 4.83 Hz , 4H), 4.16-4.13 (t, J = 4.77 Hz, 4H), 4.32-4.29 (t, J = 4.83 Hz, 4H), 5.83-5.80 (dd, J_1 = 10.42 Hz, J_2 = 1.51 Hz, 2H), 6.17-6.10 (dd, J_1 = 17.94 Hz, J_2 = 10.48 Hz, 2H), 6.44-6.40 (dd, J_1 = 17.44 Hz, J_2 =1.51 Hz, 2H), 6.97-6.94 (d, J = 8.97 Hz, 4H), 7.83-7.81 (d, J =9.03, 4H).

HA(3EO)H**:** ^{1}H NMR ($CDCl_3$, 400 MHz), δ ppm: 0.75-0.72 (m, 6H), 2.09-1.03 (m, 18H), 3.77-3.26 (m, 20H), 4.49-4.27 (m, 4H).

HA(3EO)DA**:** ^{1}H NMR ($CDCl_3$, 400 MHz), δ ppm: 0.75-0.73 (m, 6H), 2.08-1.09 (m, 18H), 3.77-3.62 (m, 16H), 4.71-4.29 (m, 8H), 5.85-5.78 (dd, J_1 = 10.40 Hz, J_2 = 1.53 Hz, 2H), 6.23-6.06 (dd, J_1 = 17.95 Hz, J_2 = 10.51 Hz, 2H), 6.60-6.40 (dd, J_1 = 17.44 Hz, J_2 = 1.51 Hz, 2H).

HA(3EO)H and HA(3EO)DA were not strictly assigned peaks due to the mixture of stereoisomers of cyclohexane. The introduction of ethylene oxide chains and acrylic parts was confirmed.

COPY

2.4. Evaluation of resins

Resins were evaluated for tensile testing, impact resistance, monomer conversion, and thermal properties. Photo-curable resins for 3D printers require the use of liquid monomers. Therefore, among the acrylic monomers synthesized, A(3EO)DA, Z(3EO)DA, M(3EO)DA, P(3EO)DA and HA(3EO)DA, which were obtained in liquid state, were used as photo-curable resins. In the strength test, HA(3EO)DA was tested only tensile testing.

2.4.1 Tensile testing

Dumbbell-shaped samples were used for tensile testing. To prepare a dumbbell-shaped sample, the synthesized monomer and initiator are first mixed at room temperature under light-shielded conditions. BAPO was used as the initiator. The light irradiation method is divided into initial curing and post curing, following the actual 3D printer modeling process. First, 700 μL of the resin was placed in a dumbbell-shaped silicon mold for initial curing and irradiated with 405 nm light for 3 mins using CCS 405 nm LED lamp. After that, the cured resin is removed from the silicon mold and irradiated with 405 nm light for 30 mins as post curing using ELEGOO Mercury LED lamp. Since heating is also commonly used for post curing, in this study, samples were prepared with only photocured and samples with photocured followed by heating [21]. Heating was performed on a hot plate at temperatures of 100, 150, and 200°C for 1 h. The samples after curing are shown in Fig. 2. The sample thickness is 0.1 cm and Tensile speed was 10 mm/min.

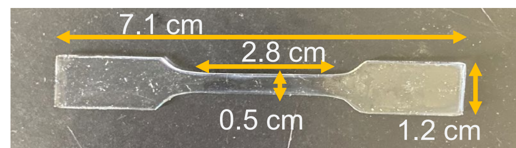

Fig. 2. Shape and size of a dumbbell-shaped sample.

2.4.2 Impact resistance test

In the impact resistance test, a metal weight was continuously dropped onto the cured resin, and the impact resistance was evaluated from the height at which the cured resin cracked. The test was started at 20 cm and increased by 5 cm if the cured resin did not crack. Rectangular samples were used for the impact resistance test. Samples were prepared by stacking layers according to actual 3D printer modeling. A square silicon mold was filled with 130 mL of liquid resin and irradiated with light using CCS 405 nm LED lump. Then, 130 mL of liquid resin was placed again on top of the cured layer and cured by light irradiation for 1 min. This process was repeated three times to produce a cured resin with three layers. After that, the cured resin is removed from the silicon mold and irradiated with 405 nm light for 30 mins as post-curing using ELEGOO Mercury lump. As in the tensile test, two types of post curing were performed: only photocured and photocured and then heated. The cured resins were heated to 150 and 200°C. The samples after curing are shown in Fig. 3. The sample thickness is 0.2 cm.

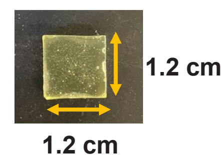

Fig. 3. Shape and size of a prepared rectangular sample.

2.4.3 Monomer conversion rate measurement

The conversion ratio in resins made with each monomer was measured using FT-IR. The 1 mL mixture of monomer and initiator was dropped onto a KBr window plate, sandwiched between two other KBr window plates, and illuminated with 405 nm light for a certain time before FT-IR measurement. The conversion of the C=C bond (1635 cm^{-1}) of the acrylic group due to the progress of the polymerization reaction was calculated, and the change in conversion was traced by plotting the change over time.

2.4.4 Thermal property investigation

The photocured resin was ground and thermogravimetric analysis (TGA) and Differential Scanning Calorimetry (DSC) measurements were performed. TGA measurements were performed under a pseudo-air atmosphere, in a temperature range of 100 ~ 600°C, and at a temperature increase rate of 5°C/min. From TGA measurement, the temperature at which 5% ($T_{5\%}$) and 10% ($T_{10\%}$) weight loss of each sample was investigated. DSC measurements were performed under a high purity nitrogen atmosphere, in a temperature range of 30 ~ 220°C, and at a temperature increase rate of 5°C/min. Glass transition temperature (T_g) and crystallization temperature were measured from DSC.

3. Results and discussion

3.1. Tensile testing

Figure 4 shows the stress-strain curves of tensile testing of cured resins made with the synthesized monomers. The stress-strain curves for resins only photocured and heated at 100°C showed a flat curve shape, indicating that the cured resins are highly flexible. However, the curve shape changed significantly for the resins heated at 150°C and 200°C. Heating above 150°C revealed a yield point, making the resin harder, more tenacious, and tougher.

COPY

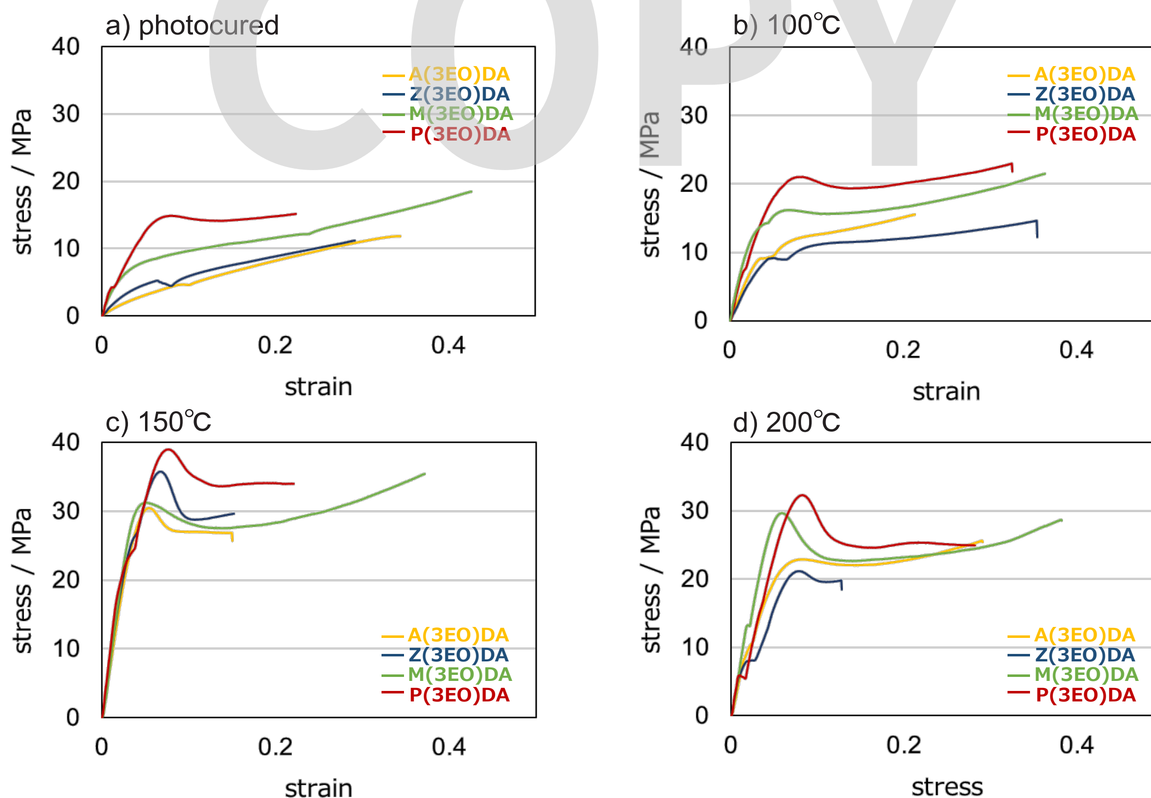

Fig. 4. Stress-strain curve of each cured resins. (a) Samples just after photo-cured, (b)-(d) samples post-baked at 100, 150, and 200°C, respectively.

For all cured resins, the highest tensile strength was achieved when heated to 150°C. Tensile strength was 2-3 times higher than that of only photocured. The highest tensile strength was achieved with P(3EO)DA resin, which showed 39 MPa. In addition to high tensile strength, resins using M(3EO)DA and P(3EO)DA, which have three benzene rings in the monomer unit, have high elongation at break, indicating that they are tough resins. In addition, resins heated at 150°C and 200°C exhibited necking.

Tensile testing was conducted with a resin using HA(3EO)DA, a monomer in which the benzene ring of bisphenol A was hydrogenated, to compare it with A(3EO)DA (Fig. 5). The cured resin using A(3EO)DA with benzene ring showed high elongation at break and necking upon heating, whereas the cured resin using hydrogenated HA(3EO)DA showed low elongation at break and was hard and brittle, showing no necking upon heating. It is suggested that the introduction of benzene rings in the monomer structure facilitates the orientation of the polymer, resulting in a high elongation rate and necking upon heating.

3.2. Impact resistance

The results of the impact resistance test are shown in Fig. 6. The only photocured resin was more flexible, as shown by the tensile test, and the flexibility resulted in a higher impact strength. For resins after heating, cured resin using M(3EO)DA and P(3EO)DA, which contain three benzene rings in the monomer unit, also have excellent impact strength even after heating. Impact resistance test also shows that these resins have high toughness.

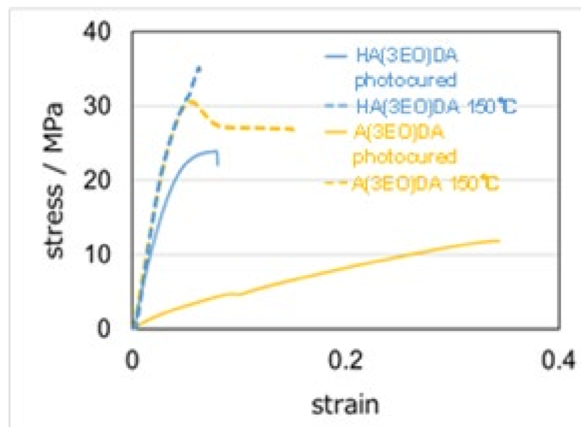

Fig. 5. Stress-strain curve of cured HA(3EO)DA resin.

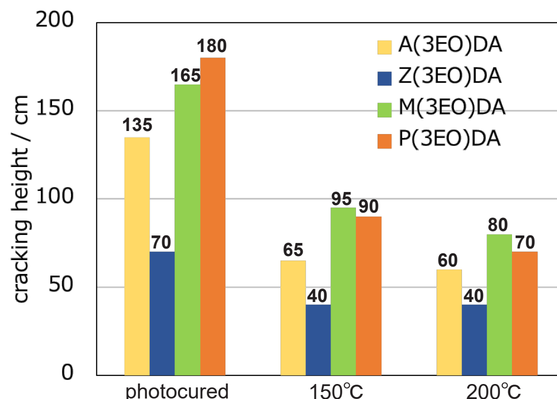

Fig. 6. Impact resistance of each resin.

3.3. Monomer conversion rate

Figure 7 and Table 2 show the conversion rate of each resin with respect to the light irradiation time. For all resins using any monomer, the conversion increased to as high as 70~80% after 30 seconds of light irradiation, and the conversion exceeded 80% after 3 mins of irradiation. The final conversion during light curing was in the high 80% range for all resins. The conversion after heating at 200°C was also measured. The conversion after heating increased only slightly for all resins. This suggests that the increase in tensile strength of the resins was not due to a decrease in unreacted monomers upon heating. The reason for the increase in strength is thought to be a change in polymer structure.

3.4. Thermal property investigation

Figure 8 shows the TGA and DSC measurements of cured resins using each monomer. The DSC scanning curves show only the results of the second run. Table 2 also shows the $T_{5\%}$, $T_{10\%}$, and T_g of cured resins using each monomer. In all samples, pyrolysis started around 240°C and ended around 500°C to 550°C. There was no significant difference in the $T_{5\%}$ and $T_{10\%}$ among the resins. The T_g ranged from 40 to 60°C, there was no significant difference among the resins. It was found that there was no significant difference in thermal properties when the type of the central bisphenol skeleton was changed.

From the DSC results, a slight peak that appeared to be crystallization was observed around 130°C for resins using any of the monomers. This indicates that the polymer partially crystallized when heated above

COPY

130°C for the resins in this study [22]. The significant increase in tensile strength of the sample heated at 150°C in the tensile testing is thought to be due to partial crystallization of the polymer [22,23].

The shape of the scanning curve between the first and second DSC runs was focused on to confirm the strain of the polymer; if the shape change between the first and second runs is large, the strain is large [24]. The shape change of the scanning curve of M(3EO)DA resin that was only photocured and the resin that was photocured and then heated at 150°C was checked (Fig. 9). The shape change of the only photocured resin was large, while the shape change of the heated resin was small and the polymer strain was reduced.

The above results indicate that the use of monomers with benzene rings in the resins in this study resulted in a high elongation rate and necking due to the orientation of the polymer upon heating, and that the partial crystallization of the polymer increased its tensile strength and made it a resin with high toughness.

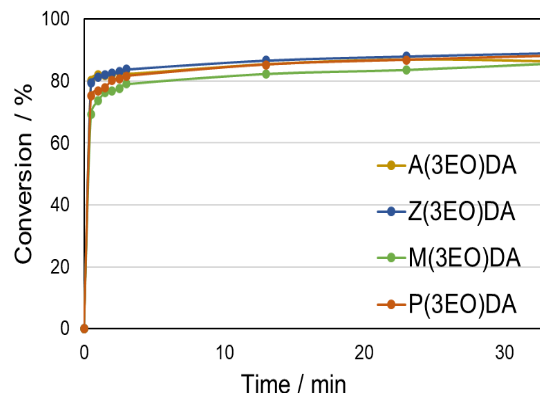

Fig. 7. Photocuring conversion curve of each resin.

COPY

Table. 2. Maximum conversion just after photocuring and post-heating. $T_{5\%}$, $T_{10\%}$, and T_g of each cured resin.

	A(3EO)DA	Z(3EO)DA	M(3EO)DA	P(3EO)DA
Photocured / %	86.3	85.6	85.6	88.0
200°C post-heated / %	88.0	87.2	87.2	89.8
$T_{5\%}$ / °C	282.7	286.5	281.2	286.5
$T_{10\%}$ / °C	299.0	301.7	297.8	300.8
T_g / °C	46.5	57.5	42.8	57.0

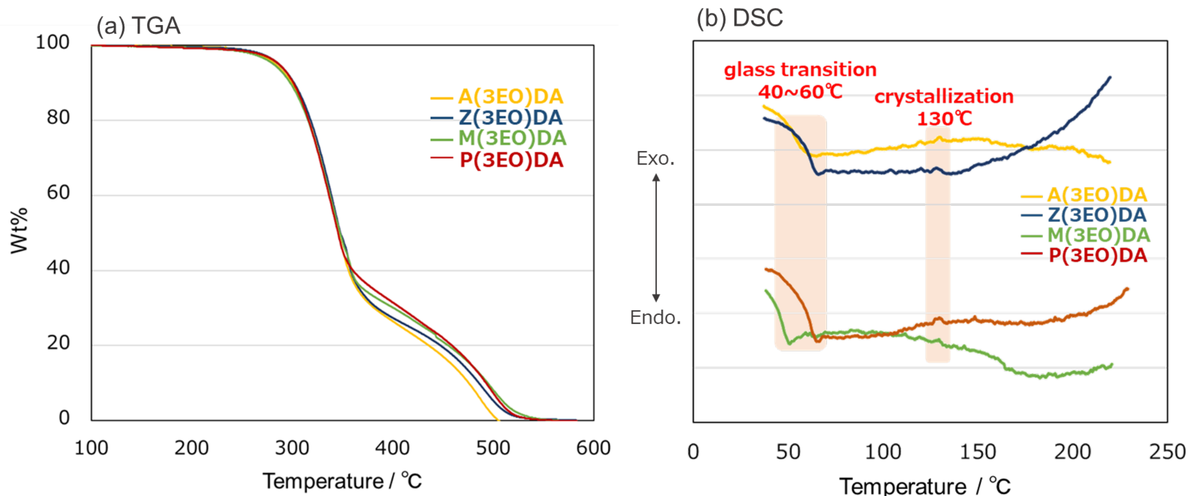

Fig. 8. Result of (a)TGA and (b)DSC of each resin.

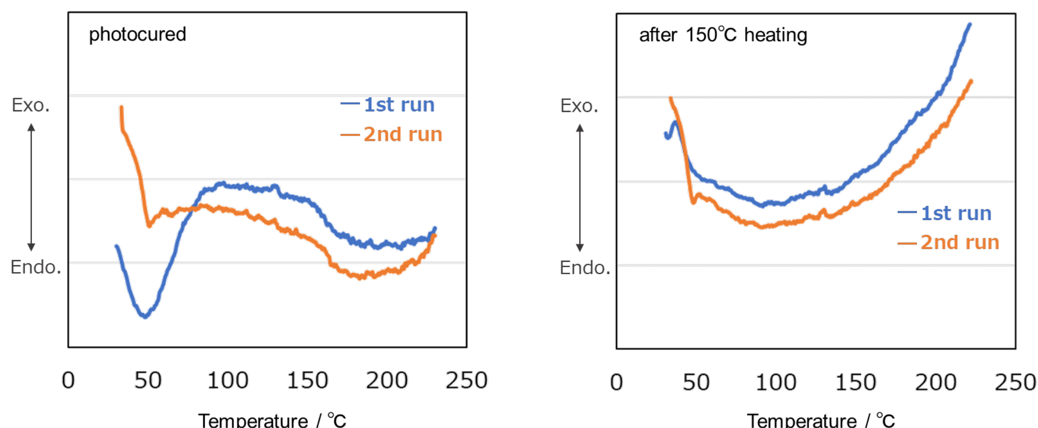

Fig. 9. Comparison of the results of the first and second DSC scans for the samples of with and without heating (150°C) after light curing of M(3EO)DA resins.

4. Conclusion

In this study, we synthesized acrylic monomers having both rigid and flexible parts in one molecule and developed a fast curing and high-strength photo-curable resin. As the rigid part, we focused on bisphenol, which is widely used in industry and available at low cost. As the flexible part, we focused on ethylene oxide chains and synthesized bifunctional acrylic monomers combining them. We succeeded in producing high-strength resins using these monomers. The introduction of benzene rings in the monomer structure facilitated polymer orientation, resulting in a high elongation rate. Furthermore, heating the polymer at 130°C or higher eliminated the polymer strain. Partial crystallization resulted in improved tensile strength and tensile modulus. These results may serve as a guideline for designing tough photo-curable resins.

Acknowledgements

This study was supported by METI Monozukuri R&D Support Grant Program for SMEs Grant Number JPJ005698. The authors also acknowledge the Centre for Analytical Instrumentation, Chiba University for their support of ^{1}H NMR spectroscopy.

References

1. M. Sangermano, *Pure Appl. Chem.*, **84** (2012) 2089.
2. P. Tesavibul, R. Felzmann, S. Gruber, R. Liska, I. Thompson, A. R. Boccaccini, and J. Stampfl, *Mater. Lett.*, **74** (2012) 81.
3. B. C. Gross, J. L. Erkal, S. Y. Lockwood, C. Chen, and D. M. Spence, *Anal. Chem.*, **86** (2014) 3240.
4. A. Bagheri, and J. Jin, *ACS Appl. Polym. Mater.*, **1** (2019) 593
5. X. Wang, M. Jiang, Z. Zhou, J. Gou, and D. Hui, *Composites Part B*, **110** (2017) 442.
6. G. Postiglione, G Natale, G. Griffini, M. Levi, and S. Turri, *Polym. Compos.*, **38** (2017) 1662.
7. M. Ueda, K. Takase, and T. Kurosawa, U.S. Patent 8980971 (2015)
8. A. A. Mousawi, P. Garra, X. Sallenave, F. Dumur, J. Toufaily, T. Hamieh, B. Graff, D. Gigmes, J. P. Fouassier, and J. Lalevée, *Macromolecules*, **51** (2018) 1811.
9. J. Zhang, F. Dumur, P. Xiao, B. Graff, D. Gigmes, J. P. Fouassier, and J. Lalevée, *J. Polym. Sci., Part A: Polym. Chem.*, **54** (2016) 1189.
10. S. C. Ligon, R. Liska, J. Stampfl, M. Gurr, and R. Mülhaupt, *Chem. Rev.*, **117** (2017), 10212.
11. G. Griffini, M. Invernizzi, M. Levi, G. Natale, G. Postiglione, and S. Turri, *Polymer*, **91** (2016) 174.
12. R. Yu, X. Yang, Y. Zhang, X. Zhao, X. Wu, T. Zhao, Y. Zhao, and W. Huang, *ACS Appl. Mater. Interfaces*, **9** (2017) 1820.
13. M. Invernizzi, G. Natale, M. Levi, S. Turri and G. Griffini, *Materials*, **9** (2016) 583.

COPY

14. K. Kobayashi, H. Takamatsu, H. Okamoto, T. Taniguchi, and T. Karatsu, *J. Photopolym. Sci. Technol.*, **34** (2021) 231.
15. M. Ito, H. Takamatsu, T. Taniguchi, H. Okamoto, and T. Karatsu, *J. Photopolym. Sci. Technol.*, **34** (2021) 237.
16. S. Tanaka, Y, Nakashima, and H. Kishi, *Networkpolym.*, **33** (2012) 140.
17. M. A. Paserb and I. N. Bakirova, *Rus. J. Gene. Chem.*, **6** (2014) 84.
18. J. H. Kim, E-S. Park, J. H. Shim, M-N. Kim, W S. Moon, K-H-Chung and J-S. Yoon, *Agric. Food Chem.*, **52** (2004) 7480.
19. J. P. Collin, D. Jouvenot, M. Koizumi, and J. P. Sauvage, *Inorg. Chem*., **44** (2005) 4693.
20. Y. Lu, K. W. Joseph Ng, H. Chen, X. Chen, S. K. Jacob Lim, W. Yan and X. Hu, *Chem. Commun.*, **57** (2021) 3375.
21. Q. Shi, K. Yu, X. Kuang, X. Mu, C. K. Dinn, M. L. Dunn, T. Wang and H. J. Qi, *Mater. Horiz.*, **4** (2017) 598.
22. J. C. Yang, X. Huang, Y. Meng, and M. Anthamatten, *ACS Appl. Polym. Mater.*, **1** (2019) 1829.
23. D. G. Sycks, D. L. Safranski, N. B. Reddy, E. Sun, and K. Gall, *Macromolecules*, **50** (2017) 4281.
24. K. Kawai, K. Kurosaki, and T. Suzuki, *Cryobio. Cryotech.*, **54** (2008) 71.

COPY

Review

Journal of Photopolymer Science and Technology
Volume 36, Number 2 (2023) 111－116 ©2023SPST

Recent Trend of Advanced LSI Packaging: Introduction for application of polymers

Takumi Ueno

Faculty of Textile Science and Technology Fiber Innovation Incubator, Shinshu University, 3-15-1 Tokida, Ueda, Nagano 386-8567, Japan

**ueno-t@shinshu-u.ac.jp*

Recent trends in Advanced LSI Packaging for heterogeneous integration are described. 2D package also called MCM (Multi Chip Module), FOWLP (Fan-Out Wafer Level Packaging) which has been applied to smartphones, 2.5D package using silicon chip as an interposer, chip embedded package which compensates for the shortcomings of the 2D and 2.5D package, and the 3D package which has recently gained great attention, are discussed. While it is becoming more difficult to improve performance by shrinkage of critical feature size and scaling rules, the proposed the concept of chiplets has led package technology to play a role in further improving the performance of LSIs.
Keywords: MCM (Multi Chip Module), FOWLP (Fan-Out Wafer Level Packaging), 2.5D package, Chip embedded package, 3D package, Chiplets, Photosensitive materials

COPY

1. Introduction

The digitization society greatly advanced by the enhancement of LSI (Large Scale Integration) performance. Furthermore, the growth of such as data science, expansion of data communication, AI (Artificial Intelligence), IoT (Internet of Things), a green technology, the automatic driving will demand the higher-performance computer. These demands for higher performance LSIs which support above technologies are continuing.

LSI has a history of improvement in performance by shrinkage of critical feature size in LSI chip and scaling law. At present, the number of transistors per chip exceeds 10 billion and is approaching 100 billion. This has been achieved greatly by pattern size shrinkage lithography technology, and the efforts are continuing. However, it is said that the so-called Moore's Law, which reduces the cost by increasing the components density, has begun to slow down. The continued development of lithography for smaller feature size is becoming more costly and time consuming of research and development by increased cost of state of art equipment such as EUV exposure tool, complicated processes like multi-patterning, and increased complexity of new transistor structures such as FinFET (Fin Field-Effect Transistor) and GAA (Gate-All-Around) transistors [1].

Under such circumstances, heterogeneous integration combined with 2.5D, 3D packages using KGD (Known Good Die) which is selected good dies manufactured by good yield processes, and FOWLP (Fan-Out Wafer Level Packaging), etc. have been intensively developed [2, 3, 4].

Recently, chiplets has gained great attention, and work on standardization "UCIe 1.0" related to design of data transmission on package board has also started [5, 6, 7]. Chiplets integrates multi dies with different functions manufactured by conventional good yield processes into a single package, while achieving both low cost KGDs and high performance.

To classify the application fields of packaging technology are

- PCs (personal computers) and game equipment
- High-performance computers for data centers AI and big data analysis
- Mobile devices such as smartphones smart watches and note PCs
- System of power control with power device implementation in the green energy field

Received March 24, 2023
Accepted May 18, 2023

- Automotive electric and autonomous driving and high-performance processor for image recognition.

As shown in Fig. 1, the roles of the package are to supply power and transform signals by changing the size from the nm-level fine wiring of the LSI chip to the mm-level interface on mother board. Along with the miniaturization of LSI, shrinkage of pattern size is also advancing in the package area.

Other functions of the package include a heat dissipation and a protection against various environmental changes. Various materials such copper as conductor, insulating organic materials, solder for connections between Si die and PCB (Printed Circuit Board), Si for LSI, conductors and insulators fabricated in LSI are used for packaging system. The CTEs (Coefficient of Thermal Expansion) of these materials are different. This requires to ensure reliability that can withstand the thermal history of the package manufacturing processes and to withstand environmental changes. Furthermore, the chiplets proposed recently has come to play an important role in further improving the performance of LSIs.

In this paper, the recent packaging technologies including the past ones for mobile devices and high-performance computers are described.

COPY

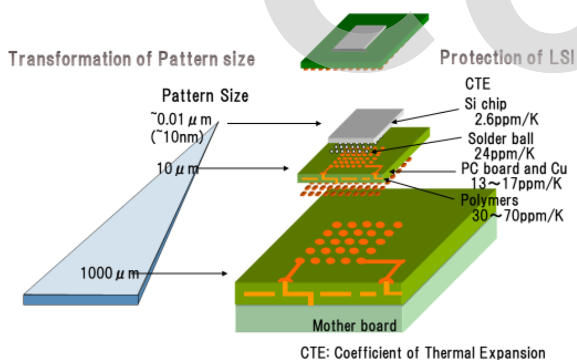

Fig.1 Roles of Package.

2. 2D Packaging

The technology of arranging chips on a PCB and connecting them to each other on the board to improve overall performance is known as MCM (Multi Chip Module) or SiP (System in Package). Various technologies have been developed along with the increase in the number of bumps connected to the substrate associated with the advancement of SoC (System on Chip) which is accelerated by the integration of numbers of transistors on LSI and the shrinkage of minimum feature size by the lithography technology.

The solder connection technology so called C4 (Controlled Collapse Chip Connection) as shown in Fig. 2 that flips the LSI chip with solder balls upside down to connect the solder bumps to the pad on the package board was developed by IBM [8].

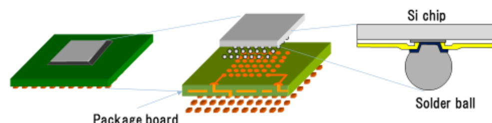

Fig. 2. Solder connection technology so called C4 (Controlled Collapse Chip Connection)

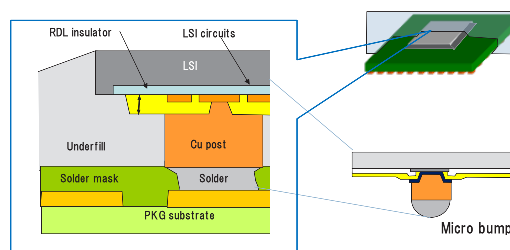

Fig. 3. Micro bump of Cu post used for CPU package.

With the progress of SoC technology, the number of bumps has increased, which led the narrower bump pitch. It has also resulted in the need to keep the bump height uniformity. A micro bump of Cu post formed on LSI side and reduced amount of solder as shown in Fig. 3 has been used [2, 3].

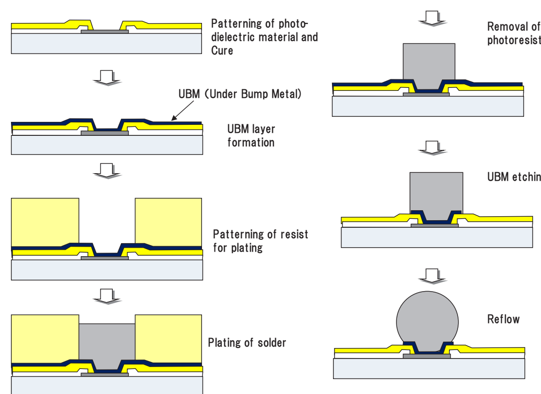

Fig. 4. An example of Solder bump forming processes.

Since it has become difficult to connect a large number of bumps of an LSI chip to a motherboard, organic package substrates with narrower pitch pad and finer wiring and Si interposers manufactured by LSI back-end process technology have come to be used. It is estimated that bumps on LSI chip is ~10,000 bumps/cm^2, while solder ball pitch for a motherboard is around 500~1,000 bumps/cm^2 [1].

Double-sided SiP has also been reported recently for 5G and wearable applications [9].

Photosensitive materials are used for forming the bumps described above. As an example, a solder bump forming process is shown in Fig.4. The IMS (Injection Molded Solder) method, an advanced type of C4, which forms solder by printing requires heat resistance of photosensitive materials [10].

3. FOWLP (Fan-Out Wafer Level Package)

With growing the performance of CPUs (Central Processor units), the increasing number of bumps has made it difficult to mount directly on the motherboard. In order to relax the bump pitch, a fine metal wired package substrate (interposer) is placed between the motherboard and the LSI chip [3]. However, this type of package substrate requires finer wiring, leading to low manufacturing yield, which results in increase in cost. Infineon proposed FOWLP in order to alleviate the cost increase as well as solder bump pitch issues. As shown in Fig. 5, the solder balls can be placed outside the chip. Therefore, even if the number of bumps on the chip side increases, the package can be adjusted to the size (pitch) of the current available solder balls. Fig. 6 shows the chip first FOWLP process. PoP (Package on Package) equipped with DRAM on the top of FOWLP installed with an application processor has become the mainstream package for smartphones as shown in Fig. 7.

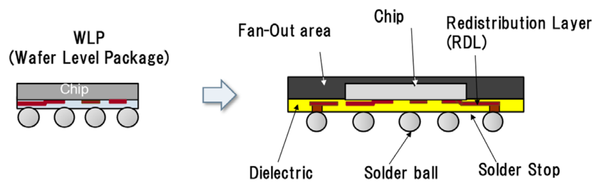

Fig. 5. Wafer level package and FOWLP（Fan-Out Wafer Level Package）.

Fig. 7 also shows applicable photosensitive materials for fabrication in PoP packages. Photosensitive materials include resists used in LSI manufacturing, bump forming resists, insulating materials for RDL (Redistribution Layers), and photosensitive films for Cu plating. Photosensitive insulating materials for RDL have been reported from several companies [11-14]. Polymer-related materials include a film for release layer acting temporary adhesive, encapsulant materials, die bonding film etc. as expected from the processes in Fig.6.

As the pattern size of RDL is reduced, maintaining the reliability of the package becomes more difficult. In particular, the high-temperature processes of soldering cause a stress around the soler ball and interface of the interconnect materials in RDL [15, 16]. The stress of the outer solder balls of the arranged on FOWLP is large, and the stress may induce the damage on the wiring in RDL layer. The effects of the width of the wiring, the thickness of the insulating layer, and the wiring shape on the stress of soldering ball are analyzed [15]. The elastic modulus and CTE of the photo-dielectric materials used in the insulating layer also affect the stress between interface of metal line and insulators. The curing temperature of insulating layer of photo-dielectric materials also influences the stress. Recently the thinnest DRAM FOWLP that has better thermal, mechanical and electrical performance than conventional wire-bonded type memory packages has been reported [17].

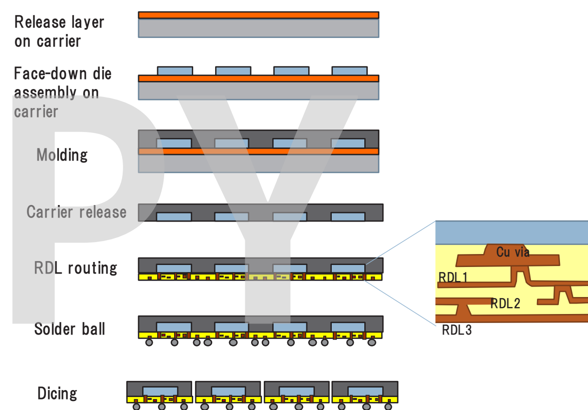

Fig. 6. Chip first FOWLP process.

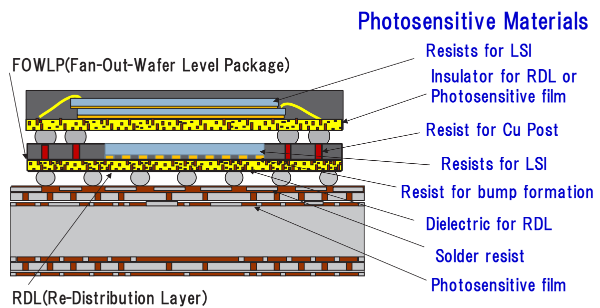

Fig. 7. Photosensitive materials for FOWLP process and related POP (Package on Package) on a mother board.

FOPLP (Fan-Out Panel Level Package) based on use of a large panel such as glass plate has been used in order to reduce the manufacturing costs of FOWLP [18]. The die shift during of mold process is a challenge in yield of the manufacturing. A

COPY

method of controlling the arrangement of dies in consideration of the molding die shift in advance is applied. Furthermore, an improvement method called adaptive patterning technology which detect die shifts by the adaptive alignment of direct laser exposure tool and exposure of the controlled area for redistribution layer has been proposed to increase the yield [19].

4. 2.5D Packaging using Si interposer

A Si chip is used as an interposer instead of an organic substrate called 2.5D packaging as shown in Fig. 8. The Si chip used as the interposer does not have transistors, but instead contains bumps that connect wiring to the logic chip, and TSVs (Through Silicon Via) that connect the top and bottom chips. In this case, the wiring density can be increased because metal layers can be manufactured with LSI back-end-processes. On the other hand, increase in mounting LSI chips makes the area of the Si chip of the interposer larger, leading to an increase in cost. One of the challenges of Si interposer fabrication is the larger exposure area for wiring pattern formation, while the size of the reticle used for existing exposure equipment limits exposure area [20].

COPY

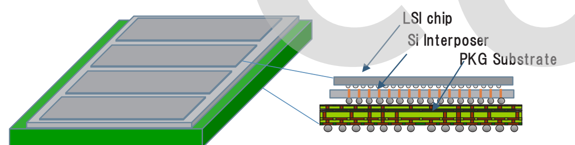

Fig. 8. 2.5 package with Si interposer.

5. Packaging embedded dies interconnect bridge

Chip embedded package was proposed as a technology to compensate for the shortcomings of 2D and 2.5D [21, 22] as shown in Table 1. In a 2D package using an organic PCB as an interposer, the die-package connection density through an organic substrate is limited. The yield to fabricate PCB decreases due to the issues like distortion of the PCB, as the finer wiring patterns on an organic substrate is required.

A 2.5D package that uses a Si interposer enables wiring to be formed in a Si process, which improves connect density and provides narrow bump pitches. As describe above, the area of the Si interposer, however, become large, leading to an increase in cost as well as the size limitation of the Si interposer due to the size of the reticle (mask).

Intel has proposed a package embedded multi-die interconnect bridge (EMIB) that can mitigate the drawbacks of 2D and 2.5D packages by using a structure in which a relatively small Si chip embedded in organic substrate bridges between LSIs [21]. Two different kinds of bumps, C4 and micro bumps, on the chips are used to bridge. IBM has also proposed a similar design of Direct Bonded Heterogeneous (DBHi) Si bridge [22]. Applied Materials, TSMC, Unimicron, ASE, and Amkor have also reported packages similar to AMD's Elevated Fanout bridge [3, 27].

Table 1. Comparison of package structures.

	die-package connection	die-die interconnects	Cost
Multi-chip Package Die-1(LSI) Die-2(LSI) PKG substrate	Poor density	Poor density 500～1000 /cm^2	Low
Silicone Interposer PKG substrate	Good density	Good density ～10,000 /cm^2	Higher cost of larger interposer + TSV
EMIB: Embedded Bridge PKG substrate	Good density	Good density ～10,000 /cm^2	Low cost of smaller silicone bridge

One of the challenges of EMIB is to fabricate a cavity. EMIB has a cavity in the buil-up substrate. A bridge chip is arranged in the cavity and connects chip 1 and chip 2. In DBHi, after connecting the bridge chip with LSI chip 1 and chip 2, those are installed in the cavity. A laser debonding process has been reported by IMEC for a bridge fabrication process [23].

6. 3D Packaging for heterogeneous integration

Intel has announced a three -dimensional package technology that can use TSV to improve performance while the substantial chip area is reduced [24]. TSVs associated with Cu pillars which reduce resistance are used for power supply and high-speed signal transfer. Another key technology of this packaging is a structure of direct Cu pad connection between chips with the aim of increasing the number of connected electrodes and the transmission speed without soldering. As a result, the bump pitch can be improved to less than 10 μm. They reported that chips connected with Foveros (TSV related technology) and EMIB provides 45TFLOPS (10^{12} Floting-point Operations Per Second) of sustained vector FP32 performance and 5TB/s of sustained memory fabric bandwidth [25].

Chiplets architecture is now accepted as a key technology to enable the continued economically viable growth of power efficient computing under the situation of the slowdown in Moore's Law. Agarwal and coworkers of AMD's have reported a notable package with a three-dimensional package of CPU and Cache memory using TSV technology as shown in Fig. 9 [26, 27]. As a result, this chiplets can meet continued demands for increased device density, higher memory bandwidth, reduced global interconnects, increased energy efficiency, and a smaller footprint.

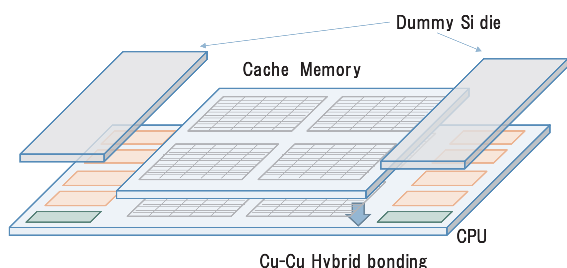

Fig. 9. 3D package of cache memory on CPU chip.

In addition to increasing the number of transistors for the CMOS logic, high performance CPU requires the higher cache memory capacity. However, since the cache memory SRAM forms one memory with six transistors, it causes the issue of increasing the chip area. If the cache memory produced separately can be placed to connect CPU core with short distance, it can be expected to improve performance while maintaining LSI yield. The 3D chiplet was realized by applying the direct Cu-Cu connection between the chips.

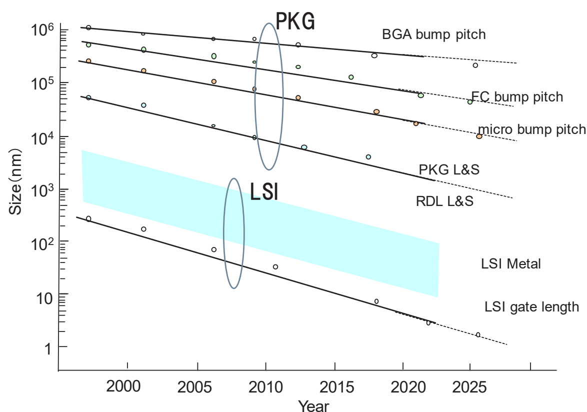

Fig. 10. Technology trends of packaging (PKG) and LSI fabrications.

Swaminathan reported >3x higher interconnect energy efficiency and x15 higher interconnect density (30-50μm pitch to 9μm pitch) compared to micro bump 3D architecture. In desktop gaming system and their technology delivered on average 15% faster gaming performance [27].

7. Trends of Package technology

Fig. 10 shows the trends of pattern size of lithography for LSI and the package [28]. The shrinkage of pattern size of package is also advancing with the trend of miniaturization in LSI. The wiring pattern size of the package substrate is the level of state-of-the-art pattern size of LSI in the late 1970s. However, copper pattern on an organic substrate has a large aspect ratio, which is more difficult than the fabrication of LSI in the 1970s. In addition, it seems that the transition from solder balls to micro-bump (Cu posts with solder), and to direct Cu-Cu connection. The pitch of electric connections between LSI chips and between LSI chip and package board becomes smaller and connection density becomes larger. In these trends, photosensitive materials for smaller size patterns will play an important role.

COPY

8. Conclusion

Different types of package structures have been proposed. The advanced packaging technology plays a role in not only flexible connection from the nm level of LSI to the mm level of the motherboard but also relieving heat and mechanical stress and protecting from the external environment. It should be noted that the chiplets proposed recently has come to play a major role in further improving the performance of the systems composed of LSIs. Considering these roles, the technologies for reliable materials and processes will become more and more important in LSI packages.

Acknowledgement

The author would like to thank for the fruitful discussion with Dr. Sanjay Malik of FujiFilm Electronic Materials U.S.A., Inc. and Dr. Tetsuya Enomoto of Resonac Corp.

References

1. https://eetimes.itmedia.co.jp/ee/articles/2204/25/news056.html.
2. R. Tummala, M. Swaminathan, and P. Nimbalkar, *Chip Scale Review* Mar./Apr. (2022) 6.
3. J. H. Lau, *Chip Scale Review* Jan./ Feb (2022) 21.
4. I. Kojima, *Nikkei Electronics*, Nov. (2022) 79.

5. T. Yunogami, https://eetimes.jp/ee/articles/2102/16/news047.html
6. D. Clark, *Chip Scale Review,* Jan./Feb. (2022) 6.
7. https://eetimes.itmedia.co.jp/ee/articles/2204/25/news056.html. UCIe (Universal Chiplet Interconnect Express) is an open standard that defines the interconnection of chiplets within a package.
8. L. F. Miller, *IBM J. Res. Develop.*, **13** (1969) 239.
9. D. Wang, M. Tsai, J. Y. Chen, and YP Wang, *Chip Scale Review*, Sep./Oct., (2022) 24.
10. J. Mukawa, S. Takahashi, C. Kobata, K. Ohkita, S. Kusumoto, K. Hasegawa, T. Aoki*, E. Nakamura, T. Hisada, H. Mori, and Y. Orii*, *J. Photopolymer Sci. Technol.* **29** (2016) 395.
11. H. Mizuno, T. Sakurai, K. Okamoto, and K. Inomata, *J. Photopolym. Sci. Technol.*, **27** (2014) 199
12. M. Tomikawa, R. Okuda, and H. Ohnishi, *J. Photopolym. Sci. Technol.*, 28 (2015) 73
13. T. Sasaki, *J. Photopolym. Sci. Technol.*, **29** (2016) 379
14. T. Motobe, M. Ohe, N. Yamazaki, and T. nomoto, *J. Photopolym. Sci. Technol.*, **31** (2018) 451.
15. Y. Okada, A. Fujii, K. Ono, and Y. Kariya, *J. Photopolym. Sci. Technol.*, **33** (2020) 171.
16. L. Yip, R. Lin, C. Lai, and C. Peng, *Chip Scale Review* Nov./Dec. (2022) 19.
17. H.-Y. Son, K.-J. Sung, J.-H. Kim, and K. Lee, *Chip Scale Review* Jan./ Feb., (2023) 10.
18. T. Braun, K.-F. Becker, O. Hoelck, R. Kahle, M. Woehrmann, L. Boettcher, M. Toepper, L. Stobbe, H. Zedel, R. Aschenbrentrler, S. Voges, M. Schneider-Ramelow, and K.-D. Lang, , *IEEE Proc. 68th Electronic Comp. and Tech. Conf. (ECTC)* (2018) 70.
19. C. Sandstrom and R. Davis, *Chip Scale Review* Nov./Dec. (2022) 34.
20. R. Mahajan, R. Sankman, N. Patel, D. Kim, K. Aygun, Z. Qian, Y. Mekonnen, I. Salama, S. Sharan, D. Iyengar, and D. Mallik, *IEEE/ECTC Proc.*, May (2016) 557.
21. G. Duan, Y. Knaoka, and R. McRee, *IEEE/ECTC Proc.*, May (2021) 1.
22. K. Sikka, R. Bonam, Y. Liu, P. Andry, D. Parekh, A. Jain, and M. Bergendahl, *IEEE/ECTC Proc.*, June (2021) 136.
23. K. Kennes and A. Guerrero, *Chip Scale Review* Nov./Dec. (2020) 19.
24. https://monoist.itmedia.co.jp/mn/articles/2107/30/news063.html
25. W. Gomes, A. Koker, P. Stover, D. Ingerly1, S. Siers, S. Venkataraman, C. Pelto, T. Shah, A. Rao, F. O'Mahony, E. Karl, L. Cheney, I. Rajwani, H. Jain, R. Cortez, A. Chandrasekhar, B. Kanthi, and R. Koduri, *IEEE International Solid-State Circuits Conf. (ISSC)*, (2022) 42.
26. R. Agarwal, P. Shah, R. Swaminathan, P. Cheng, B. Wilkerson, J. Wuu, and C. Mandalapu, *IEEE Proc. 72nd Electronic Comp. and Tech. Conf. (ECTC),* (2022) 1103.
27. R. Swaminathan, *Chip Scale Review* May/June, (2022) 11.
28. P. Lam, *Chip Scale Review,* Sep./ Oct. (2022) 15.

COPY

Communication

Journal of Photopolymer Science and Technology
Volume 36, Number 2 (2023) 117−122 ©2023SPST

Reliability Study for Photosensitive RDL Material

Ryota Shiraishi*, Yasunori Takahashi, and Ritsuya Kawasaki
Sumitomo Bakelite Co., Ltd. 40-1 Mizumachi, Kamizakai
Nogata, Fukuoka 822-0006 Japan
**shiraishi-ryota@sumibe.co.jp*

In recent years, as electronic devices such as smartphones become more functional, more compact, and lower cost, many semiconductor makers are studying the packages such as WLP (Wafer Level Package) having re-distribution layer (RDL). With the miniaturization and the increase in the number of pins of a semiconductor package, the method of conduction between a semiconductor chip and an external electrode has been changed from wire connection to bump connection and RDL. And the application of a wafer coating material is also required to have higher functions from a buffer coat film to bump protection and an interlayer insulating film for RDL. Further, in recent years, in addition to the purpose of avoiding the performance deterioration of the semiconductor device due to the high-temperature treatment, a packaging material having low heat resistance is sometimes used in the FOWLP, and therefore, the wafer coating material is required to lower temperature curable. We have studied the reliability of the RDL package with various RDL photosensitive materials.
Keywords: RDL, Coating material, Photosensitive resin, High resolution, Low temperature hardening, Reliability of RDL package

COPY

1. Introduction

In recent years, semiconductor packages are used in a wide range of fields, including personal computers, smartphones, and IT equipment related to servers, household appliances, transportation equipment, and industrial equipment. Regarding recent trends in packaging technology, we can see the two directions of technologies from the viewpoint of packaging materials. (Fig.1) The first direction is the downsizing and thinning of semiconductor packages in line with the spread of IT systems such as 5G and so on. To apply such advanced package structures called heterogeneous integration, package materials are required to be low in stress for thinning, and to have fine pattern-ability for narrow pitch and narrow gap. Another direction is high efficiency and withstand voltage of power devices for transportation equipment such as

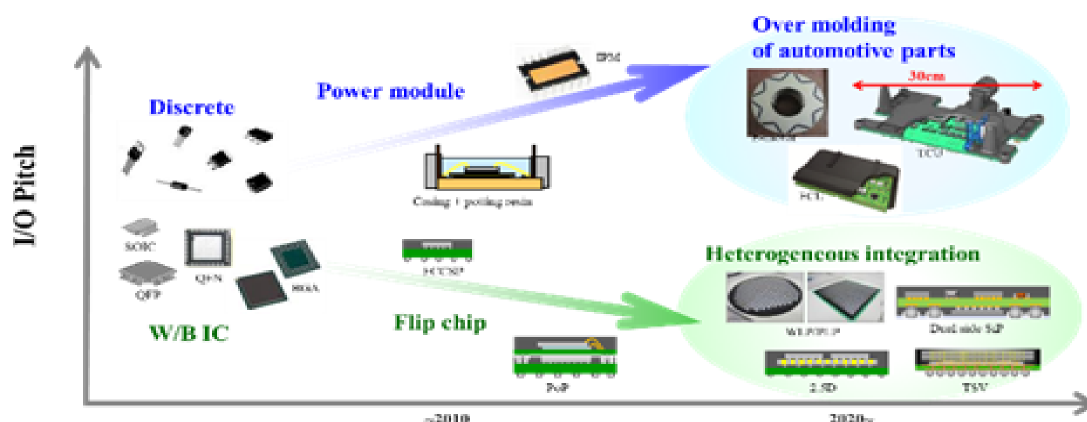

Fig.1 The two directions of technologies for package

Received March 31, 2023
Accepted May 16, 2023

automobiles and railways, and industrial equipment such as robots. Therefore, packaging materials are required to have high heat resistance and insulation properties. Heterogeneous integration has been a shift from Flip Chip CSP (Chip Size Package) to the structure in which multiple different chips are mounted in one package such as InFO PoP (Integreated Fan-Out Package on Package) and SiP (System in Package). As for packaging technology, miniaturization of chips and packages, high density of I/O, and Fan-out PKG process applicability have been increasing. [1-5]

To achieve these requirements, typical properties required for wafer coating materials include a higher resolution for higher electrode density and low temperature curable at the heat temperature of the substrate material of the Fan-out package. And other properties such as high insulation and heat resistance are required to package power semiconductors. [6]

In the case of RDL, as it is necessary for RDL structure formation must pass complex processes, the photosensitive material for RDL needs to have the properties to pass it. For example, high resolution and high chemical resistance are required. In addition, high reliability is required for the RDL photosensitive material. For example, adhesion with copper wiring, adhesion between photosensitive insulating materials, and thermal reliability after u-HAST (un-Biased Highly Accelerated Stress Test), HTS (High Thermal storage), TC (Thermal Cycle), and reflow. In this study, we evaluated the reliability of photosensitive materials for RDL materials (RDL materials) and examined the required characteristics for developing new RDL materials.

2. Experimental

2.1. RDL process

We tried to evaluate RDL two-layer package. The outline of RDL process is showed Fig.2.

All samples were fabricated on 8-inch silicon wafers. Silicon wafers were thermally oxidized to form SiO_2 with 500 nm thickness.

The 1st copper layer was formed by a semi-additive plating process (SAP). To form the seed layer, the reverse argon sputtering process was used as a pretreatment. 25 nm titanium layer and 150 nm copper layer were deposited. Next, positive type resist was coated with 5μm thickness (5μmt) on the wafer by spin coater. Furthermore, the wafer was exposed by an i-line stepper, using a reticle with arrays of daisy-chain patterns. And, the exposed areas were opened by paddle development with 2.38% TMAH aq. developer. Before electrolytic copper plating, oxygen plasma treatment was performed to remove organic residue from the opened area and to improve the wettability of the resist film. Next, copper wiring was formed with approximately 2 μm thickness by electrolytic plating. The wafer set cathode side was immediately immersed in a copper sulfate bath. Then, it was immersed in a resist stripping solution to remove the unnecessary resist. To remove the seed layer except for the wiring pattern area, seed etching was performed in the order of copper seed and titanium seed.

Next, the process was transferred to form 1st resin layer with conduct via. To clean the copper wiring surface, acid treatment was performed. As copper is easily oxidized, it is a risk of the great variability of the surface condition in the plane. So, oxygen plasma was performed after the acid treatment. The RDL material was coated by a spin coater (5μmt on copper wiring after curing). Exposure was performed under the same condition in-plane with appropriate exposure dose and focus. Development was carried out by either the spray method using cyclopentanone or the paddle method using 2.38% TMAH aq. Curing of RDL material was performed under a nitrogen atmosphere at 230°C for 2 hours. After curing, oxygen plasma treatment was performed to remove residues from the bottom of the via.

The 2nd copper layer was formed by SAP also. The process is almost the same as the 1st copper layer formation. After seed etching, oxygen ashing treatment was performed to remove metal residue on the 1st RDL material surface.

Finally, the 2nd resin layer was formed. Acid treatment and oxygen plasma treatment were also performed before the second resin layer formation. The 2nd RDL material was also coated by a spin coater. (5μmt on copper wiring after curing). To open the pattern of the pad portion for the continuity test with Φ1~2mm, exposure was performed by direct-write exposure device. And then development was performed with the developer. After that, curing treatment was performed. To prevent oxidation of copper in the pad area due to reliability treatment, nickel and gold were stacked on the pad area by a non-eletrolytic plating process (3μm Nickel and 50 nm Au). [7]

COPY

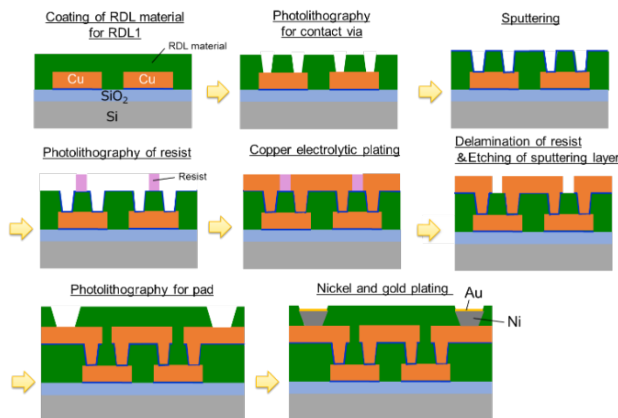

Fig.2 Outline of RDL process

2.2. Evaluation materials

We prepared several materials for the evaluation. The RDL materials used in the evaluation were as follows. Material A is negative type and uses polyimide. Material B is negative type and uses epoxy resin. Material C is positive type and uses polybenzoxazole.

Table.1 Film property of RDL material

	Unit	Material A	Material B	Material C
Main resin	-	Polyimide	Epoxy	Polybenz oxazole
type	-	Nega	Nega	Posi
Curing condition	°C/hrs	230/2	170/2	230/2
Tensile modulus	GPa	3.2	2.3	2.7
Elongation	%	50	30	40
Tg	°C	280	170	283
CTE (50-100°C)	ppm/°C	51	73	39

2.3. Evaluation contents

As a preliminary study, the adhesion b/w the RDL material and the plated copper, b/w the RDL material and the RDL material itself was evaluated. In addition, the lithographic resolution was evaluated to check if the via could be opened or not with the desired shape. Reliability process conditions after assembling the package are shown in Table.2.

Table.2 Reliability test condition

Reliability test	Condition
Un-biased Highly Accelerated Stress Test (u-HAST)	130℃/85%/264hrs
Thermal Cycle Test (TCT)	-65℃⇔150℃ 200 cycle
High-Temperature Storage (HTS)	150℃/500hrs
Nitrogen reflow	260℃(Peak temperature) x 10 times Peak temperature hold time: 30 seconds
Oxygen reflow	260℃(Peak temperature) x 6 times Peak temperature hold time: 180 seconds

Before and after each reliability test, the copper wiring resistance change rate was measured with a four-terminal resistance tester. In addition, cross-sectional observation of RDL structure was conducted after reliability evaluation.

3. Results and discussion

3.1. Adhesion of RDL material

The adhesion of the RDL material contacted with plated copper and cured RDL material film was evaluated. The RDL material was coated and cured on the plated copper or the cured RDL material itself, and grid lines were made on the test pieces by knife. And then scotch tape test was conducted. As a result, peeling of the film was not observed on each substrate, and it was confirmed that each RDL material film has high adhesion to each material.

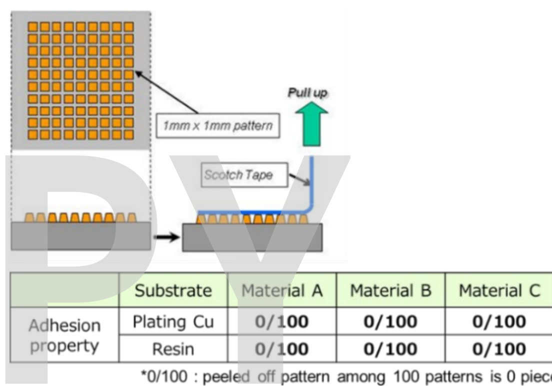

	Substrate	Material A	Material B	Material C
Adhesion property	Plating Cu	0/100	0/100	0/100
	Resin	0/100	0/100	0/100

*0/100 : peeled off pattern among 100 patterns is 0 piece

Fig.3 Adhesion of RDL material

3.2. Lithography resolution of RDL material

The diameters of the via connecting the 1st copper layer and 2nd copper layer are Φ5μm and 8μm. Exposure dose and focus were optimized for the via by i-line stepper,

Cross-sectional photographs of the Φ5μm circular via on the 1st copper layer are shown in Fig.4. Materials A has a tapered via shape where the middle diameter is larger than the bottom diameter. Material B has a vertical via shape with the middle and bottom diameters equal. Material C has tapered via shape, but the taper angle is very low. This low taper angle is caused by the large curing shrinkage rate of material C. If the taper angle is too low, the top diameter of the via exceeds the land diameter of the 2nd copper layer, and the 2nd copper wiring cannot be made with the appropriate shape.

COPY

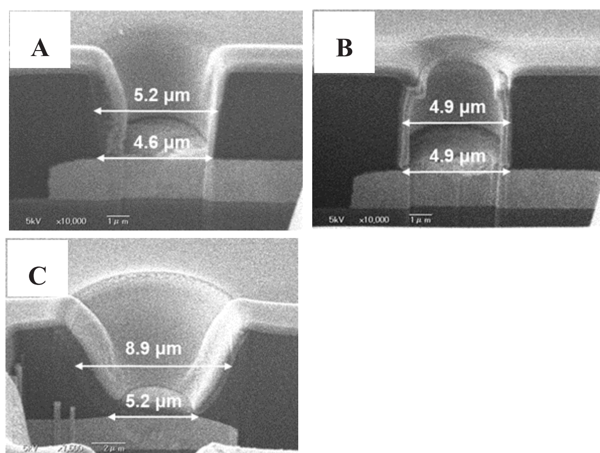

Fig.4 Opened area of circular via

3.3. Wiring shape stability after reflow

The sample was prepared according to the process flow described in 2-1. The appearance after the 2nd copper layer formation is shown in Fig.5. The daisy-chain pattern is aligned horizontally, and the 1st copper layer pattern can be faintly seen between the 2nd copper layer patterns.

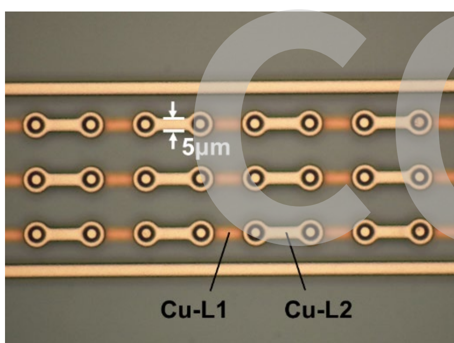

Fig.5 Package appearance after 2nd copper layer formation

Furthermore, the 2nd resin layer was formed and reliability processing was performed. After nitrogen reflow treatment, FIB processing was performed on the test piece, and the cross-section was observed by FE-SEM. For the material with high glass transition temperature (Tg) such as Material A, there was no deformation at the daisy chain (Fig.6). It is estimated that stress on the copper wiring is reduced by the material because Tg of material A is higher than 260℃ (reflow temperature) and the thermal expansion of the resin film is suppressed.

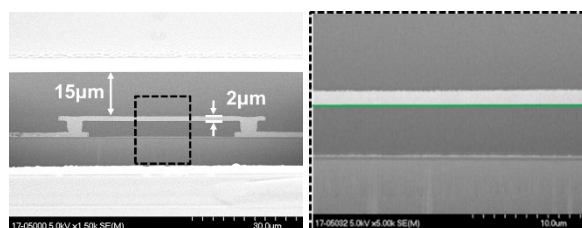

Fig.6 Cross-section view of RDL package after nitrogen reflow (Left: Whole pattern containing via, Right: Daisy chain portion)

3.4. Continuity test after reliability process

After the nickel and gold plating process, copper wiring resistance was measured by a four-terminal tester. Then, each sample was subjected to various reliability processes. After the reliability process, the resistance value was measured again and the resistance change rate was calculated according to the below formula.

$$(b-a)/a\times 100 \quad (1)$$

a: Resistance value before the reliability process
b: Resistance value after the reliability process

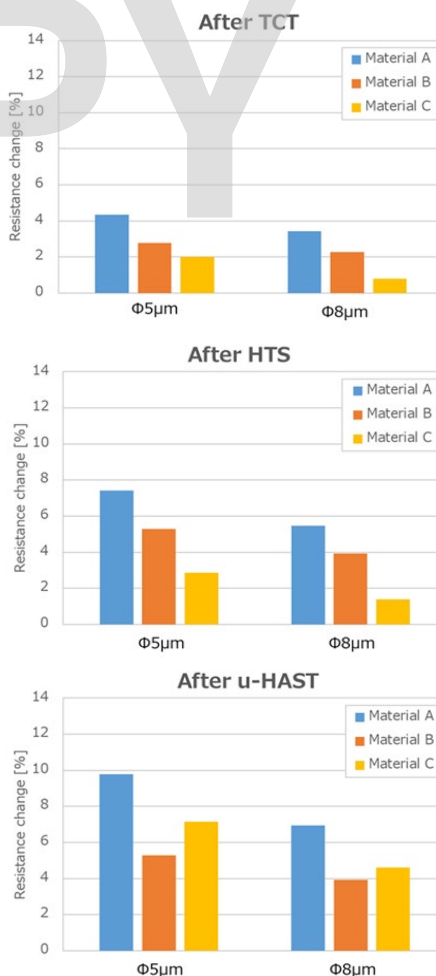

Fig.7 Resistance change rate after the reliability process

COPY

This result is shown in Fig.7. Material A has the highest resistance change rate after u-HAST, HTS, and TCT. On the other hand, material C had the smallest resistance change after HTS and TCT. The reason for the large resistance change is due to the reduction in the effective volume of the copper wiring. Copper wiring has formed copper oxide through reliability testing. It is assumed that the formation of copper oxide is affected by the oxygen permeability of the RDL material.
The resistance change rate is smaller for Φ8μm than that for Φ5μm. In the reliability process, it is assumed that the smaller the wiring diameter is, the lower the ratio of the effective volume of the copper wiring is. [8]

3.5. Formation of copper oxide after HTS

We investigated the cause of the increased resistance change. As it is considered that the sample after HTS is easiest to form copper oxide, we observed the cross-section after HTS. Curing film on the plated copper substrate was fabricated and then HTS was performed. The sample was processed by FIB and the cross-section was observed by FE-SEM. As a result, voids were observed on the plated copper in all material systems, and the formation of copper oxide was confirmed on the voids (Fig.8). In particular, material A had large voids and cracks at the interface between the curing film and the plated copper.

	Material A	Material B	Material C
Cross-section view after HTS			
Thickness of the copper oxide [nm]	260	100	120

Fig.8 Cross-section view of the interface between RDL material film and copper after HTS

The copper oxide diffuses as copper ions from the copper wiring layer to the resin layer, and its diffusion rate is much faster than the diffusion rate of copper atoms. Therefore, it is thought that the supply of copper into the interface can't catch up with the supply of copper ions into the RDL materials, and voids are generated. [9]

3.6. Effect of copper oxide after the oxygen reflow process

Reflow resistance under an oxygen atmosphere is required as a reliability process.

When the same process was performed on the RDL two-layer structure, the degree of copper oxide growth is still significant. (Fig.9) The resistance change rate was measured after reflow in nitrogen and oxygen atmosphere. Although there was almost no resistance change after the nitrogen reflow, the resistance change after the oxygen reflow increased by about 8%. It can be estimated that the effect of oxygen atmosphere is extremely high for the formation of copper oxide.

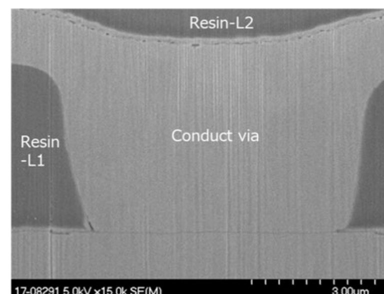

Fig.9 Cross-section view of the RDL package after oxygen reflow.

COPY

To verify the effect of additives on the growth of the copper oxide layer, the same evaluation was conducted by using photosensitive material formulated without additives from Material A. Material A contains an additive that has a carboxylic acid group and an additive that has a tri-azole group. When these additives were removed, the thickness of the copper oxide layer after oxygen reflow became smaller.
The curing film was peeled off from the plated copper, and the interface area was analyzed by X-ray photoelectron spectroscopy (XPS). XPS signal showed that the valence of copper changed from divalent to monovalent or zero-valent during the formation process of the curing film. We estimated that the additives reduced the copper in curing and the copper was more easily oxidized in the oxygen reflow.

4. Conclusion

In developing RDL materials, we evaluated the reliability of various photosensitive materials by assembling RDL two-layer packages and examined the characteristics required for the materials.

We found that the oxidation of copper wiring increases the resistance and reduces conductivity in the reliability process involving an oxygen atmosphere.

To improve this problem, we think that approach from the formulation change is necessary, such as

resin design and optimization of additives. In addition, to prevent wiring deformation during the reliability test process, it is considered that the high glass transition temperature of the resin film has the advantage.

Acknowledgments

This article is based on results obtained from "Research and Development Project of the Enhanced Infrastructures for Post 5G Information and Communication Systems" (JPNP20017), subsidized by the New Energy and Industrial Technology Development Organization (NEDO).

Also, we would like to express our gratitude to the Research Center for 3D Semiconductors for their assistance in this study.

References

1. J. Sabatini, "GE's High-Density Overlay Technology," *Surface-Mount Technology*, **6** (1992) 18.
2. W. Daum, W. Burdick, and R. A. Fillion, "Overlay High-Density Interconnect: A Chips-First Multichip Module Technology", *Computer,* **26** (1993) 23.
3. T. Meyer, "eWLB System in Package-Possbilities and Requirements," *IWLPC Proceedings*, **160** (2010).
4. Kang, I.S, "Wafer Level Embedded System in Package (WL-ESiP) for 3D SiP Solution," *IWLPC Proceedings*, (2010) 153.
5. B. Rogers, C. Scanlan, and T. Olson, "Implementation of a fully molded fan-out packaging technology", *IWLPC* (2013).
6. J. H. Kim, *J. Photopolym Sci. & Technol*, **22** (2009) 403.
7. Emmanuel Chery, Fabrice F. C. Duval, Michele Stucchi, John Stabbekoorn, Kristof Croes, Eric Beyneimecc, "Photosesitive polymer reliability for fine pitch RDL applications'', *ECTC*, (2020) 1234.
8. Stephane Moreau, Nacima Allouti, Celine Ribiere Jean Charbonnier, David Bosuchu, Jean-Philippe Michel, Nicholas Buffet, and Pascel Chausse "Passivation materials for a reliable fine pitch RDL'', *ECTC*, (2018) 1577.
9. Yutaro Koyama, Yu Shoji, Keika Hashimoto, Yuki Masuda, Hitoshi Araki, and Masao Tomikawa, "Development of Novel Low-temperature Curable Positive-Tone Photosensitive Dielectric Materials with High Reliability", *ECTC*, (2019) 639.

COPY

Journal of Photopolymer Science and Technology
Volume 36, Number 2 (2023) 123－126 ©2023SPST

Speculation of Mechanical Properties of Ni-W Micro-gears Fabricated by LIGA Process

Kanta Yamamoto[1]*, Kohzo Tamada[1], Kana Okamoto[2], Sho Amano[1], Akinobu Yamaguchi[1], Yuichi Utsumi[1***], and Tohru Yamasaki[2]**

[1] *Laboratory of Advanced Science and Technology for Industry, University of Hyogo, 3-1-2 Kouto, Kamigori, Ako, Hyogo 678-1205, Japan*
[2] *Research Center for Advanced Metallic Materials, University of Hyogo, 2167 Shosha, Himeji, Hyogo 671-2280, Japan*
kanta97@lasti.u-hyogo.ac.jp, yamaguti@lasti.u-hyogo.ac.jp, utsumi@lasti.u-hyogo.ac.jp,

Microgears made of Ni-W alloy that are expected to have high durability, were successfully fabricated by using the LIGA process with synchrotron radiation. In this study, Ni-W electrodeposited alloy microgears were mechanically evaluated. The LIGA process based on the synchrotron radiation facility, New SUBARU at the University of Hyogo was performed at the Beamline BL11 (electron energy: 1.0 GeV). A dimensional evaluation of the fabricated microgears showed that they could be fabricated with a high accuracy of a few percent from the design value. Tensile tests and Vickers hardness tests presented that the Ni-W electrodeposited alloy has excellent material properties in terms of both strength and ductility. As a result, micro gears with high precision, high strength, and high ductility can be fabricated using this process.
Keywords: Synchrotron Radiation, LIGA process, Ni-W electrodeposited alloys, Microgear

COPY

1. Introduction

Microgears are required to meet the growing demand for ultrasmall motors in various fields, especially in the medical field. Microgears require high dimensional accuracy and durability, but it has been difficult to achieve high dimensional accuracy on the order of microns in metals with conventional machining. For example, the smallest standard diameter of gears in practical use is about 300 μm, and it is difficult to manufacture high-precision gears with a standard diameter of 300 μm or less. [1]

On the other hand, the Lithographie-Galvanoformung-Abformung (LIGA) process using synchrotron radiation can fabricate metal parts with a high aspect ratio and dimensional accuracy in the submicron range. [2] However, because a metal is in general electrodeposited in the gaps of the resist by electroplating after resist processing using photolithography, the metals that can be electrodeposited are limited to relatively soft metallic materials such as Ni and Cu, making it has been impossible to fabricate highly durable metal parts.

Recently, it was founded that the Ni-W electrodeposited alloy developed by Yamazaki *et al.* has a nanocrystalline/amorphous composite structure and exhibits high plastic deformability in spite of its high strength. [3 - 14] The Ni-W electrodeposited alloy could provide a solution to fabricate the microgears adequately satisfied with the criteria that ensures the durability and reliability required for the small actuators used in robotic surgical devices of the medical field.

In this study, Ni-W electrodeposited alloy microgears with excellent durability are fabricated using the LIGA process with synchrotron radiation. The microgears were also evaluated for shape accuracy and mechanical evaluation by tensile and Vickers hardness tests.

2. Method

The LIGA process was performed using the

Received March 31, 2023
Accepted May 17, 2023

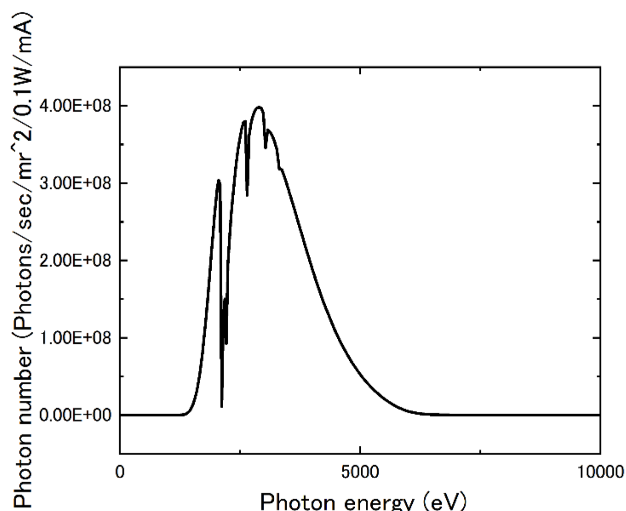

Fig. 1. Photon flux spectrum of BL11 when the NewSUBARU is operated at 1.0 GeV.

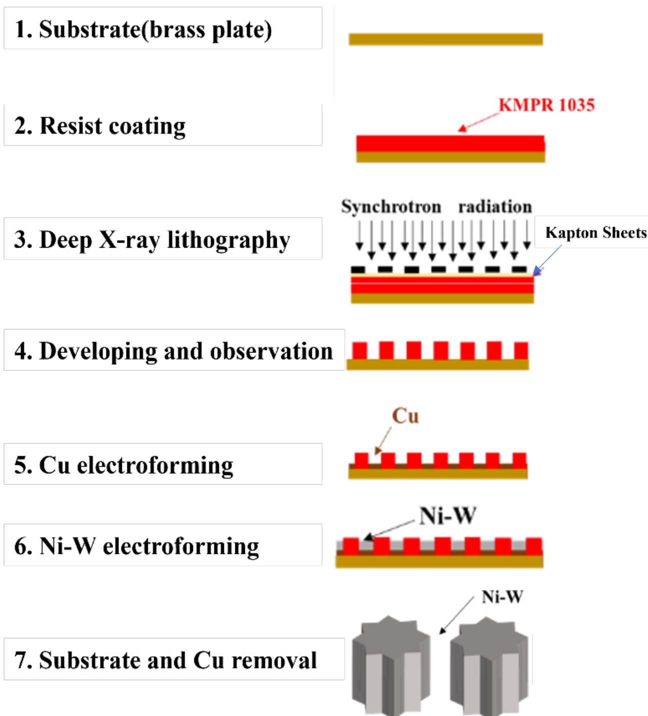

Fig. 2. Fabrication process procedure: (1) Preparation of Substrate, (2) Resist coating, (3) Deep X-ray lithography, (4) Developing and inspection, (5) Cu electrodepostion, (6) Ni-W electroforming, and (7) Removal of substrate and Cu electroplating.

beamline BL11 at the synchrotron radiation facility NewSUBARU in the University of Hyogo. The energy spectrum of BL11 is shown in Fig. 1, where the operating mode of the storage ring is 1 GeV. The fabrication procedure of microgears made of Ni-W alloys is schematically illustrated in Fig. 2.

A 100 mm × 100 mm copper plate with a thickness of 0.3 mm was used as a substrate. Photoresist KMPR 1035 (manufactured by KAYAKU Advanced Materials, Inc.) was used to fabricate the microgears. Before applying the photoresist, Omnicoat (manufactured by KAYAKU Advanced Materials, Inc.) was spin-coated to improve peeling characteristics after resist development and electroforming. Next, exposure was performed using the BL11 operated at 1 GeV. The synchrotron radiation exposure dose was 17 J/cm^2.

After exposure, the substrate was heated at 65°C for 10 minutes and 95 °C for 40 minutes to complete the curing reaction. The substrate was then dipped in SU-8 Developer (manufactured by KAYAKU Advanced Materials, Inc.) and MCC 101 Developer (manufactured by KAYAKU Advanced Materials, Inc.) Photoresist KMPR 1035 is a negative type resist, so the molecular weight increases and the pattern remains after development without dissolving in chemical solvents. Next, a 10 µm copper film was electrodeposited by copper sulfate electroforming to fix the resist and smooth the substrate surface as schematically illustrated in (5) of Fig. 2. Finally, microgears were fabricated by Ni-W electroforming as shown in (6) of Fig. 2. The Ni-W plating solution was a mixture of nickel sulfate and sodium tungstate, with citric acid and ammonium sulfate added as complexing agents. Ir-Ta mesh was used as an anode plate on the substrate. Furthermore, the brushing method proposed by Nakayama *et al.* was applied to suppress the generation of voids and pits due to hydrogen bubbles. Plating time was adjusted so that the film thickness was 80 µm.

COPY

3. Results

3.1 Observation and dimensional evaluation of Ni-W microgear

Figure 3 shows scanning electron microscopy (SEM) images of Ni-W alloy micro gears with diameters of (a) 1000, (b) 500, and (c) 300 µm. Since copper sulfate electroforming was performed before Ni-W electroforming, metallic luster was also observed on the surface of the Ni-W microgears. Dimensional evaluations of microgears by the SEM observation are summarized in Table 1. The shape errors between the design dimensions of the tooth tip diameter, reference circle diameter, and inner circle diameter and the measured values are also summarized. These evaluation results suggest that the microgear can be fabricated with a high accuracy of a few percent from the design value by

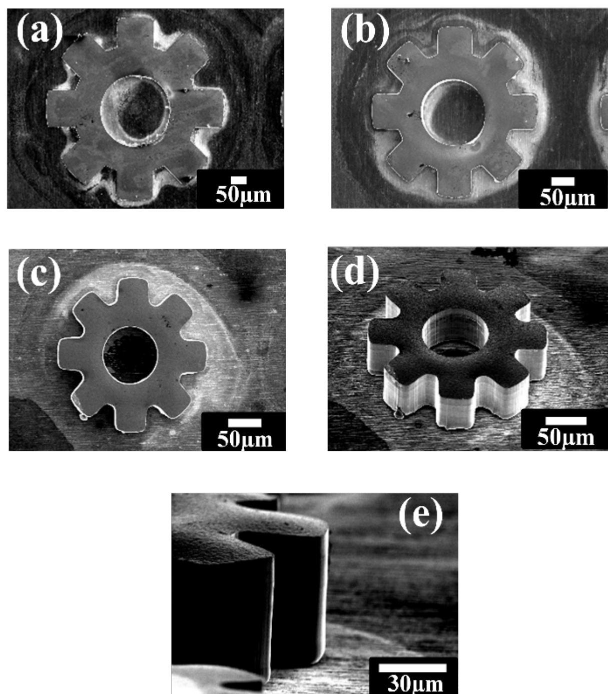

Fig. 3. SEM images of Ni-W microgears with diameter of (a) φ1000 μm, (b) φ500 μm, and (c) φ300 μm. (d) an oblique view of (c). (e) magnified view of the gear portion of the gear.

using this process based on the LIGA process.

3.2. Mechanical Evaluation

As a mechanical evaluation, tensile tests were performed to measure the tensile strength of Ni-W deposit alloys. The tensile specimens were Ni-W electrodeposited alloys with a film thickness of 80 μm produced by this process. The result of the tensile test is shown in Fig. 4. A micro autograph

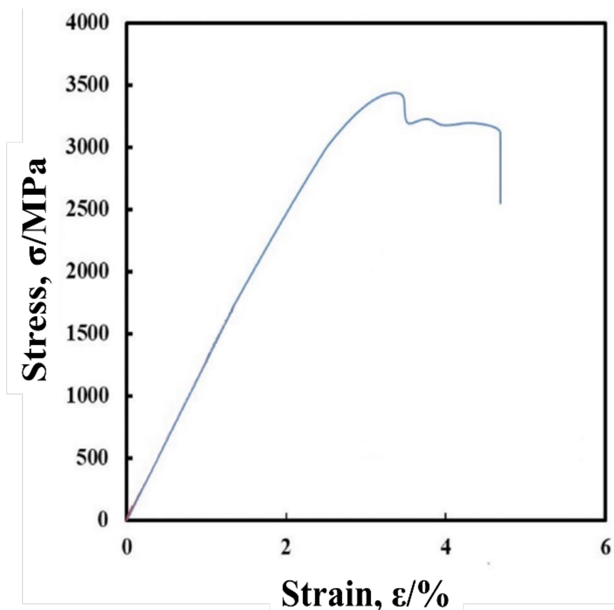

Fig.4. Stress-strain curves obtained by tensile testing of Ni-W electrodeposited film.

(Shimadzu Micro Auto MST-I Type HS/HR) was used for the measurement, and the strain rate was set to 4.2×10^{-4} $s^{-1.}$ The specimen was prepared by electrodeposition of micropatterns with a width of 0.5 mm between the points. We estimated that Young's modulus of this plate was about 1200MPa. We found that the specimens have a high yield strength of about 3500 MPa. It is higher than that of bulk Ni-W (the typical value is about 1600 MPa for an 1-mm-thick Ni-W plate)[15]. It is reported that the yield strength decreases with increasing thickness in Ni-W alloy. [8].

Next, a Vickers hardness test was performed to measure the hardness of the Ni-W electrodeposited alloy. The duration of loading was 15 s. The Vickers hardness of the sample prepared by this process was HV576 (566~599), which is a sufficiently hard material. (Cu: HV40~400, Ni: HV293) [16, 17]. No cracks were observed around the Vickers indentation at the time of measurement, indicating that the material is sufficiently ductile. No difference was observed in the Vickers values when the load was varied.

Table 1.Shape evaluation of Ni-W microgears with diameters of (a) φ1000 μm, (b) φ500 μm, and (c) φ300 μm.

	(a)		(b)		(c)	
	CAD dimensions (μm)	Average value (μm)	CAD dimensions (μm)	Average value (μm)	CAD dimensions (μm)	Average value (μm)
Tip diameter	1000	954	500	497	300	288
Reference diameter	850	829	425	418	255	249
Inside diameter	400	378	200	191	120	110
Shape error	4.2%		2.3%		4.5%	

4. Summary

In this study, Ni-W electrodeposited alloy microgears which were fabricated by using the LIGA process were mechanically evaluated. The dimensional evaluation of the fabricated microgears showed that microgears could be fabricated with a high accuracy of a few percent from the design value. Tensile tests and Vickers hardness tests

COPY

showed that the Ni-W electrodeposited alloy has excellent material properties in terms of both strength and ductility. As a result, microgears with high precision, high strength, and high ductility can be fabricated using this process.

In the near future, conducting dynamic property tests (wear tests and endurance tests) on the interlocking gears is expected to demonstrate their use as highly durable microgears. Besides, this process can provide a clue to realize a highly durable microturbine and contribute to the further development of microfluidics research.

References

1. Y. Kitakoga: Int. J. Jpn. Soc. Precis. Eng. **58** (1992) 1284. (in Japanese). https://doi.org/10.2493/jjspe.58.1284.
2. N. Nakajima and A. Umeda: Advanced Machining Technology & Development Association: LIGA Process – Advancing Three-Dimensional Ultrafine Machining Technology (Nikkan Kogyo Shinbun, 1998) 89 (in Japanese).
3. T. Yamasaki, M. Yamada, H. Adachi, T. Nabeshima, and Y. Yokoyama: Microsyst. Technol. 20 (2014) 1941. https://doi.org/10.1007/s00542-013-2005-7
4. S. Nakayama, H. Adachi, T. Nabeshima, T. Miyazawa, and T. Yamasaki :Sci. Adv. Mater. 8 (2016) 2082. https://doi.org/10.1166/sam.2016.2825
5. T. Yamasaki, M. Sonobe, and H. Yokoyama: Mater. Sci. Forum 561 – 565 (2008) 1295. https://doi.org/10.4028/www.scientific.net/MSF.561-565.1295
6. H. Hosokawa, T. Yamasaki, N. Sugamoto, M. Tomizawa, K. Shimojima, and M. Mabuchi: Mater. Trans. 48 (2004) 1807. https://doi.org/10.2320/matertrans.45.1807
7. T. Yamasaki: Scr. Mater. 44 (2001) 1497. https://doi.org/10.1016/S1359-6462(01)00720-5
8. S. Nakayama, H. Adachi, and T. Yamasak:; J. Alloys. Compd. 643 (2015) S22. https://doi.org/10.1016/j.jallcom.2014.12.209
9. K. Fujita, K. Nagaoka, T. Suidu, T. Nabeshima, and T. Yamasaki: J. Jpn. Inst. Met. Mater. 77 (2013) 192. (in Japanese). https ://doi.org/10.2320/jinstmet.J2012067
10. K. Fujita, T. Suidu, and T. Yamasaki: J. Jpn. Inst. Metals 75 - 76 (2011) 348. (in Japanese). https://doi.org/10.2320/jinstmet.75.348
11. H. Yokoyama, T. Yamasaki, T. Kikuchi, and T. Fukami: Mater. Sci. Forum 561 - 565 (2007) 1295. https://doi.org/10.4028/www.scientific.net/MSF.561-565.1295
12. N. Oda, H. Matsuoka, T. Yamasaki, and T. Fukami: J. Metastable Nanocryst. Mater. 24 - 25 (2005) 411. https://doi.org/10.4028/www.scientific.net/JMNM.24-25.411
13. T. Nasu, M. Sakurai, T. Kamiyama, T. Usuki, O. Uemura, K. Tokumitsu, and T. Yamasaki: Mater. Sci. Eng, A 375-377 (2004) 163. https://doi.org/10.1016/j.msea.2003.10.144
14. Hasseb,A.S.M.A. and Bade,K: Microsyst Technol. 14 (2008) 379. https://doi.org/10.1007/s00542-007-0447-5
15. I.Matsui and N.Omura:Mater.Trans, 59 (2018) 123 https://doi.org/10.2320/matertrans.M2017256
16. N. A. Badarulzaman, A. A. Mohamad, S. Puwadaria *et al.*: J Coat Technol Res. 7 (2010) 815. https://doi.org/10.1007/s11998-010-9271-4
17. S. Chenna Krishna, Narendra Kumar Gangwar, Abhay K. Jha, Bhanu Pant.: *J. Materials.*2013 (2013) 1. https://doi.org/10.1155/2013/352578

Corresponding authors:
*K. Y. (kanta97@lasti.u-hyogo.ac.jp)
**A. Y. (yamaguti@lasti.u-hyogo.ac.jp)
***Y. U. (utsumi@lasti.u-hyogo.ac.jp)

COPY

COPY

JOURNAL OF PHOTOPOLYMER SCIENCE AND TECHNOLOGY

Volume 36, Number 2, 2023

Fabrication of Moth-eye-structured Films with Two Types of Resin Separated by Micro-order Regions 67
Kazuki Fujiwara, Hiroyuki Sugawara, and Jun Taniguchi

Filling Behavior Observation of UV-curable Resin Using Bridge-Structure Mold 73
Yusuke Murakami, Yusuke Nagai, and Jun Taniguchi

Transfer Durability of Re-release Coated Replica Mold on Ultraviolet Nanoimprint Lithography 77
Tomohito Wakasa and Jun Taniguchi

Ultraviolet-curable Material with High Fluorine Content for Biomimetic Functional Structures Achieved by Nanoimprint Lithography with Gas-permeable Template for Life Science and Electronic Applications 83
Rio Yamagishi, Sayaka Miura, Mano Ando, Yuna Hachikubo, Tsugumi Murashita, Naoto Sugino, Takao Kameda, Yoshiyuki Yokoyama, Yuki Kawano, Kaori Yasuda, and Satoshi Takei

Development of High Accurate Multi-Step Deep X-ray Exposure System Using Two-axial PZT Actuators 91
Taki Watanabe, Sho Amano, Kaito Fujitani, Akinobu Yamaguchi, and Yuichi Utsumi

Study of Dihedral-Corner-Reflector-Array Fabrication Process Using Soft X-ray Deep X-ray Lithography 97
Taki Watanabe, Sho Amano, Shinya Izawa, Satoshi Maekawa, Keisuke Yoshiki, Akinobu Yamaguchi, and Yuichi Utsumi

Development of Photo-curable Resin for 3D Printing Using Acrylic Monomers with Bisphenol Skeleton 101
Kotaro Kobayashi, Daisuke Aoki, Tatsuo Taniguchi, Takashi Karatsu, Nobuaki Takane, Hiroaki Okamoto, Koichi Fujii, and Yuki Yamauchi

Recent Trend of Advanced LSI Packaging: Introduction for application of polymers 111
Takumi Ueno

Reliability Study for Photosensitive RDL Material 117
Ryota Shiraishi, Yasunori Takahashi, and Ritsuya Kawasaki

Speculation of Mechanical Properties of Ni-W Micro-gears Fabricated by LIGA Process . . . 123
Kanta Yamamoto, Kohzo Tamada, Kana Okamoto, Sho Amano, Akinobu Yamaguchi, Yuichi Utsumi, and Tohru Yamasaki

COPY